STRESS TRIGGERING OF EARTHQUAKES AND SUBSIDENCE IN THE LOUISIANA COASTAL ZONE DUE TO HYDROCARBON PRODUCTION

A DISSERTATION

SUBMITTED TO THE DEPARTMENT OF GEOPHYSICS

AND THE COMMITTEE ON GRADUATE STUDIES

OF STANFORD UNIVERSITY

IN PARTIAL FULFILLMENT OF THE REQUIREMENTS

FOR THE DEGREE OF

DOCTOR OF PHILOSOPHY

Ellen P. Mallman

September 2007

I certify that I have read this dissertation and that in my opinion it is fully adequate, in scope and quality, as a dissertation for the degree of Doctor of Philosophy.

_____

Mark D. Zoback (Principal Adviser)

I certify that I have read this dissertation and that in my opinion it is fully adequate, in scope and quality, as a dissertation for the degree of Doctor of Philosophy.

_____

Gary Mavko

I certify that I have read this dissertation and that in my opinion it is fully adequate, in scope and quality, as a dissertation for the degree of Doctor of Philosophy.

_____

Gregory C. Beroza

I certify that I have read this dissertation and that in my opinion it is fully adequate, in scope and quality, as a dissertation for the degree of Doctor of Philosophy.

_____

Tom Parsons

Approved for the University Committee on Graduate Studies.

Abstract

This thesis presents contributions towards better understanding of the interaction between earthquakes through elastic stress triggering and the role of hydrocarbon production on subsidence and land loss in southern Louisiana.

The first issue addressed in this thesis is that of the role of static stress changes on earthquake triggering. It has been reported that changes in the Coulomb stress following moderate earthquakes can provide a predictive method for determining regions that are more likely to experience future earthquakes and regions that are less likely to experience future earthquakes. However, in order to test whether increases in seismicity are caused by static stress triggering, stress shadows need to be identified. The first study investigated whether observed changes in seismicity rate following the 1992 Landers, California and 1995 Kobe, Japan earthquakes are accurately predicted by elastic Coulomb stress transfer models. To quantify the relationship between Coulomb stress changes and the seismicity rate change, spatial changes in the seismicity rate were compared to the modeled changes in Coulomb failure stress (ΔCFS) for the two subject earthquakes beginning with the simplest and most common ΔCFS model and then increasing to more complex and geophysically realistic ΔCFS models. The analyses found that for all the tested ΔCFS models wherever seismicity rate changes could be resolved the rate increased regardless of whether the ΔCFS theoretically promoted or inhibited failure. In addition, the areas of highest seismicity rate following the main shock did not correlate with the sign or the magnitude of ΔCFS. Rather, the areas most active after the main shock were also the most active before the main shock.

The second study is motivated by the observation that stress shadows are inherently difficult to resolve, and that identifying stress shadows remains the one way to definitively test static stress transfer models. In this work the common definition of a stress shadow was extended to independently test the stress shadow hypothesis using a global catalog of seismicity. The traditional definition of a stress shadow is associated with a decrease in the overall seismicity following a main shock, similar to what was observed following the 1906 San Francisco earthquake. Instead, it is asserted that a stress shadow may be present if there is either: 1) a change in the average focal mechanism of the seismicity before and after the main shock, or 2) a decrease in the seismicity rate for a given mechanism type. Using these new definitions of a stress shadow, a global catalog of 119 $M_s \geq 7$ earthquakes and associated events within a 2-degree region of each main shock in the Harvard CMT catalog were examined. The analyses indicated that while stress shadows are subtle, they are present in the global catalog. It also explains why "classical" stress shadows, similar to what was observed following the 1906 San Francisco earthquake are rarely observed for individual main shocks.

The second issue addressed in this thesis is the role of hydrocarbon production on subsidence and land loss in the Louisiana Coastal Zone. Land loss in the Louisiana Coastal Zone is a wide spread problem that poses a great threat to the regions ecologic and economic stability. While land loss in the Louisiana Coastal Zone is the combination of many processes, both natural and anthropogenic, it has been suggested that oil and gas production may be a large contributing factor to observed regional subsidence and land loss. The two studies in this thesis extend previous work by modeling the effect of oil and gas production in the region in two ways. First, multiple producing oil and gas fields and multiple epochs of leveling data are considered to provide constraints on predicted subsidence. Second, the role of compaction of the reservoir bounding shales on the regional subsidence signal is included. The first study used an analytic model and a first-order leveling line as a constraint to model the effect of oil and gas production on subsidence in Lafourche Parish, Louisiana. The modeled subsidence due to production-induced compaction of the reservoir sands is consistent with observations of several centimeters of localized subsidence over the producing oil and gas fields. Both the modeling and observations of subsidence indicate that subsidence due to reservoir

compaction is highly localized and can not be related to observations of more extensive regional subsidence. Examination of the production and subsidence rates during the two leveling epochs (1965-1982 and 1982-1993) shows that the subsidence rate increased during the 1982-1993 leveling epoch while the production rates decreased. This suggests that a time-dependent mechanism may be an important component of production-induced subsidence.

Given the results of the previous study, the second study related to subsidence in the Louisiana Coastal Zone looks at the role of time-dependent compaction of the shales as a possible mechanism to explain an increased subsidence rate at a time of decreased production. Time-dependent production-induced compaction of shales can then be used as a predictive tool for estimating future subsidence in the region after production has ended. Subsidence due to production-induced compaction of the reservoir sands and reservoir bounding shales was modeled using the ground water flow package MODFLOW. The modeling results indicate that production-induced subsidence will continue to be important over the oil and gas fields due to compaction of the reservoir bounding shales until at least 2050, but the subsidence signal will remain localized over the producing fields. The results of the two studies on the role of hydrocarbon production on subsidence in the Louisiana Coastal Zone indicate that regional models of subsidence must include the effects of production-induced subsidence due to both sands and shales, but that this can not account for the entire observed subsidence signal in the Louisiana Coastal Zone. This work is an integral component in the development of an integrated model of subsidence and wetland loss in southern Louisiana and should be considered during any restoration plans.

Acknowledgements

This dissertation would not have been possible without the help and support of many people.

One of the most important pieces of a PhD dissertation is a great advisor. I have been most fortunate to have Mark Zoback as my advisor for the past six years. His support, encouragement and guidance during this time has been invaluable. He recognized early on topics that would pique my interest and keep me motivated. Mark was incredibly supportive during the frustrating times and shared in my excitement with each breakthrough. Despite a very busy schedule Mark always made time to be available for questions, discussions, and reviewing manuscripts. In addition to providing a great environment for intellectual growth Mark also recognizes the need for balance in both his and his student's lives. His encouragement of our pursuits outside of research, such as traveling, enjoying everything the Bay Area has to offer, and family has made my time in graduate school that much more fulfilling.

I also want to thank Tom Parsons at the USGS in Menlo Park for his support and guidance, especially while working on the stress triggering portions of this dissertation. He provided the initial idea and funding in the form of a summer internship that resulted in the work presented in Chapter 3. He has always been available for discussion and has encouraged my ideas. I would like to thank Tom for serving on my committee since my qualifying exam and taking the time to come over to Stanford for various meetings and annual reviews.

Many thanks for the remainder of my committee over the years: Norm Sleep, Greg Beroza, and Gary Mavko. Your insights and discussions have improved this dissertation in many ways. In addition, I would like to thank George Thompson who always asked insightful questions during group seminars and always made sure that I had seen various articles published regarding my research. His care and involvement in our research group and my research will be one of my fondest memories of graduate school.

Thank you to George Hilley for agreeing to chair my defense even though it was a day after he got back from Tibet! He provided some great insight during the discussions that took place in my defense and the input was appreciated.

The work in Southern Louisiana built on research carried out by Alvin Chan during his PhD, and provided me with a great starting point for my work. Alvin took the time to make sure that I understood what he had done while he was in the process of finishing his dissertation and moving. Even after leaving Stanford, he has always been available to answer my questions and has taken time on every one of his visits to California to discuss my work.

Paul Hagin has been an invaluable resource the past two years of my dissertation. His help with building the MODFLOW model and understanding of the details of the sand and shale compaction modeling have been greatly appreciated. I know that I am not the only person who is very glad that he returned to Stanford!

I would like to thank all the administrators in the Department of Geophysics who makes sure we graduate, get paid, and just make our lives a bit easier. Thank you Jeannette, Lauren, and Tara for all you do. A special thanks to Susan Phillips-Moskowitz for making sure we have everything we need down in the lab, taking care of anything we need, and just watching over us in general.

One of the best things about my time at Stanford is being part of a great research group. Alvin, Amie, Amy, Baltz, Bjorn, Hannah, Hiroke, John T., John V., Laura, Lourdes, Naomi, Pijush, Paul, Stephanie, we have been more than simply colleagues, we have become great friends. Thank you for all the great research related and not research related discussions, coffee breaks, ski trips.

I would like to thank all of my friends here in California who have provided support throughout the years and have done a great job of getting me away from my desk! Thank you Amie, Sara, Kristina, Michelle, Jess, Emily, Laura, Katie, Naomi, Hannah, Kevin, James, Dave, Dave, John, Lourdes, Marissa, Heidi, and Kahla for making my time here so enjoyable! I will miss our runs, bike rides, hikes, and travels. But, look forward to visiting and doing all these things in new locations!

Finally, I have to give my greatest thanks to my entire family for their support over all these years. I especially have to thank my parents, Jim and Sharon, and my brother David for their incredible support of my education. I wouldn't have accomplished all of this with out you.

Contents

List of Figures

List of Tables

Chapter 1

Introduction

1.1   Overview and motivation

This thesis is composed of four specific studies covering two broad topics. The first two studies examine the role of static stress changes on earthquake triggering; the second two examine the role of hydrocarbon production on subsidence in the Louisiana Coastal Zone. While the two topics are different in detail, they demonstrate the effect of crustal stress changes and the potential resulting hazards, either from increased seismicity or greater hurricane and flood risk. Both of these topics have direct impacts on economic and human health along with implications for assessment of programs dealing with hazards and restoration.

In the first study I assessed the validity of elastic Coulomb stress models in predicting observed changes in seismicity rates following the 1992 Landers, California and 1995 Kobe, Japan earthquakes. Shortly after the Joshua Tree – Landers – Big Bear earthquake sequence of 1992, researchers began studying the changes in elastic Coulomb failure stress as a way to explain the locations of aftershocks [*King, et al.*, 1994; *Stein*, 1999; *Parsons, et al.*, 2000]. These studies argued that aftershocks are concentrated in zones with a positive change in the Coulomb failure stress and are rare in zones of negative Coulomb failure stress. In this work I investigated whether the observed changes in seismicity following the Landers and Kobe earthquakes corresponded with the predictions from elastic Coulomb stress transfer models. In addition I extended previous studies by adding two more physically realistic conditions into the Coulomb stress

modeling: 1) the change in Coulomb stress is calculated on optimally oriented planes in three dimensions and 2) the regional stress orientations are heterogeneous. I tested to see if these two additional models more accurately predict the observed changes in seismicity than the common assumptions of optimally oriented strike-slip two-dimensional planes and a regionally uniform stress field. This will help in determining if more realistic and complicated models of elastic Coulomb stress will more accurately predict changes in earthquakes probabilities.

In the second study I carried out a global search for stress shadows following M≥7 earthquakes using a new definition for stress shadows. Earthquakes with M≥7 are expected to reduce the stress in large portions of the surrounding crust, and thus it would seem logical that there should be a decrease in seismicity following these events due to the static stress change. This decrease in seismicity is called a stress shadow and has been observed following the 1857 Fort Tejon and 1906 San Francisco earthquakes in California [*Harris and Simpson*, 1996; *Stein*, 1999]. However, many researchers have had a hard time identifying stress shadows following other M≥7 earthquakes. I propose that stress shadows due to the change in static stress following a main shock may still be present despite the lack of observed seismicity rate decreases if there is a change in the average focal mechanism before and after the main shock. This change in average focal mechanism is the result of suppressing earthquakes of a particular mechanism while encouraging earthquakes of another mechanism resulting in no change (or an increase) in the overall seismicity rate such that a traditionally defined stress shadow would not be identified. Using this new definition, I evaluated 119 events in the Harvard CMT focal mechanism catalog in an attempt to identify stress shadows. In addition to evaluating each of the main shocks and its associated earthquakes individually, another advantage to using a global catalog is the ability to stack the data in order to enhance small signals that would not be significant for an individual event.

The third study examined the role of production-induced reservoir compaction on observed subsidence in the Louisiana Coastal Zone. Subsidence and land loss is a growing problem in southern Louisiana with many implications for both regional and national ecologic and economic stability. While there are many mechanisms driving

lands loss in Louisiana, it has been suggested that subsurface oil and gas production may be a large contributing factor. I extend the work done previously by *Chan and Zoback* [2007] which looked at production-induced subsidence and fault slip over the Lapeyrouse field by building a more regional model to include production from multiple oil and gas fields along with multiple leveling epochs to constrain my model. I use geologic and pressure data to estimate the amount of compaction due to production in the four modeled fields as input into the analytic *Geertsma* [1973] model to estimate the amount of production-induced subsidence. This allowed me to address the following questions: 1) is the subsidence signal higher over the oil and gas fields?, 2) does the rate of subsidence correlate with the rate of oil and gas produced?, and 3) can production induced subsidence explain the observed regional subsidence?

The final study builds on the previous work in Louisiana to look at time-dependent production-induced compaction of not only the reservoir sands but also the reservoir bounding shales. I used MODFLOW-2000, a finite difference groundwater flow program developed by the US Geological Survey to model the subsidence related to compaction of both the sands and shales. I first carried out numerous sensitivity analyses to constrain the constitutive parameters of the sediments, and then used these to model the predicted subsidence over the same time period as the modeled production and leveling data. Using the production and leveling data to calibrate my subsidence model I then extended the model for two additional time epochs when there is no production or leveling data to provide insight into the potential for additional local and regional subsidence after production has ended.

1.2 Thesis Outline

In addition to this introduction, this thesis contains four chapters. Chapters 2 and 3 cover the two stress triggering studies while chapters 4 and 5 cover the work done on production induced subsidence in Louisiana. Chapter 2 has been published in its entirety in the Journal of Geophysical Research, portions of Chapter 4 has been published in the Journal of Coastal Research, and Chapter 3 is has been submitted to the Journal of Geophysical Research. Chapter 5 is in preparation for publication.

1.2.1 Chapter 2 – Assessing elastic Coulomb stress transfer models using seismicity rates in southern California and southwestern Japan

Chapter 2 details the quantitative comparison of seismicity rate changes following the 1992 Landers, California and 1995 Kobe, Japan earthquakes to the modeled changes in elastic Coulomb failure stress. I was interested in how well the stress change models predicted the observed changes in seismicity rates in order to test the validity of Coulomb stress transfer models as a predictive tool for future earthquake hazards following moderate to large earthquakes. I detail the gridding technique and methods used for calculating seismicity rate changes and a method for quantitatively comparing these observed rate changes to the modeled changes in Coulomb failure stress. I then describe the motivation and method for extending the previous Coulomb stress models to include optimally oriented planes in three dimensions and heterogeneous regional stress orientations. The results of this work indicate that every where seismicity rate changes can be resolved, the rate increased regardless of whether the change in Coulomb failure stress would theoretically promote or inhibit failure. Finally, I found that the regions of highest seismicity rate following the main shock did not correlate with the sign or magnitude of the change in Coulomb failure stress.

1.2.2 Chapter 3 – A global search for stress shadows

Chapter 3 builds on observations made in Chapter 2 and by *Felzer and Brodsky* [2005] that that decreases in seismicity predicted by static stress models are rarely observed for individual main shocks. In this chapter I use a global catalog of seismicity and a new definition of a stress shadow to see if this allows stress shadows to be identified for individual main shocks, or by stacking the global data allows me to enhance small signals present, but not significant for individual events. I assert that a stress shadow may be present in a catalog not only if the over all seismicity decreases following a main shock but if there is either 1) a change in the average focal mechanism of the seismicity before and after the main shock, or 2) a decrease in the seismicity rate for a

given mechanism type. These changes in average focal mechanism are due to the change in static stress suppressing earthquakes of a given mechanism while simultaneously promoting earthquakes of a differing mechanism. I then present a graphical method for identifying and quantifying changes in average focal mechanisms before and after the main shock. I use this method to examine both the individual main shocks and their associated events and the stacked data sets. I find that when looking at events associated with individual main shocks stress shadows remain very rare, but that stacking the global data I am able to begin to resolve stress shadows using the new definition developed in this work.

1.2.3 Chapter 4 – Subsidence in the Louisiana Coastal Zone due to hydrocarbon production

Land loss and subsidence in southern Louisiana has come to the forefront of the news over the past couple of years highlighting the long term problem and the implications of the previous and continued loss of this valuable land. In Chapter 4 I examine the role that hydrocarbon production has on subsidence due to compaction of reservoir sands in Lafourche Parish. I first detail the method developed by *Chan and Zoback* [2007] for using bottom hole pressure, a constitutive law for Gulf of Mexico sands, and a generalized Gulf of Mexico stress path to estimate production induced reservoir compaction and an analytic model to estimate the resulting surface subsidence. I apply this method for a region with multiple producing oil and gas fields with a leveling line to constrain the model. I find that the results of the analytic model are constant with what the observed subsidence along the leveling line. However, one of the other reasons I choose Lafourche Parish for the model is that the leveling line has multiple epochs of leveling data which provides insight into time-dependent subsidence mechanisms. I find that while the analytic model for production-induced sand compaction does a good job modeling the subsidence observed in one time epoch it is unable to explain the accelerating subsidence rate observed while production rates decreased. This indicates that there is likely a time-dependent subsidence mechanism for production-induced subsidence that is not being modeled.

1.2.4 Chapter 5 – The role of shale compaction due to hydrocarbon production on subsidence in the Louisiana Coastal Zone

Chapter 5 builds directly on the final observation of Chapter 4 that there is likely a time-dependent subsidence mechanism operating that could explain the increase in subsidence rate observed along the leveling line in Lafourche Parish during a time when fluid production decreased. This has important implications for predicting future subsidence within the Louisiana Coastal Zone and for restoration and protection plans. In this chapter I model the effect of production-induced compaction of both the reservoir sands and reservoir bounding shales using MODFLOW-2000, a finite difference groundwater flow modeling package developed by the US Geological Survey [*Winston*, 2000; *Höffmann, et al.*, 2003]. I first present the background for time dependent shale compaction and the role it plays on delayed and continued surface subsidence following fluid production and the way that MODFLOW models shale compaction and subsidence. I then discuss in detail the parameters used by MODFLOW and the sensitivity of the model to these various parameters. Using the leveling observations I constrain the MODFLOW parameters needed to fit the first two time epochs. Once these two epochs are adequately modeled by MODFLOW I then extend the model into two time epochs after modeled production has ended. This allows me to predict how much additional subsidence can be expected due to production-induced compaction after production has ended and also determine the aerial extent of the effect of the production-induced subsidence. I find that subsidence due to production-induced shale compaction will continue until at least 2050, but that it continues to be primarily localized over the oil and gas fields, thus it can not account for the entire observed regional subsidence. I conclude that production-induced subsidence in the Louisiana coastal zone will remain an important component of the regional subsidence picture and should be included in any regional subsidence models and in regional protection and restoration plans.

Chapter 2

Assessing elastic Coulomb stress transfer models using seismicity rates in southern California and southwestern Japan[1]

Abstract

We investigated whether observed changes in seismicity rate following the 1992 Landers and 1995 Kobe earthquakes correspond with predictions of Coulomb stress transfer models. To quantify the relationship between Coulomb stress change and seismicity rate change, we compared spatial changes in observed seismicity rates to the modeled changes in Coulomb failure stress (ΔCFS) for the two subject earthquakes. We begin with the simplest and most common ΔCFS model, which assumes that regional stress orientations are uniform and the stress change is resolved on optimally oriented strike-slip planes. We then extended the ΔCFS models to include the more geophysically realistic assumptions of spatially varying regional stress orientations and optimally oriented planes in 3D. For all the tested ΔCFS models, we found that virtually everywhere seismicity rate changes could be resolved, the rate increased regardless of whether the ΔCFS theoretically promoted or inhibited failure, and that we were not able to reliable resolve seismicity rate decreases. An improvement in the correlation between

the sign of the ΔCFS and where rate increases occur when estimating the ΔCFS on optimally oriented planes in 3D rather than 2D is a consequence of using optimally oriented planes and the ability to primarily observe rate increases. The region of positive ΔCFS increases by allowing more degrees of freedom so the correlation with positive rate change appears to increase. The areas of highest seismicity rate following the main shock did not correlate with the sign or the magnitude of the ΔCFS. Rather, the areas most active after the main shock were also the most active before the main shock.

2.1   Introduction

A primary goal of earthquake triggering studies such as this one is to develop the ability to predict where the next earthquake in a region will occur [*Freed*, 2005]. *Steacy et al.* [2005] point out the two main directions in the development of predictive tools based on Coulomb stress transfer: 1) change in probabilities of large earthquakes in a region [*Stein, et al.*, 1997; *Toda, et al.*, 1998; *Parsons, et al.*, 2000; *Parsons*, 2005; *Toda, et al.*, 2005] and 2) almost real-time assessment of areas prone to off-rupture aftershocks [*McCloskey, et al.*, 2003; *Steacy, et al.*, 2005; *Toda, et al.*, 2005], both of which have great societal importance. This work contributes to both of these directions. It addresses the first in that we are assessing whether areas show the increases or decreases in seismicity rate predicted by elastic Coulomb stress transfer as these changes in seismicity rate indicate the change in probability of large earthquakes according to the Guttenberg-Richter relationship. The work also contributes to the second direction of assessment of areas prone to off-rupture aftershocks in that if the changes in observed seismicity rate correlate with the changes in ΔCFS this can allow for estimation of regions that will be more susceptible to triggered earthquakes following a given main shock.

Shortly after the Joshua Tree-Landers-Big Bear earthquake sequence in 1992 researchers began doing studies of elastic Coulomb stress change in the area, or the change in Coulomb stress due to the static offset of the main shock, to explain the locations of aftershocks [*King, et al.*, 1994; *Stein*, 1999; *Parsons, et al.*, 2000]. These studies found aftershocks concentrated in zones with a positive change in elastic Coulomb failure stress, ΔCFS, and rare in zones where the change was negative

consistent with simple elastic Coulomb failure stress theory [*Reasenberg and Simpson*, 1992; *Stein, et al.*, 1997; *Toda, et al.*, 1998; *Stein*, 1999]. A number of studies have attempted to quantitatively correlate the changes in observed seismicity rate following a moderate to large main shock and the calculated changes in Coulomb failure stress [*Reasenberg and Simpson*, 1997; *Gross and Burgmann*, 1998; *Toda, et al.*, 1998; *Wyss and Wiemer*, 2000; *Kilb, et al.*, 2002; *Parsons*, 2002; *Marsan*, 2003; *Ogata, et al.*, 2003; *Toda and Stein*, 2003; *Lin and Stein*, 2004; *Steacy, et al.*, 2004; *Woessner, et al.*, 2004; *Ma, et al.*, 2005; *Marsan and Nalbant*, 2005; *Steacy, et al.*, 2005].

Of particular importance are the decreases in seismicity rates in areas of negative ΔCFS commonly referred to as stress shadows, which are only predicted by elastic Coulomb failure and not other triggering mechanisms, such as dynamic stresses. Such shadows were observed over broad regions following the M7.9 1857 Ft. Tejon earthquake in southern California and the M7.8 1906 San Francisco earthquake [*Reasenberg and Matthews*, 1988; *Harris and Simpson*, 1996; 1998]. However, recent detailed analyses of seismicity rates in California had difficulty identifying stress shadows following the 1989 M_W 7.0 Loma Prieta, 1992 M_W 7.3 Landers, 1994 M_W 6.7 Northridge, and 1999 M_W 7.1 Hector Mine earthquakes [*Felzer and Brodsky*, 2005]. In this study we investigated whether observed changes in seismicity rates following the M_L 7.4 1992 Landers and M_W 6.9 1995 Kobe earthquakes correspond with predictions from elastic Coulomb stress transfer models.

Breakdowns in the correlation between the seismicity rate changes and elastic Coulomb stress transfer at given length or time scales would indicate the need for incorporating more complicated time-dependent processes. In response to such observations, Coulomb stress transfer modeling has expanded beyond the simple elastic case to consider the time advance of major earthquakes by coupling of static ΔCFS with rate and state friction models [*Toda, et al.*, 1998; *Stein*, 1999], the time dependent effects of viscoelastic flow in the lower crust and upper mantle [*Freed and Lin*, 2001; *Pollitz and Sacks*, 2002; *Freed*, 2005], and poroelastic effects [*Peltzer, et al.*, 1998; *Masterlark and Wang*, 2002]. In addition to earthquakes triggered by changes in Coulomb stress due to the static offset of the main shock, dynamic stress changes from the passing of seismic

waves are also a possible mechanism for triggering events both distantly [*Hill, et al.*, 1993; *Gomberg, et al.*, 2001; *Freed*, 2005] and in the near-field [*Beroza and Zoback*, 1993; *Kilb, et al.*, 2000; 2002; *Gomberg, et al.*, 2003; *Freed*, 2005; *Felzer and Brodsky*, 2006]. In this study we restrict our analysis to the changes in elastic Coulomb failure stress caused by the static offset of the Landers and Kobe main shocks, but we also comment on how these results fit in with hypotheses of dynamic triggering in the surrounding region.

Most previous regional studies also have assumed optimally oriented strike-slip or dip-slip faults [*King, et al.*, 1994; *Toda, et al.*, 1998]. *Steacy et al.* [2005] considered optimally oriented planes in 3D based on the regional stress and the main shock stress tensors, and assumed that there was a causal relationship between the aftershocks and the change in Coulomb stress in an effort to determine the best method for computing Coulomb stress maps. We also consider optimally oriented planes in 3D, but instead explore whether using this more complicated model can predict the distribution of seismicity rate changes following the Landers and Kobe earthquakes in an effort to test the predictions of elastic Coulomb failure stress models. Calculating ΔCFS on optimally oriented planes assumes that the crust has pre-existing fractures in every orientation, and it is the fractures that are optimally oriented in the current stress field that will fail due to changes in the elastic Coulomb stress [*King, et al.*, 1994]. Additionally, previous studies of Coulomb stress change following moderate earthquakes have calculated ΔCFS assuming uniform regional background stress orientations [*King, et al.*, 1994; *Freed and Lin*, 2001; *Pollitz and Sacks*, 2002]. However, in complicated plate boundary regions where most large earthquakes occur, assuming regional heterogeneous background stresses may be more accurate. *Townend and Zoback* [2001b; 2006] used seismicity to invert for the orientation of the maximum horizontal stress, S_{Hmax}, in southern California and southwestern Japan, respectively. While there is a resolvable mean orientation of S_{Hmax}, variations are sufficiently large that they may impact the determination of optimally oriented planes for ΔCFS calculations.

In this paper we extend the work of previous studies by adding two more physically realistic assumptions: 1) the change in Coulomb stress is calculated on

optimally oriented planes in 3D and 2) the regional stress orientations are heterogeneous. We test whether incorporating these two assumptions more accurately predicts the observed changes in seismicity than the common assumptions of optimally oriented strike-slip 2D planes and a regionally uniform stress field. This will help determine if more realistic and complicated models of elastic Coulomb stress more accurately predict changes in earthquake probabilities. We also show that when using models based on slip occurring on optimally-oriented planes in 3D, the area of the region in which a positive ΔCFS is observed increases. Hence, we will present an analysis that incorporates the comparison of the percentage of the region experiencing increases (or decreases) in ΔCFS to the correlation between seismicity rate increases and the modeled change in ΔCFS.

2.2 Study areas

The Landers earthquake in southern California and the Kobe earthquake in southwestern Japan provide ideal locations to study the effect of ΔCFS on seismicity rates. Both areas are monitored by a dense seismic network facilitating the detection of seismicity rates and thus earthquake probability, which is critical due to the high population densities of the regions.
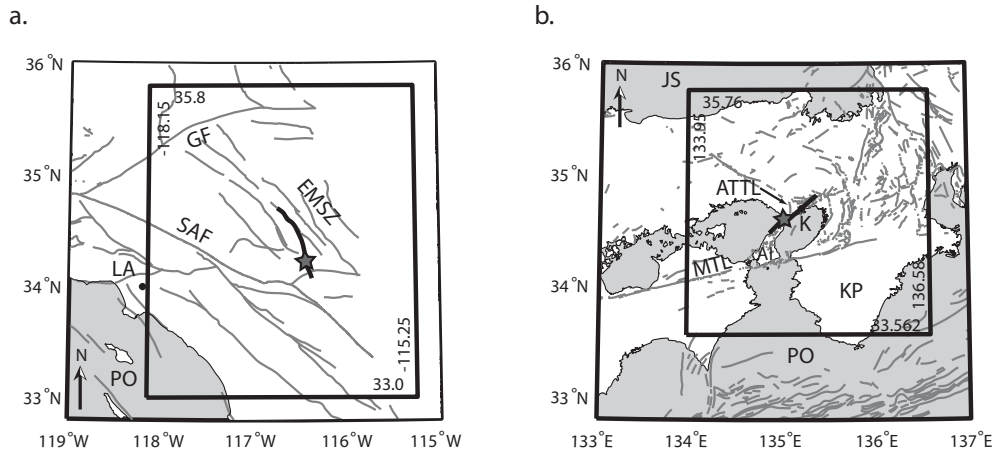
Figure 2.1: Regional maps showing the study areas for Landers and Kobe used in this study. In both maps epicenters are marked with a star and ruptures with a dark gray line. Lighter gray lines represent faults and the black box is the region used for ΔCFS calculations. a. Map of the Landers region. EMSZ: Eastern Mojave Shear Zone, GF: Garlock Fault, LA: Los Angeles, PO: Pacific Ocean, SAF: San Andreas Fault b. Map of Kobe region. ATTL: Arima-Takatuski Tectonic Line, JS: Japan Sea, K: Kobe, KP: Kii Peninsula, MTL: Median Tectonic Line, PO: Pacific Ocean

The M_L 7.4 Landers earthquake occurred in the Mojave Desert section of the San Andreas Fault (SAF) system in southern California. This area is characterized by primarily N_W striking right lateral faults sub-parallel to the SAF (Figure 2.1a). Figures 2.2a and 2.2b show the seismicity before and after the Landers main shock.

Kobe is located in southwestern Japan where the Philippine plate is subducting under the Eurasia plate. Kobe is inland from the subduction zone in an area composed principally of NE striking right-lateral, NW striking left-lateral, and north striking thrust faults (Figure 2.1b). This region has great subduction events with repeat times of ~100 years, and large strike-slip events with repeat times of ~>1000 years [*Toda, et al.*, 1998]. On January 17, 1995 a M_W 6.9 right-lateral strike slip earthquake struck the Kobe region, the strongest to hit since 1923, causing extensive damage to the city of Kobe and leaving 5,500 dead. The seismicity before and after the Kobe main shock is shown in Figures 2.2c and 2.2d.

2.3 Comparing the seismicity rate change to the change in CFS

2.3.1 *Quantifying changes in seismicity rate*

Before making a quantitative comparison of seismicity rate change and ΔCFS, we must define a metric that characterizes the change in seismicity rate and a method for defining measurement regions. In this study we use multiple methods and will show below that they yield similar results.

The β-value, as described by *Matthews and Reasenberg* [1988], is sensitive to changes in seismicity rate between two time periods in a given area. It is defined as

$$\beta\left(n_a, n_b, t_a, t_b\right) = \frac{n_a - E\left(n_a\right)}{\sqrt{\operatorname{var}\left(n_a\right)}}$$

(2.1)

where n_a and n_b are the number of events in time periods a and b, t_a and t_b are the duration of the two time periods, var is the variance and, $E(n_a) = r_b t_a$ represents the values of n_a expected under the null hypothesis of stationary random occurrence. If the variance is

represented as a binomial process, then var(n_a) = $n_b t_a$. Positive and negative values of β indicate the seismicity rate increases and decreases, respectively. The z-value is similar to the β-value in that it also measures the significance of the rate change between two time periods [*Habermann*, 1987]. However, instead of normalizing the rate change by the variance, the z-value relies on the mean and standard deviation of the rates of the two time periods, as follows:

$$z = \frac{\left(M_a - M_b\right)}{\sqrt{\left(\left(\frac{S_a^2}{n_a}\right) + \left(\frac{S_b^2}{n_b}\right)\right)}}$$

(2.2)

where M is the mean seismicity rate in each of the two time periods, a and b, S is the standard deviation of the rate, and n is the number of earthquakes. The z-value is calculated in the same way as in the ZMAP tools developed by Wyss, Wiemer, and Zúñiga for use with Matlab [*Wiemer*, 2001]. The seismicity for a given time period is binned by smaller sub-time intervals and the mean and standard deviation are calculated from the frequency counts of this binned data. Because the standard deviation is in the denominator and is normalized by the number of events in the time period having few events in the time period drives the z-value to progressively smaller numbers decreasing the significance of the rate change. A negative z-value indicates an increase in seismicity while a positive z-value indicates a decrease. The magnitude of β or z indicates the significance of the rate change based on a normal distribution. For example, a value of 1.64 is considered 90% significant for both β and z. In our analysis we considered only seismicity rate changes that are significant at the 1σ level, which is with a β-value or z-value ≥ ±1, as too few regions experienced rate changes that were significant at the 2σ level. This is primarily due to the low seismicity rates which make resolving rate changes, especially rate decreases, difficult, and is the same significance level used by *Kilb et al.* [2002]. We use 1σ to define a significant rate change in order to identify some rate decreases, but recognize that changes ≈1σ are not reliably resolved.

In addition to using the β- and z-values, we also directly compute the rate change by comparing the average rates before and after the main shock as was done by *Toda et al.* [1998]. Using this measure shows the same general results as the β- and z-values.

2.3.2 *The grid*

To calculate the change in seismicity rate for two time periods in a given area it is necessary to grid the seismicity in the region. We tested multiple gridding methods: a nearest neighbor technique [*Wyss and Wiemer*, 2000], a modified-quadtree technique [*Townend and Zoback,* 2001a; 2001b], and a uniform grid. All three produced similar results, so here we present the uniform grid, requiring a minimum number of events in each grid cell. We first specified the grid size to be 2 km per side, which is equal to the horizontal location error in the Southern California Seismic Network (SCSN) catalog for Landers and the Japan Meteorological Association (JMA) catalog for Kobe.   The grid we created is two-dimensional, with all the earthquakes projected to a single depth plane. We restricted the maximum depth of events to 20 km for Landers and 30 km for Kobe to ensure that all the events were crustal and, for Kobe, to eliminate events related to the subduction of the Philippine Sea Plate. We used all events with $M \geq 2.0$ for both Landers and Kobe, which is comparable to the magnitude of completion, M_c, determined by *Wiemer and Wyss* [2000].

In our work, the entire region is gridded and only cells that have a minimum number of earthquakes over the entire time of the catalog are kept and rate changes calculated. In southern California we require a minimum of 20 earthquakes between 1984 and 2001 to define a grid cell; in the less seismically active area around Kobe we require a minimum of 10 earthquakes between 1985 and 2001 to define a grid cell. There is little difference between the number and distribution of grid cells if only 10 earthquakes are required for Landers. The requirement of a minimum of 20 earthquakes per cell increases the potential for observing statistically significant rate changes. Conversely, at Kobe, requiring 20 earthquakes per grid cell generated too few areas where seismicity rate changes could be resolved, so a lower number of earthquakes were required. If there are fewer than the minimum number of earthquakes no grid cell is formed or rate change calculated. For each grid cell, where there at least 20 earthquakes (for Landers) or 10 earthquakes (for Kobe), we calculate the rate change for a specified time period. The only time we run into a problem is when there are no earthquakes in either the before or after period and there are enough in the other time period to define a rate change. These

changes in seismicity rate are important, and should be included. However, whenever the number of earthquakes in a time period, n, is equal to zero there is a singular value in the denominator of the z-value (for example) due to the normalization of the standard deviation by the number of events in the time period (Equation 2.2). To address this we can convert the undefined ratio of the standard deviation normalized by the number of events to either 1 or 0 when there are no events in the time period to allow the calculation to proceed. As the singularity is driven by the number of events in the denominator being zero as opposed to changes in the standard deviation making estimates of the regional variance does not solve the singularity problem. The choice of 1 or 0 to replace the singular ratio represent two end members of what the singular ratio could be replaced by. We tested both of these end member options and found that there is little difference in the results (see supplemental figure located at the end of the chapter). We proceed by assigning the singular ratio in the denominator equal to 1 in these instances.

For this study we calculated seismicity rates in various time periods beginning with the month after the main shock (the most active period of aftershocks) followed by one-year intervals, and finally by the entire time span in our catalogs after the Landers and Kobe earthquakes. The catalog used for Landers ends in 2001 at the time of the Hector Mine earthquake. The catalog for Kobe also ends in 2001 as that was the end of the available data. Background rates were defined by seismicity in the 8 to 10 years before the main shock, however the results did not change significantly if we use only half of that time to define the background, indicating that the background seismicity rate is relatively stable over the entire pre-main shock period. The grids with the seismicity rate changes calculated using both the β- and z-values for Landers and Kobe appear in Figures 2.3b, 2.3c, 2.3e, and 2.3f.

These rate changes are used in all comparisons to the various ΔCFS models. In all cases we are unable to reliably resolve seismicity rate decreases. We do not ignore the few occasions when rate decreases are observed, but focus our analysis on the rate increases and their correlation with ΔCFS. Studies performed by *Wyss and Wiemer* [2000] show that they were able to resolve areas of decreased seismicity in the same areas as the lobes of negative ΔCFS. The main difference between their technique and

ours is that they use a nearest-neighbor gridding technique, which in areas of low seismicity causes the searched region around the node to increase in order to encompass enough data to calculate a rate change. While this gridding technique does allow for resolving areas of seismicity rate decrease in regions of low seismicity (which we are unable to do with the uniform grid cell size) it runs the risk of artificially imposing rate changes with no seismicity, because of the smoothing effects of the large overlapping circles allowing individual earthquakes to be used to calculate rate changes at multiple nodes. *Wyss and*
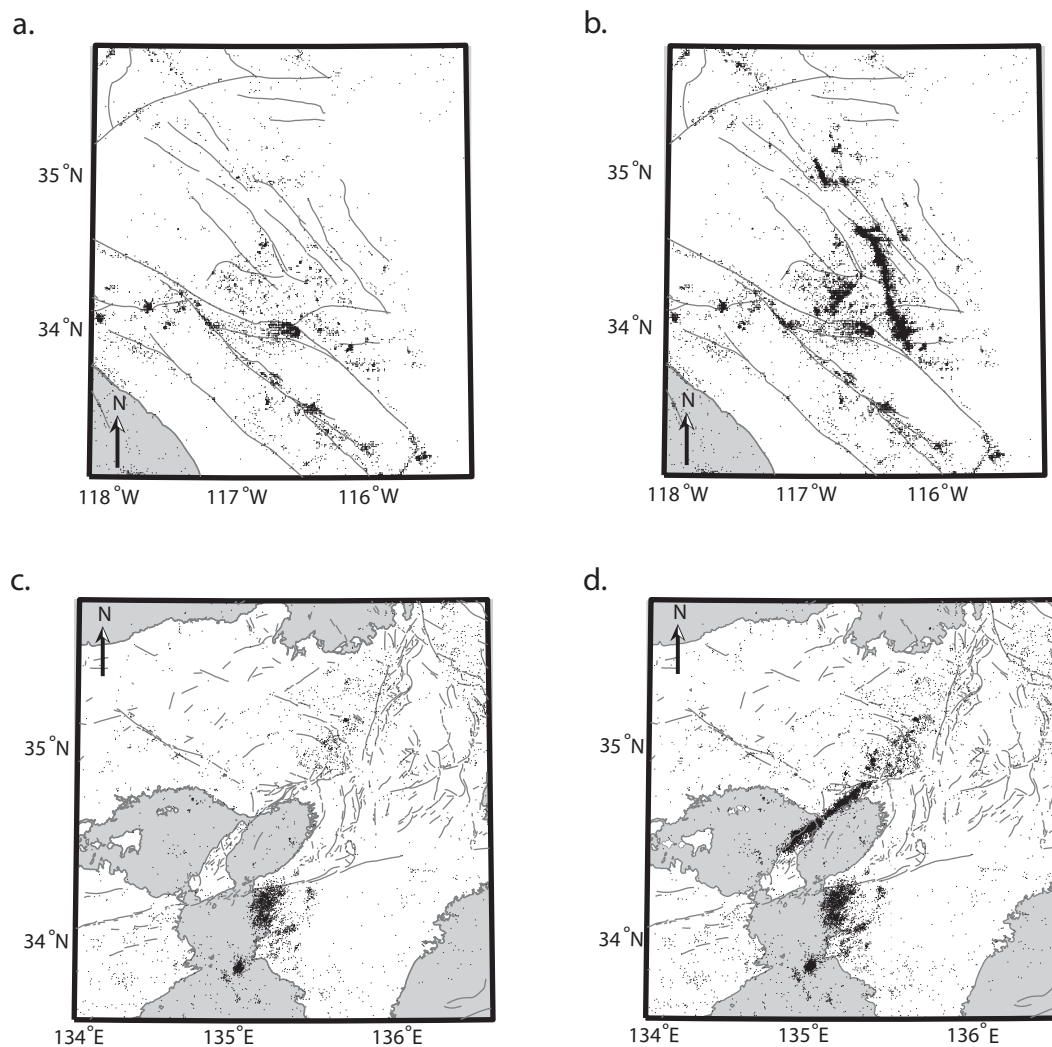
Figure 2.2: Seismicity for the study area a. before and b. after the 1992 M_L 7.4 Landers earthquake and c. before and d. after the 1995 M_W 6.9 Kobe earthquake.

Wiemer [2000] found that at ~ 70% of the nodes the sign of the seismicity rate change matched the sign of the Coulomb stress change, and they were able to resolve decreases in seismicity rate. However, when we performed our quantitative statistical analysis using the same gridding technique (nearest-neighbor) and time periods as *Wyss and Wiemer* [2000] we found that at ~40-70% of the nodes the sign of the seismicity rate change matched the sign of ΔCFS. While the nearest neighbor technique did allow seismicity rate decreases to be resolved, in many of these areas the seismicity is sufficiently low that the circle surrounding the node was so large as to include seismicity associated with a different ΔCFS. *Marsan and Nalbant* [2005] discuss the problems with using this method for gridding if the goal is to detect seismicity shadows and observe that a different procedure must be adopted in order to reliably detect shadows.

2.3.3 *Calculating the change in Coulomb failure stress*

The change in Coulomb failure stress is defined as

$$\Delta\sigma_f = \Delta\tau_\beta - \mu'\Delta\sigma_\beta$$

(2.3)

where τ_β is the shear stress on the failure plane oriented at β to the σ_1 axis (positive in the direction of fault slip), σ_β is the normal stress (positive for compression), and μ' is the effective coefficient of friction, which includes pore pressure effects [*King, et al.*, 1994; *Harris*, 1998]. The orientation of the failure plane, β, is determined by the combination of the regional background stress and the coseismic stress change from the main shock [*King, et al.*, 1994]. A positive ΔCFS indicates an increased tendency towards slip in the direction of interest (defined by the sign on τ_β), whereas a negative ΔCFS indicates a reduction in the tendency to slip.

In this study we used the program DLC written by Robert Simpson [*Parsons, et al.*, 1999], which is based on the subroutines of *Okada* [1992] for an elastic half-space, because it is more versatile than the commonly used Coulomb 2.6 software package [*Toda, et al.*, 1998] and allows for complicated and realistic models of regional stress. Using the slip model for the June 28, 1992 Landers earthquake determined by *Wald and Heaton* [1994], we modeled the ΔCFS on optimally oriented strike-slip planes, assuming

μ' = 0.4 and a regional stress of N7E (Figure 2.3a). These are the same parameters used by *King et al.* [1994]. Since the Joshua Tree and Big Bear earthquakes were close to the Landers event both temporally and spatially, the slip from these events is included in our calculations of ΔCFS. In addition, for a strike-slip main shock the calculations of ΔCFS do not vary much over depth, so ΔCFS was calculated on optimally oriented faults at 7.5 km depth (the middle of the seismogenic zone). In Figure 2.3a note that, as pointed out by *King et al.* [1994], the aftershocks appear to be concentrated in areas where ΔCFS is positive (red) and absent where ΔCFS is negative (blue).

Figure 2.3d shows the ΔCFS model for the Kobe main shock using the *Wald* [1996] slip model on optimally oriented strike-slip planes, assuming μ' = 0.4 and a regional stress orientation of N90E, the same parameters as used by *Toda et al.* [1998]. We resolved the change in stress on planes at a depth of 10 km (the center of the crustal seismogenic zone), since the main shock was predominately strike-slip the ΔCFS does not vary much with depth. While the correlation between ΔCFS and seismicity is not as clear as for Landers, *Toda et al.* [1998] performed statistical tests and claimed that Coulomb stress transfer is able to explain the spatial distribution of aftershocks following the Kobe earthquake.

2.3.4 *Quantitative comparison of changes in ΔCFS and in seismicity rate*

Although visual comparison of the changes in seismicity rate to the calculated ΔCFS shown in Figure 2.3a and 2.3d appear to be qualitatively comparable, for each location where we calculated ΔCFS, we can quantitatively test whether the seismicity rate change has the same sign. We compared these two values by plotting them against each other, with the ΔCFS on the x-axis and seismicity rate change on the y-axis (we will refer to these plots as "quad-plots") [*Reasenberg and Simpson*, 1992]. For example, if a grid cell that had an increase in seismicity rate is located in an area of increased ΔCFS, then it would plot in the upper right quadrant, and a grid cell with a decrease in seismicity rate located in an area of decreased ΔCFS will plot in the lower left quadrant. Thus, if the

changes in seismicity rate perfectly followed what elastic Coulomb stress transfer theory predicts, all the points would be in the upper right and lower left quadrants. At this point we are only interested in whether increases in seismicity rate correspond to increases in CFS, or vice versa, and not any linear relationship between the magnitude of CFS and rate change.

The quad-plot method of comparing changes in seismicity rate and ΔCFS is similar to comparing the percentage of events consistent with triggering [*Hardebeck, et al.*, 1998; *Kilb, et al.*, 2002] and using the correlation coefficient between areas of stress increase and seismicity [*Steacy, et al.*, 2005], but offers some advantages over both of these methods. We chose the quad-plot method because, in addition to finding what percentage of grid cells are consistent with triggering, it provides insight into both the potential relationship between the magnitude of Coulomb stress change required for triggering (or suppression) and any direct relationship between the magnitude of Coulomb stress change and the magnitude of the seismicity rate change. In addition, the quad-plots do not restrict us to identifying areas simply consistent with triggering (increases in seismicity and in ΔCFS) but allow us to consider stress shadows (the correlation coefficient used by *Steacy et al.* [2005] does not).

For all the quad-plots we restricted the analysis to regions with values of ΔCFS between ±5 bars, which effectively eliminates the area within ~15 km of the rupture where details in slip distribution can have a large effect on the ΔCFS calculation, similar to *Toda et al.* [1998]. Previous studies that used this technique to compare seismicity rate change and ΔCFS used the χ^2 statistic with a 4-fold table[*Reasenberg and Simpson*, 1997; *Toda, et al.*, 1998]; however, since we are unable to resolve seismicity rate decreases in many cases, there are quadrants with no data points in them (Figures 2.4, 2.5, and 2.6) making the χ^2 statistic inappropriate. Instead we simply calculate the percentage of points in each quadrant.
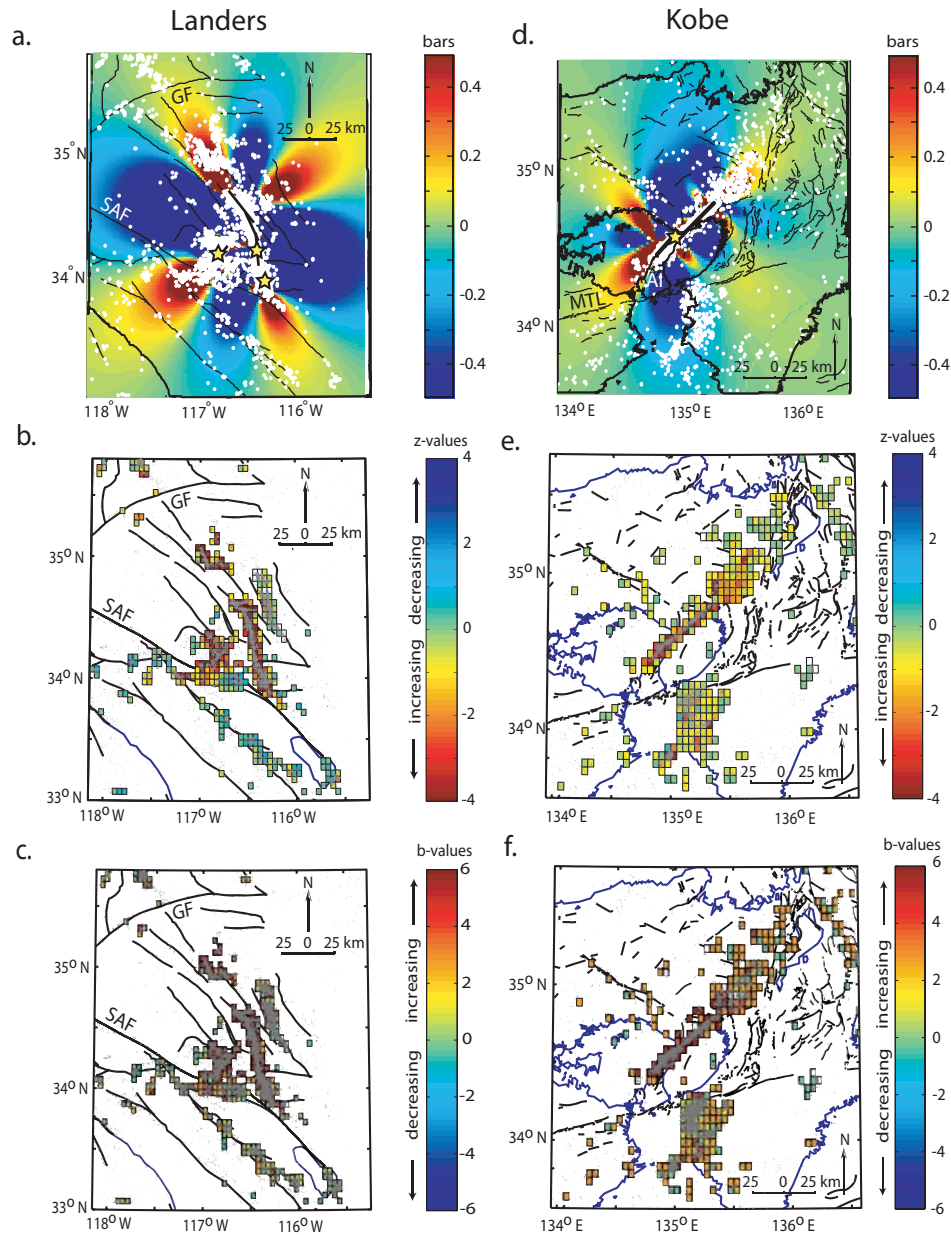
Figure 2.3: Elastic Coulomb stress and seismicity rate changes for Landers and Kobe a. Elastic Coulomb Stress change from Landers earthquake using rupture model of *Wald and Heaton* [1994] on optimally oriented strike-slip planes assuming a uniform regional stress orientation of N7E. Warm colors indicate an increase in CFS, cool colors a decrease. Yellow stars indicate the epicenters of the Joshua Tree, Landers and Big Bear earthquakes. SAF: San Andreas Fault, GF: Garlock Fault b. Seismicity rate change following Landers earthquake using the z-value. Grid cells defined using seismicity from 1984-2000. Background rate determined by 1984-1992 compared to 1992.6-1993.6. c. Seismicity rate change following Landers earthquake using the β-value. d. Elastic Coulomb Stress change from the Kobe earthquake using rupture model of *Wald* [1996] on optimally oriented strike-slip planes assuming a uniform regional stress orientation of N90E. Warm colors indicate an increase in CFS, cool colors a decrease. Yellow star indicates the epicenter of the Kobe earthquake. K: Kobe, AI: Awaji Island e. Seismicity rate change following the Kobe earthquake using z-value. Grid cells defined using seismicity from 1985-2001. Background rate determined by 1985-1994.9 compared to 1995-1996. f. Seismicity rate change following the Kobe earthquake using β-value.

2.4   The simple ΔCFS model: Optimally oriented strike-slip planes and a uniform regional stress orientation

We first tested the models of ΔCFS shown in Figures 2.3a and 2.3d to see how accurately they predicted the observed changes in seismicity rate change. These models have the same parameters as the models published in *King et al.* [1994] for Landers and *Toda et al.* [1998] for Kobe. These studies concluded that the ΔCFS accurately predicts the location of aftershocks. Figure 2.7 illustrates the comparisons between the observed seismicity rate changes for the first year after the Landers and Kobe main shocks calculated using both the β- and z-values and the modeled ΔCFS. As *Freed* [2005] points out, it can be difficult to resolve seismicity rate decreases because they need to occur in an area of active seismicity before the main shock (if there are few earthquakes in a region before the main shock, we cannot resolve any decreases in seismicity rate). However, in our study there are still a large number of grid cells in areas of negative ΔCFS and thus we can examine the extent to which rate increases occur where Coulomb stress transfer theory predicts there should be decreases in seismicity rate.

With the uniform grid, large portions of the study areas for both Landers and Kobe do not have sufficient seismicity to either define a grid cell or to calculate a significant change in seismicity rate. This is similar to what was observed by both *Kilb et al.* [2002] and *Toda et al.* [2005] for Landers and by *Toda et al.* [1998] for Kobe. The simplest explanations for this observation are that the change in Coulomb stress was not large enough to induce a change in seismicity rate, or that the background rate was too low to detect a change. However, there appears to be no correlation between the magnitude of ΔCFS and observed seismicity rate changes (Figure 2.2). *Toda et al.* [2005] also noticed this lack of correlation between ΔCFS magnitude and seismicity rate changes and argued that only areas that have high background seismicity will respond to changes in the Coulomb stress, regardless of magnitude. If there is no correlation between the magnitude of stress change and seismicity rate changes, it implies that the areas with no rate changes either have faults that are too far from failure to be triggered

by the perturbed stress state (i.e., locked), no faults, or low ambient loading rates so that the background rate is too low to detect a change. We will focus the rest of our work on the regions that have sufficient seismicity to resolve rate changes to test the static stress triggering hypothesis.

Figures 2.4 and 2.5 show the quad-plots of z-values versus ΔCFS for all time periods calculated. For the remainder of the paper we will show only the quad plot for the first year, which begins one month after the main shock. This is because when the first month of seismicity following the main shock is included the increases in seismicity rate observed are strongly influenced by the very high seismicity rates over the entire region immediately following the main shock due possibly to dynamic stresses which radiate in all directions form the main shock. In addition, it is in this time period when the catalog becomes saturated and one needs to be concerned with a change in the magnitude of completion. We begin the first year's analysis following the first month after the main shock because it is long enough after the main shock that changes in the magnitude of completion should not affect the calculations, stress shadows (if present) can be resolved [*Marsan*, 2003; *Marsan and Nalbant*, 2005], and it is a short enough time after the main shock that non-elastic effects such as viscoelastic flow of the lower crust and upper mantle should have very little to no effect. By considering the first month following the main shock separately we do omit the largest seismicity rate change signal from the first year of data, however, the first month of activity dominates the changes in seismicity rate for the first year, and decreases the possibility of observing any seismicity rate decreases. We did test various time lengths following the main shock to optimize the detection of seismicity rate changes including shadows and found that after the first month following the main shock there is little change in the correlation between seismicity rate and ΔCFS. Also, during the time period considered the seismicity rates are still high enough to resolve significant rate changes if present. In the years following the main shock, the distribution of points in the various quadrants of the plot is not significantly different from what could be expected for a random distribution of earthquakes in time for a catalog with no large earthquake. Part of what is contributing to

this decrease in being able to resolve significant rate changes is that the z- and β-values are inaccurate measures when there are too few earthquakes [*Marsan and Nalbant*, 2005].
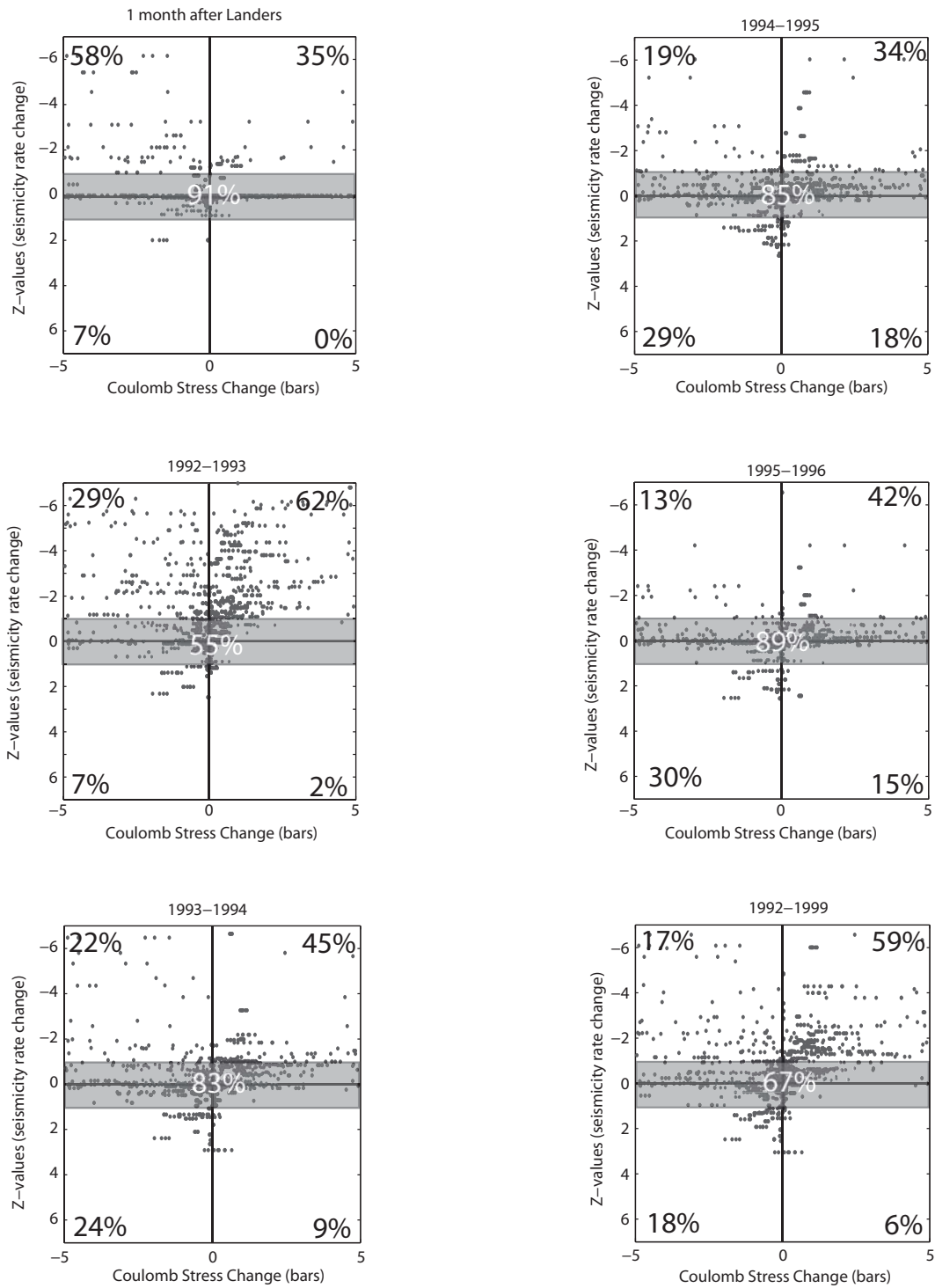
Figure 2.4: Quad-plots illustrating the relationship between seismicity rate change, expressed as z-value, and ΔCFS following the Landers earthquake. The shaded area indicates rate changes with less than 1σ significance and the percentage of all cells in that region. The remaining percentages indicate what percentage of cells with a significant rate change fall into each quadrant.
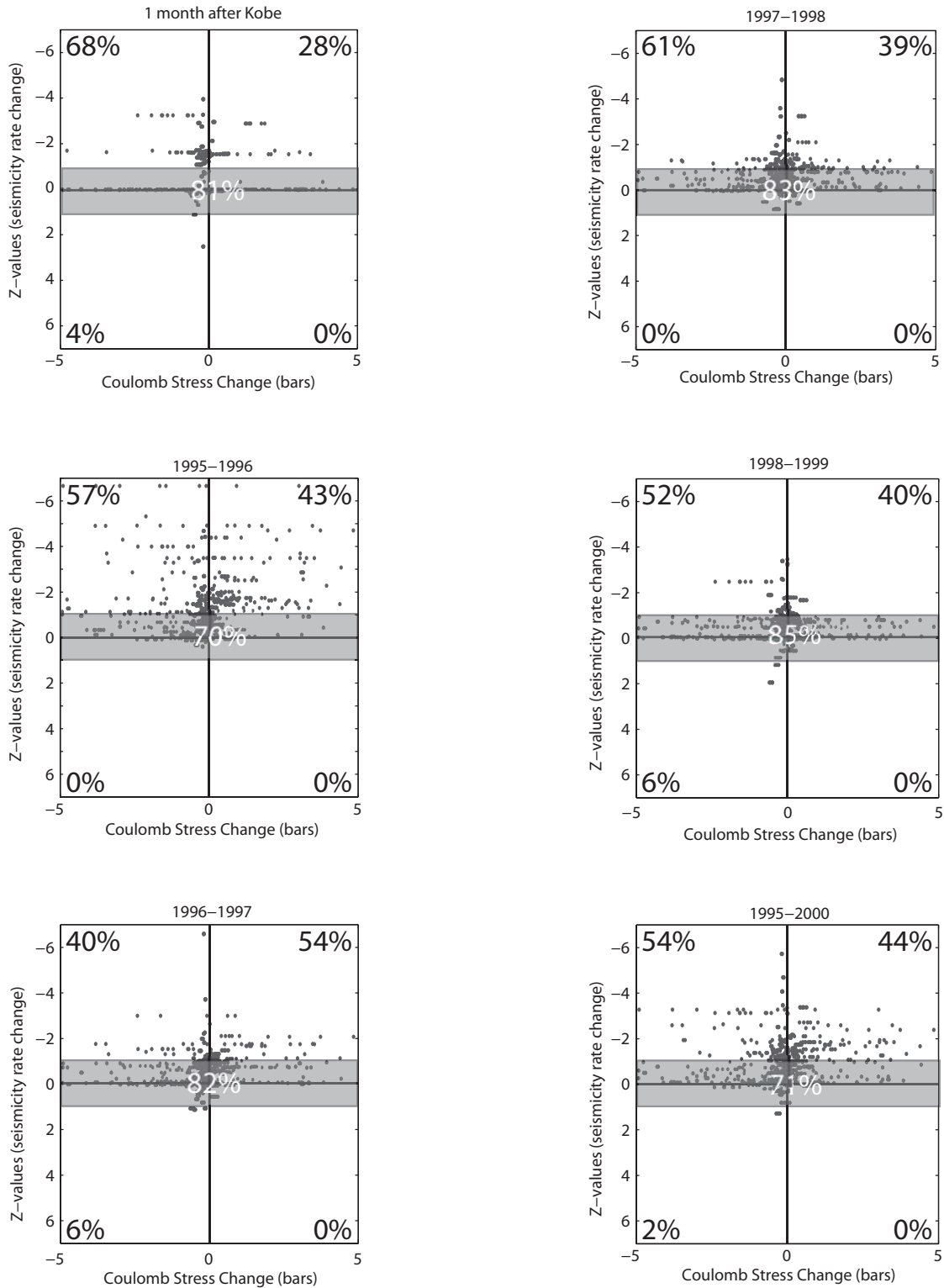
Figure 2.5: Quad-plots illustrating the relationship between seismicity rate change, expressed as z-value, and ΔCFS following the Kobe earthquake. The shaded area indicates rate changes with less than 1σ significance and the percentage of all cells in that region. The remaining percentages indicate what percentage of cells with a significant rate change fall into each quadrant.

However, if we quantify the rate change as simply R/r, where R is the mean rate after the main shock and r is the mean rate before [*Toda, et al.*, 1998], and create the quad plots the distributions are very similar to those seen in the first year for all the time periods. Quad-plots using this metric are shown for Landers as an example in Figure 2.6. Figure 2.7 shows the quad-plots using the R/r metric for a random catalog. This catalog was created by randomizing the seismicity in the Landers region between 1982 and 1999 in time while maintaining the spatial distribution and calculating the rate change for the same time periods as in the Figure 2.6. The overall distribution of points in the quadrants is not significantly different than the data (a result of maintaining the spatial distribution of events), however, the magnitude of the seismicity rate change in the random catalog is substantially lower. For the random catalog the rate changes fluctuate around zero, whereas there are substantial rate increases following the main shock in the data indicating the there are more earthquakes following the main shock compared to a random catalog.

Figure 2.8 and Table 2.1 show the results of comparing the seismicity rate change for the first year following the Landers and Kobe main shocks using both the z- and β-value to characterize seismicity rate changes to the calculated ΔCFS for the simple model of optimally oriented strike-slip planes with a uniform regional stress orientation. While anywhere from 43-62% of the cells show an increase in seismicity rate when ΔCFS is positive, as Coulomb theory predicts, 29-57% of the cells show an increase in seismicity associated with a decrease in ΔCFS. Less than 10% of the cells for Landers show a decrease in seismicity rate, and no cells for Kobe show a decrease in seismicity rate, despite having sufficient seismicity in areas of negative ΔCFS to define significant changes in seismicity rate. At Kobe much of the area of increased seismicity associated with negative ΔCFS is dominated by the cluster of seismicity south of the Kobe rupture on the Kii Peninsula (Figures 2.3e and 2.3f), which is an area typified by thrust faulting, thus optimally oriented strike-slip planes are likely not accurately modeling the planes that are active. This may account for the large percentage of cells showing an increase in seismicity rate associated with a negative ΔCFS and provides strong motivation to incorporate optimally oriented planes in 3D and regionally heterogeneous stress orientations.

Overall we found that the "standard" model of elastic ΔCFS is generally unable to fit the observed changes in seismicity rate. At Landers, where significant rate changes can be resolved ~60-70% of grid cells show an increase in seismicity associated with positive ΔCFS, less than 10% show a decrease in rate associated with negative ΔCFS, and 30-40% (depends of z- or β-value) show an increase in seismicity rate associated with negative ΔCFS. At Kobe the results are even more dramatic as seismicity rate decreases are never resolved and there are more seismicity rate increases in areas of decreased ΔCFS than increased ΔCFS. These observations led us to consider slightly more complicated ΔCFS models in order to test whether these changes could improve the fit of the observed rate changes to the models. Since we are unable to resolve seismicity rate decreases with confidence, and over 90% of the grid cells with significant rate changes were showing increases in seismicity rate, we will focus on the seismicity rate increases in the comparison of the more complicated ΔCFS models to the seismicity rate changes in the following sections. Furthermore, since the quad-plots using the z-value and the β-value are similar, for the remaining models in this paper we only present results using the z-value.
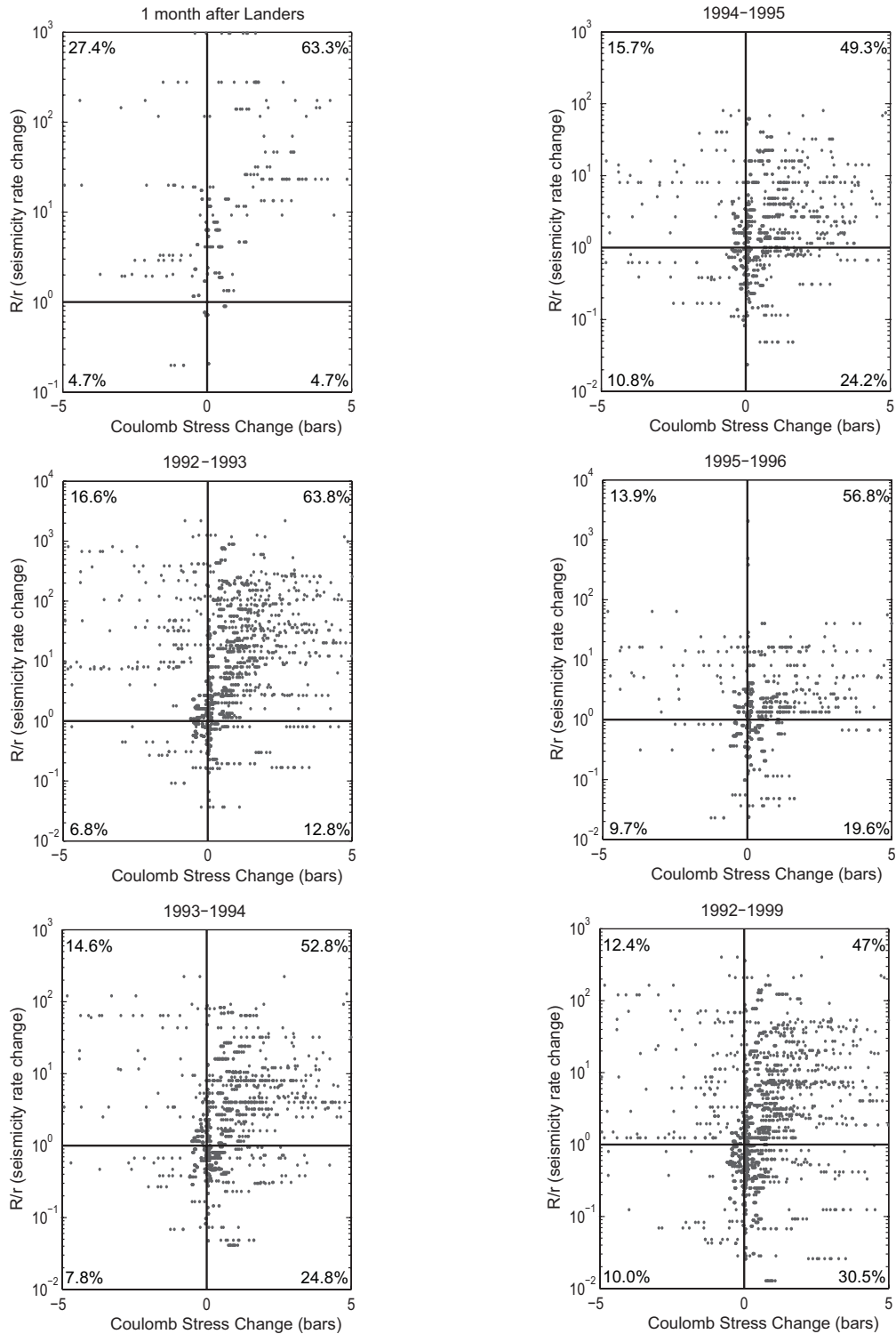
Figure 2.6: Quad-plots for Landers defining seismicity rate changes as the ratio of the average rates before and after the main shock as described in *Toda et al.* [1998]. R is the average seismicity rate after the main shock and r is the average seismicity rate before the main shock. The quad-plots using this metric for representing seismicity rate change give the same results as the quad-plots using the z-value and β-value for both Landers and Kobe.
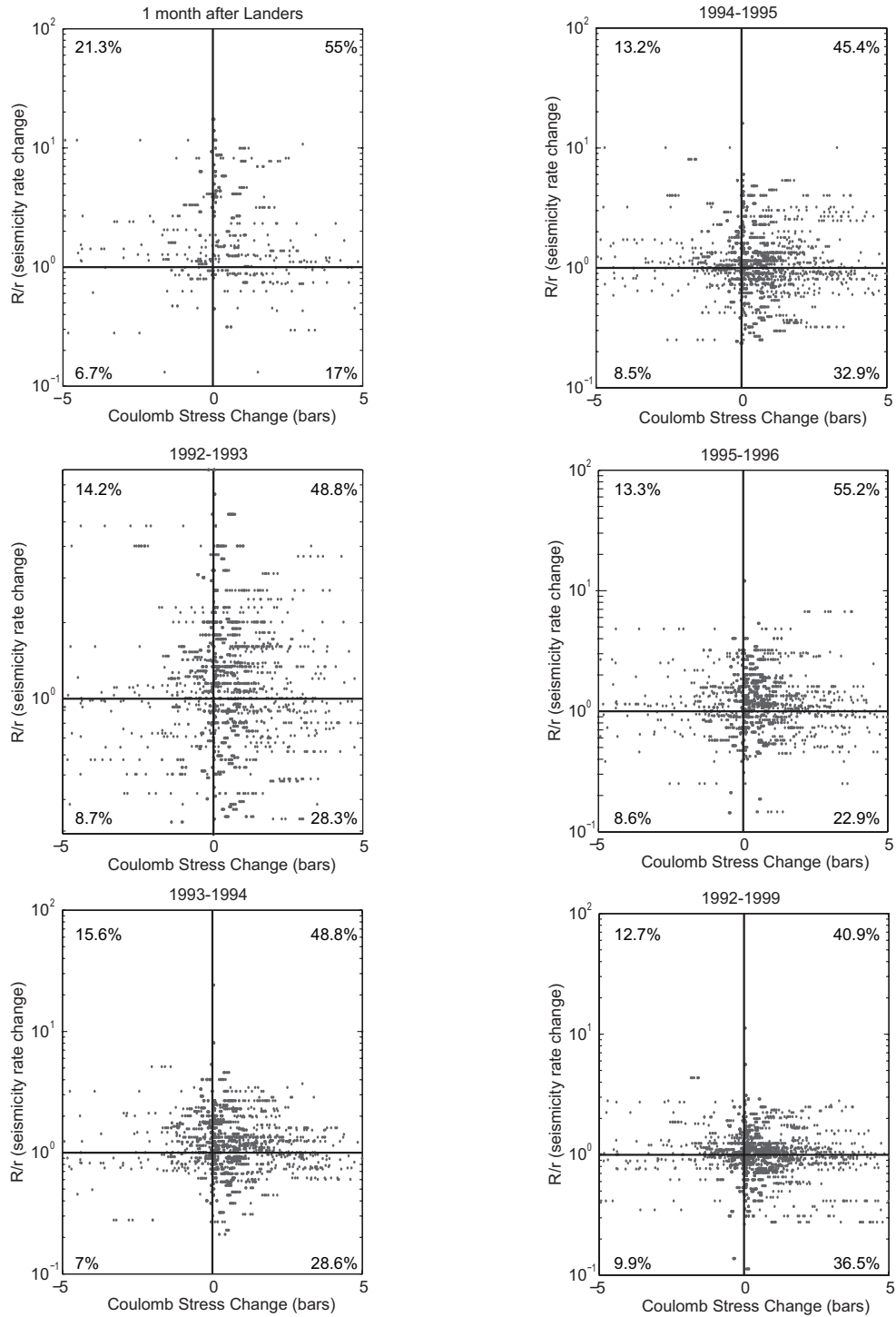
Figure 2.7: Quad-plots for Landers using a randomized seismicity catalog and defining seismicity rate changes as the ratio of the average rates before and after the main shock as described by *Toda et al.* [1998]. R is the average seismicity rate after the main shock and r is the average rate before the main shock. The seismicity catalog from 1982-1999 is randomized in time while maintaining the spatial distribution of events, and seismicity rate changes are calculated using the same time intervals as in Figure 6. While the overall distribution of points in the quad-plot is similar for the random catalog compared to the data, the magnitude of the rate changes are substantially smaller for the random catalog.
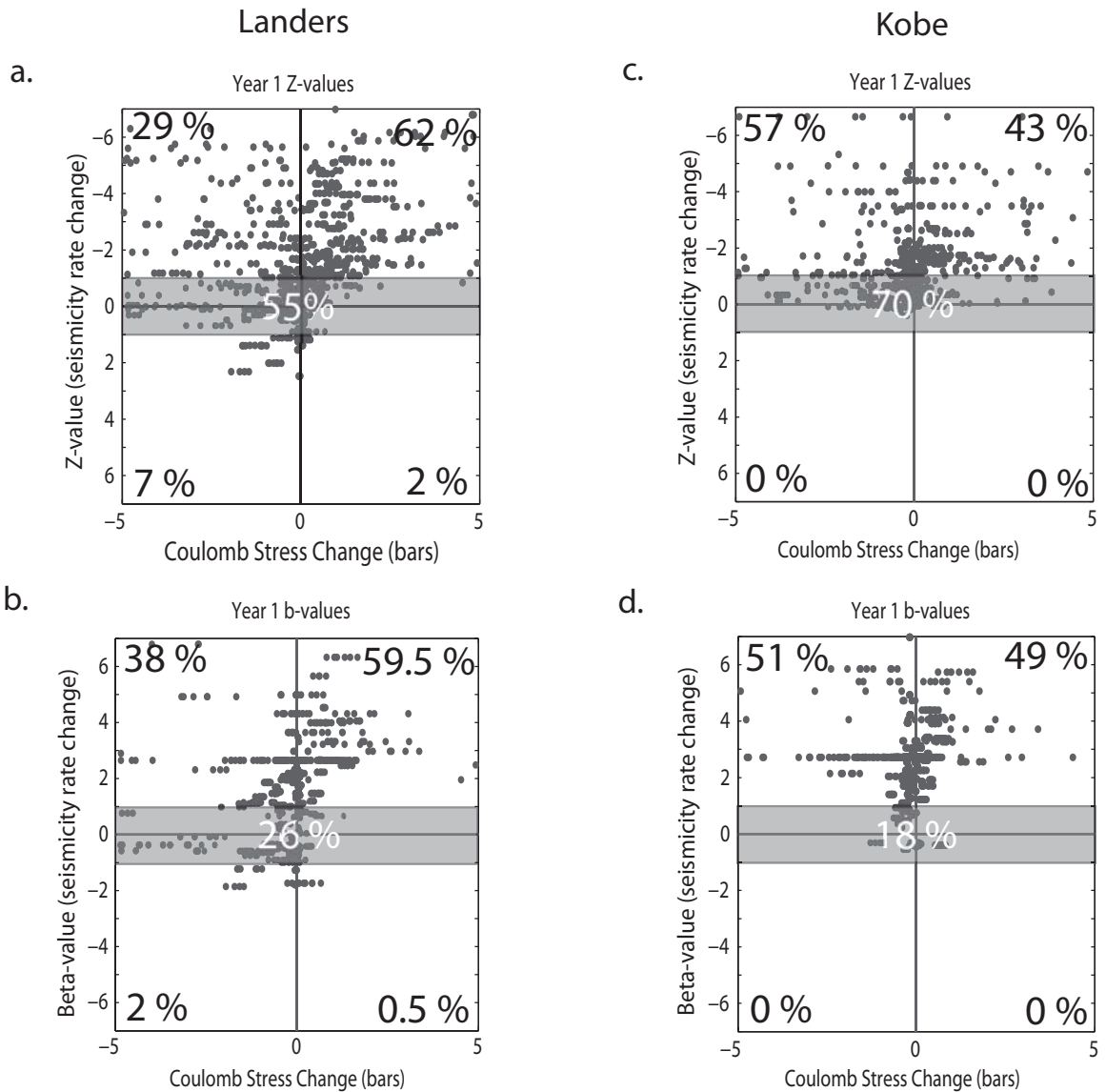
Figure 2.8: Changes in Coulomb failure stress vs. seismicity rate change for the ΔCFS model assuming optimally oriented strike-slip planes and a uniform regional stress orientation.   a. For the first year after the Landers main shock using z-value to quantify seismicity rate change, 55% of all the grid cells do not have a significant seismicity rate change (points in the gray box).   The percentages in the remaining quadrants represent the percentage of grid cells that have a significant change in seismicity rate. b. Quad-plot for Landers using the β-value to quantify the seismicity rate change. c. Quad-plot for Kobe using the z-value to quantify seismicity rate change. d. Quad-plot for Kobe using the β-value to quantify the seismicity rate change.

29

Landers		
	z-value	β-value
ΔCFS>0, ISR	62%	59.50%
ΔCFS>0, DSR	2%	0.50%
ΔCFS<0, ISR	29%	38%
ΔCFS<0, DSR	7%	2%
no significant rate change	55%	26%

Kobe		
	z-value	β-value
ΔCFS>0, ISR	43%	49%
ΔCFS>0, DSR	0%	0%
ΔCFS<0, ISR	57%	51%
ΔCFS<0, DSR	0%	0%
no significant rate change	70%	18%

Table 2.1: Results comparing the seismicity rate changes observed in the first year following the Landers and Kobe main shocks for both the z-value and the β-value compared to ΔCFS for the simple Coulomb stress model of optimally oriented strike-slip planes and a uniform regional stress orientation (also shown in Figure 8). ΔCFS >0 indicates areas with an increased tendency to slip, while ΔCFS<0 are less likely to slip. ISR: increased seismicity rate, DSR: decreased seismicity rate. The results using the z and β-value are qualitatively the same, so we use only the z-value for the remainder of the paper.

2.5 Extending the simple Coulomb failure stress models

In regions such as Landers and Kobe, where the stress state is strike-slip/thrust, the planes failing are both vertical and dipping. By considering optimally oriented planes in 3D, the portion of the region experiencing a positive ΔCFS may increase. This is because the areas that are modeled to have a positive ΔCFS for the optimally oriented strike-slip case will remain the optimally oriented planes, and thus retain the positive ΔCFS. However, in areas where the ΔCFS was negative in the strike-slip case the

optimally oriented plane in 3D may be a dip-slip plane that is modeled to experience an increase in ΔCFS. By increasing the percentage of the area experiencing a positive ΔCFS the observed seismicity may better fit the elastic ΔCFS. There is always the concern that by using optimally oriented planes a bias in the distribution of ΔCFS towards positive values is introduced. This would be of greater concern in our study if there were significant regions of decreased seismicity rate in areas of increased ΔCFS, and the optimally oriented planes were different than the average mechanism of the events. In both our study areas neither of these cases is present, so any bias introduced due to optimally oriented planes does not change the general observations and conclusions of this study.

Next, we consider heterogeneous background regional stress orientations and calculated the ΔCFS on both optimally oriented vertical strike-slip planes and optimally oriented planes in 3D. In the next three sections we describe the motivation behind these additions to the ΔCFS models, discuss the methods, and finally present the results of the comparisons of the new models to the observed changes in seismicity rates.

2.5.1 *Optimally oriented planes in 3D with regionally uniform stress orientations*

Geologic, seismologic, and stress indicators show that the Landers and Kobe regions are in a strike-slip/thrust faulting regime. At Landers the majority of focal mechanisms are strike-slip, but a significant percentage of the mechanisms are thrust, and there is even the occasional normal mechanism. The strike-slip and thrust mechanisms are distributed throughout the region while the normal mechanisms are concentrated in two localized clusters, one near Cajon Pass, where *Zoback and Healy* [1992] and *Weldon and Springer* [1988] discuss localized normal faulting, and the other is near the Garlock fault in the northern part of the region. The study of Kobe by *Toda et al.* [1998] used optimally oriented strike-slip planes for most of the region, but optimally oriented dip-slip planes on the Kii peninsula south of Kobe, which has a cluster of persistent seismicity (Figures 2.2c, 2.2d and 2.3d). However, while this cluster of seismicity is characterized by diverse mechanisms, it is not the only part of the Kobe region to have

dip-slip mechanisms. The variety of focal mechanisms present in both the Landers and the Kobe regions indicates that the assumption of optimally oriented strike-slip planes is not valid. Thus, we allow the DLC program to choose optimal planes in 3D, which allows for both strike-slip and dip-slip motion on optimally oriented planes in the region and removes the human element of choosing different optimally oriented planes for various regions.

In general to calculate ΔCFS on optimally oriented planes in 3D, it is necessary to know ϕ, the ratio of the difference between the intermediate (S_2) and minimum (S_3) principal stress magnitudes to the differential stress, in order to define the rake of the slip vector on the optimally oriented planes. This ratio is defined by *Angelier* [1989] as:

$$\phi = \frac{S_2 - S_3}{S_1 - S_3}$$

(2.4)

We can still correctly calculate the sign of the CFS change (but not the magnitude) without incorporating ϕ into the ΔCFS calculation, assuming that the region is uniaxial compressive (which is valid for a strike-slip/thrust regime, as $S_{Hmax} > S_v \geq S_{hmin}$). This is useful because we are considering regions that are in a strike-slip/thrust faulting regime, and are only interested in whether increases in seismicity rate correlate with increases in ΔCFS.

Figures 2.9a and 2.9c illustrate ΔCFS resolved on optimal planes in 3D in a uniform stress field. The most significant change from previous models (Figures 2.3a and 2.3d) is that the regions of positive ΔCFS have expanded to include much of the area surrounding the rupture, practically eliminating the off-fault areas of negative ΔCFS. The 3D optimally oriented planes for Landers do not change in most places, except in some of the off-fault lobes where they become dip-slip. This change in optimally oriented planes is what contributes to the region experiencing primarily positive ΔCFS. The areas modeled to have dip-slip optimally oriented planes better capture the thrust and normal mechanisms observed in the LA basin and near Cajon Pass respectively. For Kobe, the 3D approach adds dip-slip planes primarily to the south of the main shock rupture, which

more accurately captures the area of high seismicity on the Kii Peninsula where dip-slip mechanisms are common. This observation is apparent in the quantitative comparison of
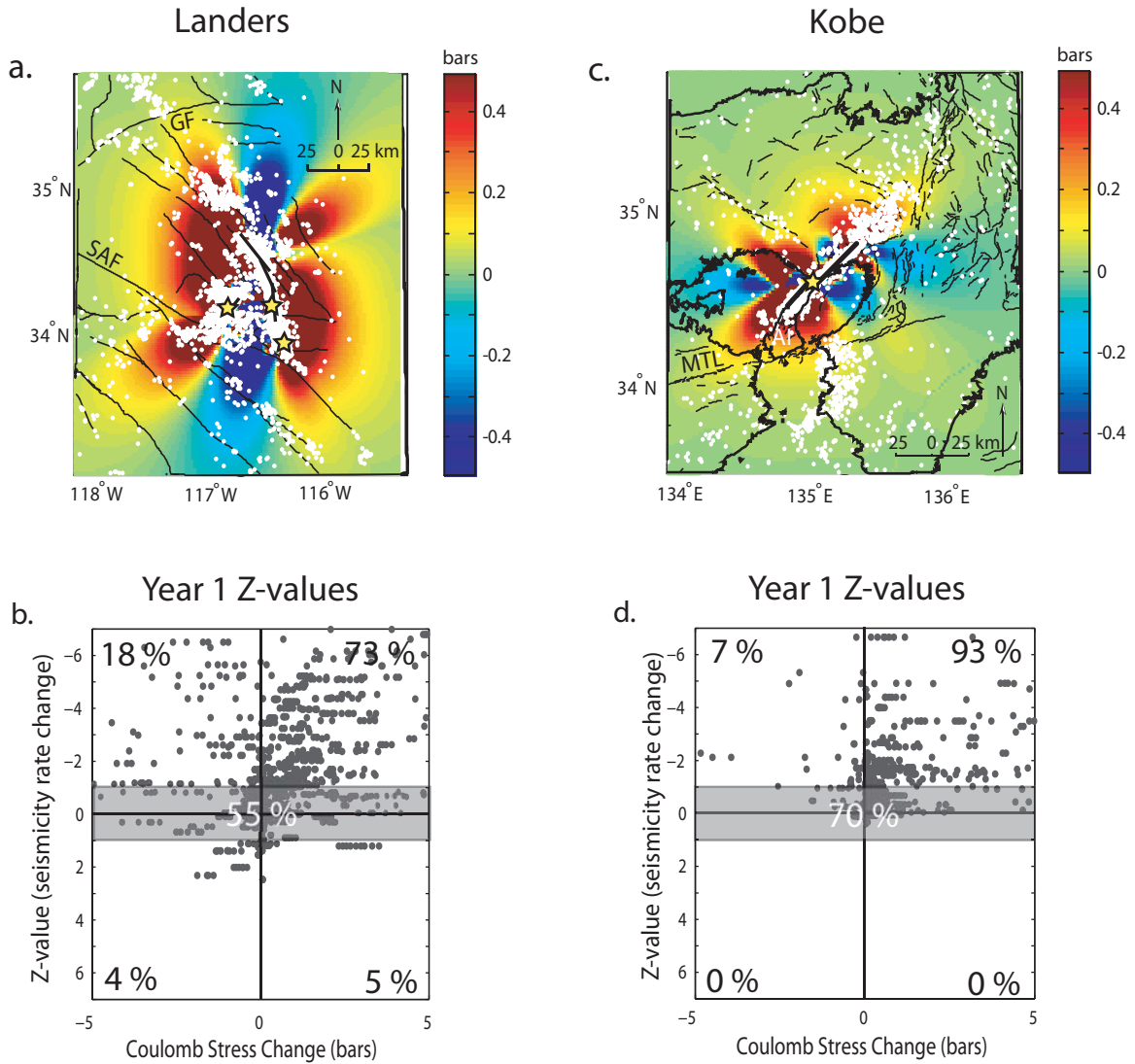
Figure 2.9: Coulomb stress change in 3D and associated quad-plots for Landers and Kobe. a. Elastic Coulomb stress changes from the Landers earthquake using rupture model of *Wald and Heaton* [1994] on optimally oriented planes in 3D assuming a uniform regional stress orientation of N7E. b. Quad-plot for Landers using the z-value to quantify the seismicity rate change for year 1. c. Elastic Coulomb stress changes from the Kobe earthquake using rupture model of *Wald* [1996] on optimally oriented planes in 3D assuming a uniform regional stress orientation of N90E. d. Quad-plot for Kobe using the z-value to quantify the seismicity rate change for year one.

ΔCFS with the observed seismicity rate changes, as shown in Figures 2.9b and 2.9d. For Landers, for the cells that show a significant seismicity rate change, 72% show an increase in seismicity associated with an increase in CFS, and 17% show an increase in

seismicity rate associated with a decrease in CFS. For Kobe, of the cells that show a significant rate change, 93% show an increase in seismicity and CFS while only 7% show an increase in seismicity rate associated with a decrease in CFS. This appears to be a significant improvement over the correlations seen with the ΔCFS model for optimally oriented strike-slip planes. However, as we will show, the relationship between the improved apparent fit and the increase in the percentage of the region experiencing an increase in CFS is important.

2.5.2 *Varying the regional stress field*

All previous studies of Coulomb stress change after an earthquake assumed a uniform regional background stress orientation [*King, et al.*, 1994; *Freed and Lin*, 2001; *Pollitz and Sacks*, 2002]. *Townend and Zoback* [2001b], similar to *Hardebeck and Hauksson* [2001], used seismicity and a recursive gridding algorithm to invert focal mechanisms to determine the orientation of S_{Hmax} (the maximum horizontal stress) in Southern California. While the overall maximum horizontal stress direction is NE-SW, as is assumed in regionally uniform models, upon close inspection the stress field varies through the region. *Townend and Zoback* [2001b] found that the orientation of S_{Hmax} is approximately N30˚E in the eastern Mojave and almost due north in the western Mojave and LA basin (Figure 2.10a). This rotation of S_{Hmax} encompasses the region affected by the Landers earthquake.

The orientation of S_{Hmax} in the Kobe region is generally east-west [*Tsukahara and Kobayashi*, 1991; *Townend and Zoback*, 2006] . While the S_{Hmax} orientation in this area has been noted previously, the *Townend and Zoback* study of 2006 was the first to use a consolidated earthquake catalog of events derived from the Japan Meteorological Agency (JMA) catalog, the Japan University Network Earthquake Catalog (JUNEC), and the National Research Institute for Earth Science and Disaster Prevention's Kanto–Tokai Network Catalog (KTK). This improved catalog, together with the non-hierarchical clustering algorithm (similar to the recursive gridding algorithm), allowed *Townend and Zoback* [2006] to resolve more accurately the variations in S_{Hmax} orientation throughout Japan. Although the orientation of S_{Hmax} in the Kobe region is predominately east-west,

there are variations in the absolute orientation (Figure 2.10b) along the Kii Peninsula south of Kobe, an area which shows increases in seismicity following the Kobe main shock despite being in a region of CFS decrease (Figures 2.2 and 2.9c).

In order to use the stress orientations determined by *Townend and Zoback* [2001b; 2006] in our CFS modeling, we employed the stress extrapolation method of Hansen and Mount [1990] to extrapolate these S_{Hmax} orientations over the entire region of interest. This method is a two-step process that first calculates an estimate of the true stress field (from existing data), and then distance weighting to extrapolate stress
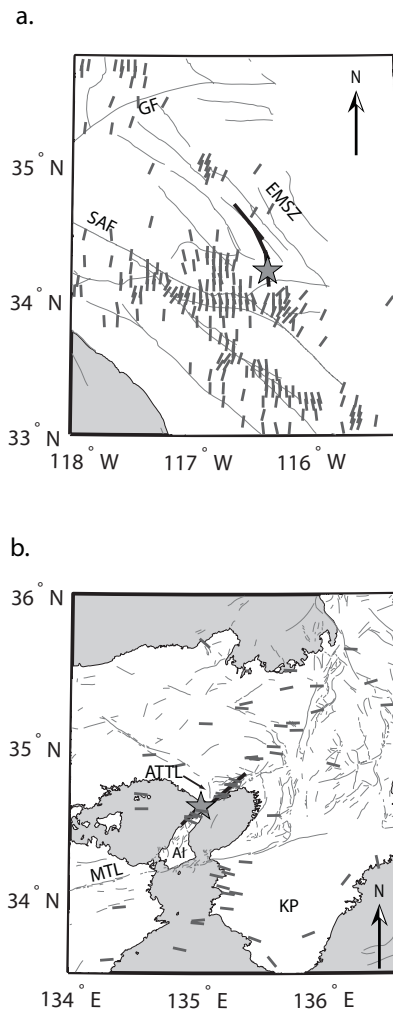
Figure 2.10: Orientations of S_{Hmax} determined by *Townend and Zoback* from focal mechanism inversions[2001b; 2006]. These orientations were extrapolated in order to calculate the change in CFS assuming heterogeneous regional stress orientations. a. In the Landers region the orientation of S_{Hmax} rotates from almost north-south in the southern to northeast-southwest in the northeast. b. In the Kobe region S_{Hmax} orientations are predominately east-west except for on the Kii Peninsula south of Kobe where there is significant rotation.

orientations to locations where stress data are unavailable. The user emphasizes either smoothness in the extrapolated field or fidelity to the data by varying how the objective function is maximized. Since we were interested in variations in the regional stress orientations and wanted the extrapolated field to correspond closely to the observed stress orientations, we required the objective function to emphasize fidelity. The resulting regional stress field, which is spatially heterogeneous, was used as input for the ΔCFS models.

Figure 2.11 presents the results of including the heterogeneous regional stress orientations in the calculations of ΔCFS caused by the Landers and Kobe earthquakes for both optimally oriented strike-slip planes and optimally oriented planes in 3D. Figures 2.3a, 2.3d, and 2.9c show that varying the stress orientation does affect the ΔCFS model, although the effect is small. When we quantitatively compared the new models of ΔCFS to the observed changes in seismicity rate, there was a slight improvement in the fit of the model to the observed seismicity rate changes (Figure 2.12). For Landers, assuming optimally oriented strike-slip planes, the percentage of grid cells that showed an increase in seismicity rate and CFS increased from 62% to 69% (Figures 2.8a and 2.12a). The percentage of grid cells with increases in both seismicity rate and CFS went from 73% to 78% when we considered optimally oriented planes in 3D (Figures 2.9b and 2.12b). For Kobe the fit of the ΔCFS to the observed seismicity rate changes did not change when we included the heterogeneous regional stress orientations (Figures 2.8c, 2.9d, 2.12c, and 2.12d). However, even with this best-fitting model for both Landers and Kobe, 7% of grid cells for Kobe and 13% for Landers show an increase in seismicity rate despite a decrease in CFS.
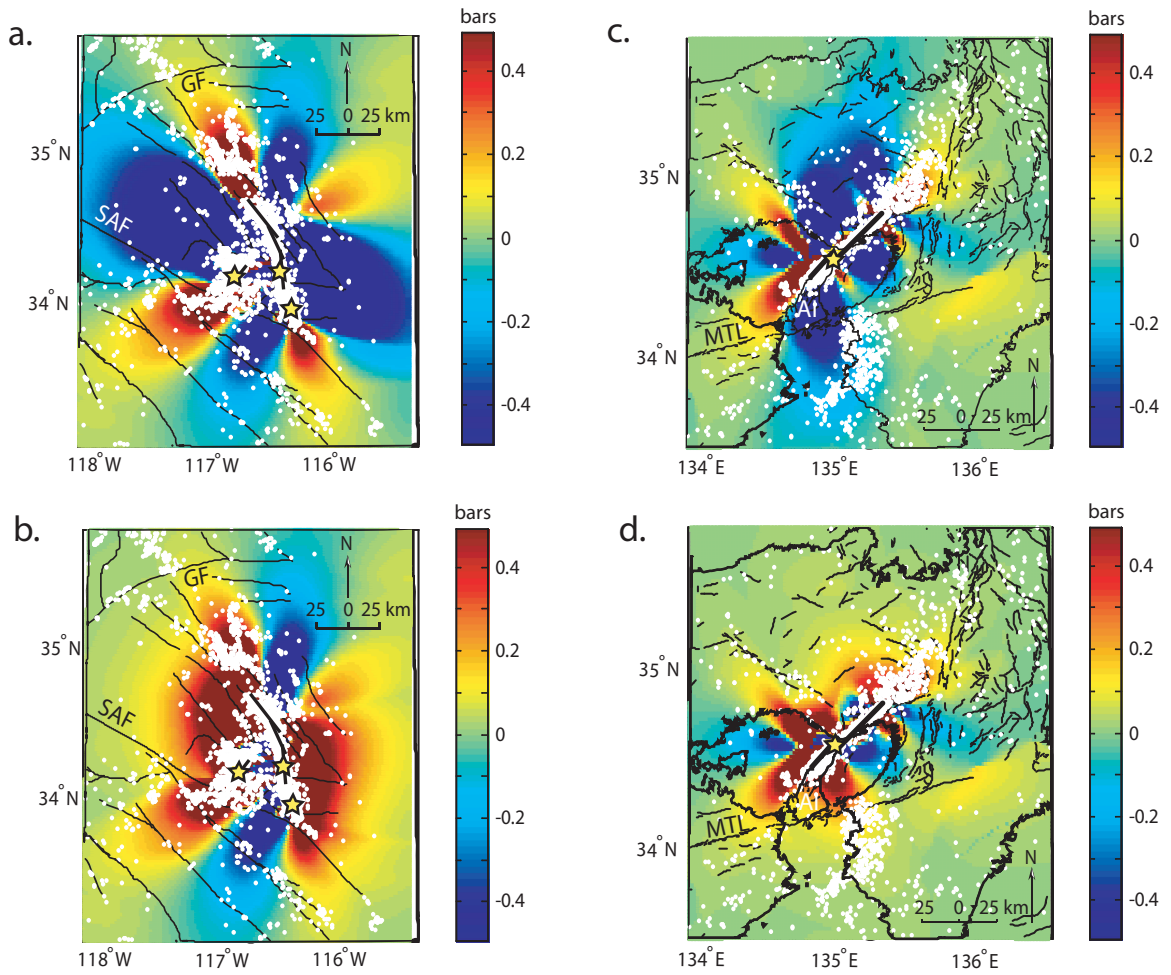
Figure 2.11: a. Elastic Coulomb stress changes from Landers earthquake using rupture model of *Wald and Heaton* [1994] on optimally oriented strike-slip planes using the heterogeneous regional stress orientations extrapolated from *Townend and Zoback* [2001b]. b. Elastic Coulomb stress changes from Landers earthquake using rupture model of Wald and Heaton [1994] on optimally oriented planes in 3D using the heterogeneous regional stress orientations. c. Elastic Coulomb stress changes from the Kobe earthquake using rupture model of *Wald* [1996] on optimally oriented strike-slip planes using the heterogeneous regional stress orientations extrapolated from Townend and Zoback [2006]. d. Elastic Coulomb stress changes from the Kobe earthquake using rupture model of *Wald* [1996; *Townend and Zoback*, 2001b] on optimally oriented planes in 3D using the heterogeneous regional stress orientations.

37
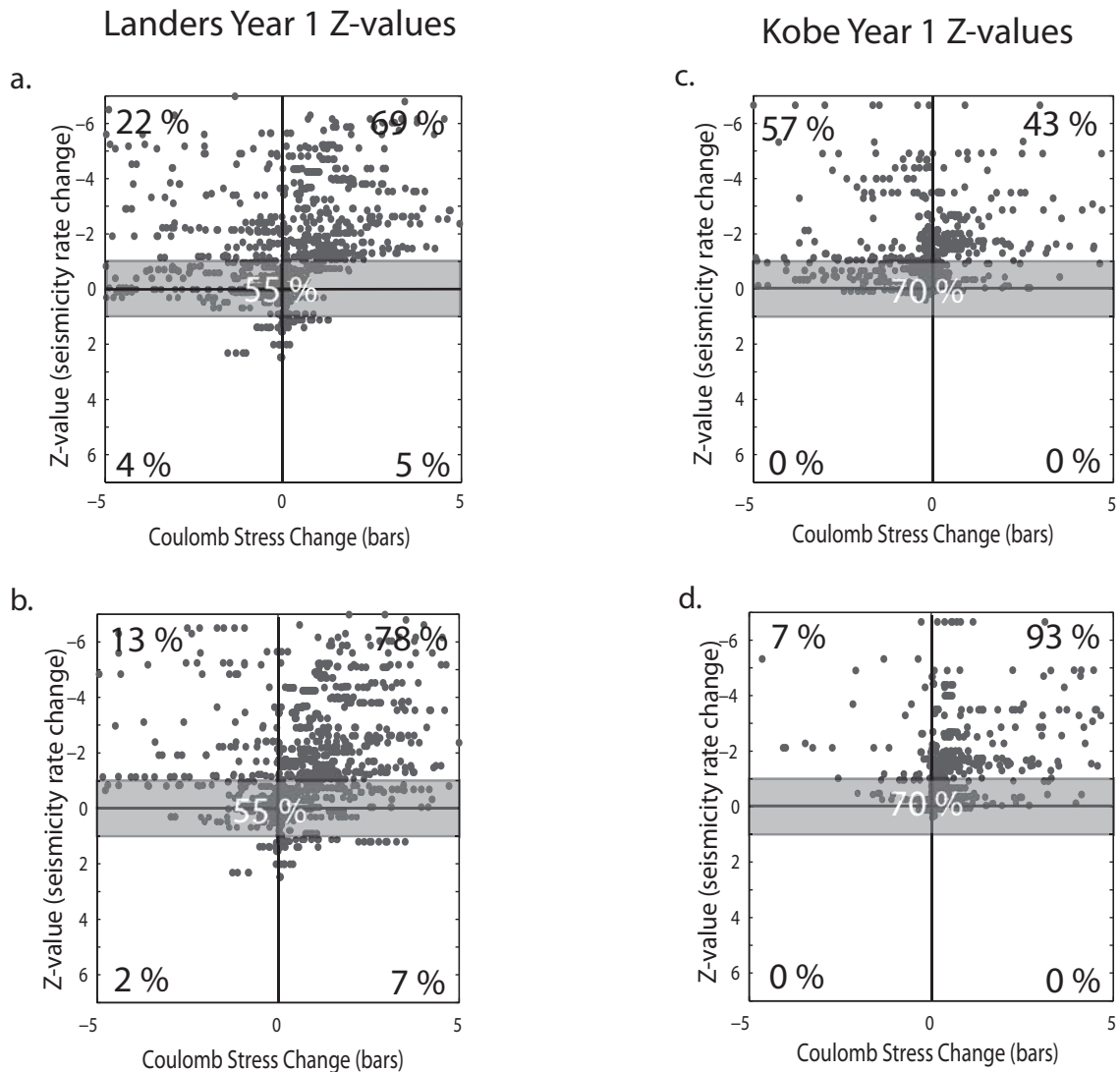
Figure 2.12: Quad-plots for the heterogeneous regional stress case for Landers and Kobe. a. Landers optimally oriented strike-slip planes. b. Landers optimally oriented planes in 3D. c. Kobe optimally oriented strike-slip planes. d. Kobe optimally oriented planes in 3D.

2.5.3 *Relationship between CFS models and apparent fit*

While the more complicated models of ΔCFS appear to fit the observed changes in seismicity rate well, the apparent fit is related to the increase in the percentage of the region that is experiencing an increase in ΔCFS (Table 2.2). To show this, we plotted the percentage of points in the upper quadrants of the quad plots versus the percentage of the region modeled to have increases (circles) and decreases (squares) in ΔCFS. We did

this for each of the four ΔCFS models where there was a significant rate change (Figure 2.13). The linear trend of the points with an approximate slope of one indicates that for both Landers and Kobe, the apparent improvements in the fit of the ΔCFS models to the observed changes in seismicity rate change is simply the result of increasing the proportion of the region modeled to have a positive ΔCFS. The percentage of points in each quadrant of the quad-plot essentially only tells what percentage of the region is experiencing positive or negative ΔCFS. As primarily seismicity rate increases are observed, despite the sign of ΔCFS, the percentage of points in a given quadrant of the quad-plots is simply illustrating the percentage of the region experiencing a positive or negative ΔCFS for each of the various models.

Landers

Model	ISR with ΔCFS > 0	DSR with ΔCFS < 0	Area with ΔCFS > 0	Area with ΔCFS < 0
Strike-slip, regional stress	62	29	64.99	35.01
3d, regional stress	73	18	78.12	21.88
strike-slip, heterogenous stress	69	22	73	27
3d, heterogenous stress	78	13	82.88	17.12

Kobe

Model	ISR with ΔCFS > 0	DSR with ΔCFS < 0	Area with ΔCFS > 0	Area with ΔCFS < 0
Strike-slip, regional stress	43	57	43.39	56.61
3d, regional stress	93	7	93.8	6.2
strike-slip, heterogenous stress	43	57	42.05	57.95
3d, heterogenous stress	93	7	93.98	6.02

Table 2.2: Table comparing the percentage of cells that experience and increase in seismicity rate for increases and decreases in ΔCFS and the percentage of the region experiencing ΔCFS increases and decreases. These results are also shown graphically in Figure 13. ΔCFS >0 indicates areas with an increased tendency to slip, while ΔCFS<0 are less likely to slip. ISR: increased seismicity rate, DSR: decreased seismicity rate.
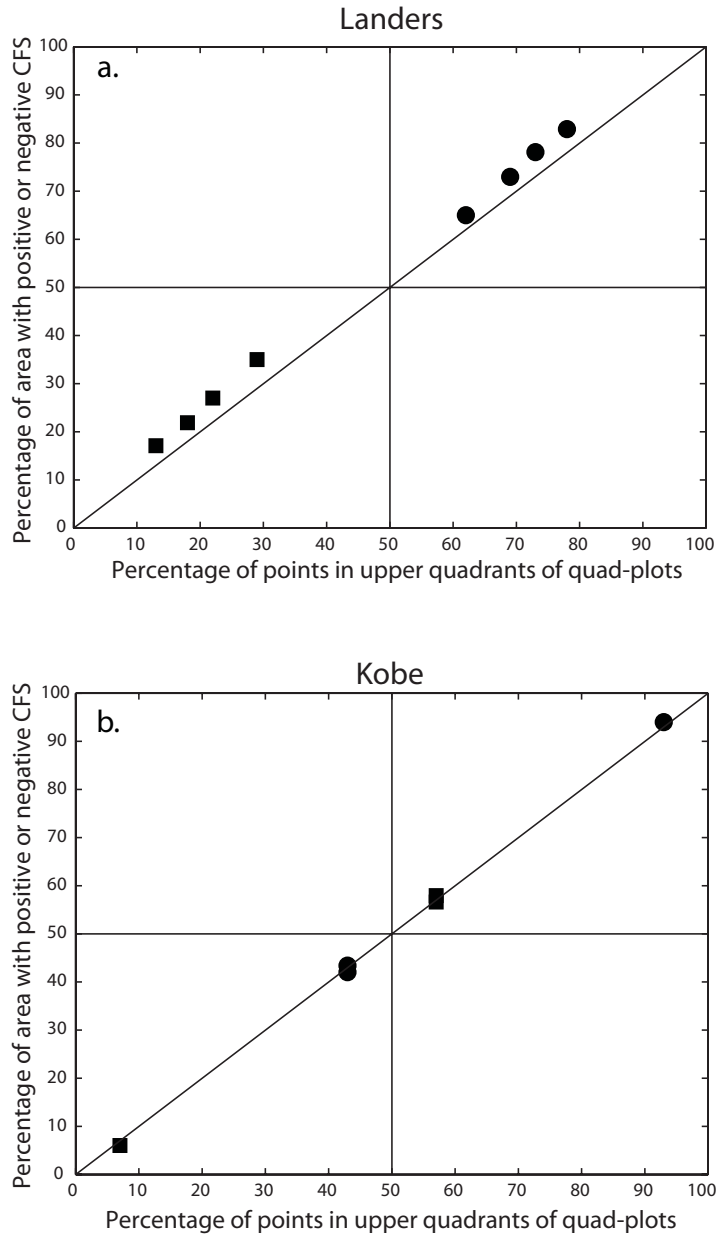
Figure 2.13: Comparison of the percentage of points in the upper quadrants of the quad-plot (seismicity rate increase) versus the percentage of the region experiencing an increase or decrease in CFS for a. Landers and b. Kobe. Circles represent regions experiencing an increase in CFS, while the squares represent the regions experiencing a decrease in CFS. The linear relationship indicates that the percentage of points that "fit" the elastic Coulomb stress model of an increase in seismicity associated with an increase in CFS are simply reflecting the proportion of the region modeled to experience an increase in CFS.

2.5.4 *Seismicity rate evolution*

Using the heterogeneous regional stress and optimally oriented planes in 3D (the "best-fitting" model) for both Landers and Kobe, we then examined the number of events for one year before (gray bars) and one year after (black bars) the main shock in grid cells with increases and decreases in CFS after filtering out near field values. Figures 2.14a and 2.14b show that while only seismicity increases are observed, seismicity rates are higher after the main shock in areas of ΔCFS increase. This observation holds for all of the ΔCFS models and time intervals tested, and the implications will be discussed in the next section.
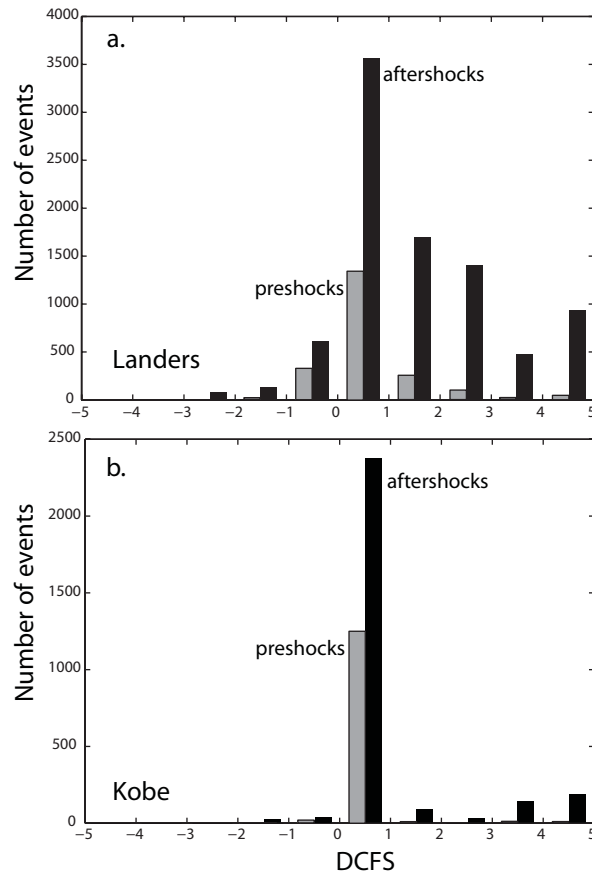
Figure 2.14: a. Number of events in grid cells with a given value of ΔCFS for the year before and after the Landers main shock. Light gray bars are the year before and dark gray bars are the year after the main shock. The number of events is greater in the year after the main shock compared to the year before regardless of the value of ΔCFS but the increase in events is larger in grid cells with a positive ΔCFS. b. Number of events in grid cells with a given value of ΔCFS for the year before and after the Kobe main shock. Light gray bars are the year before and dark gray bars are the year after the main shock. The number of events is greater in the year after the main shock compared to the year before regardless of the value of ΔCFS but the increase in events is larger in grid cells with a positive ΔCFS.

2.6 Discussion

The detailed quantitative comparisons of changes in CFS and changes in seismicity rate as a result of the Landers and Kobe earthquakes indicate that decreases in seismicity rate are difficult to observe. Rather, all we can measure are increases in seismicity rate everywhere, regardless of the sign or magnitude of ΔCFS. Even areas with high background seismicity rates, where decreases might be observable, have still higher seismicity rates following the main shock. This agrees with observations made by *Toda et al.* [2005] following the Landers and Hector Mine earthquakes. They argue that an increase in seismicity rate in areas of ongoing seismicity is consistent with predictions based on rate-and-state friction. However, the converse was almost never observed in their study.

Our ability to primarily resolve seismicity rate increases agrees with the observations by *Kilb et al.* [2002]. They conclude that while the pattern of seismicity rate increases agrees with both the static ΔCFS and dynamic ΔCFS(t) models, the observed asymmetry of the triggered seismicity fits the dynamic model better. *Kilb et al.* [2002] argue that this implies that dynamic stresses can be as effective as static stresses in triggering seismicity even long after the seismic waves have passed. For all the tested models we observe that seismicity rate increases regardless of the value of ΔCFS, but increases more in areas of positive ΔCFS (e.g., Figure 2.14). These observations suggest that both dynamic stress changes, which would increase seismicity everywhere, and static stress changes, which should have stress shadows, may be triggering seismicity after the Landers and Kobe events. This may explain why the increase in seismicity in areas of positive ΔCFS is larger than the increase in areas of negative ΔCFS. In regions of positive ΔCFS the seismicity rate would be responding to both the increases in static Coulomb stress offset and dynamic stresses from the passing of the seismic waves, while in regions of negative ΔCFS the increases in seismicity should only be due to the dynamic stresses, and some of this may be offset by the decreases in static ΔCFS.

This observation of seismicity rates increasing regardless of the value of ΔCFS is contrary to what has been argued by numerous other researchers [*Reasenberg and*

Simpson, 1992; *King, et al.*, 1994; *Harris and Simpson*, 1996; *Reasenberg and Simpson*, 1997; *Harris and Simpson*, 1998; *Toda, et al.*, 1998; *Wyss and Wiemer*, 2000; *Toda and Stein*, 2003; *Woessner, et al.*, 2004; *Ma, et al.*, 2005]. We explore possible reasons for the contradictions between some of these studies and our results here. When we use the same gridding technique and time periods as *Wyss and Wiemer* [2000] for Landers, while the quad-plots indicate decreases in seismicity rate are able to be resolved, there remain a significant number of nodes that experience an increase in seismicity rate despite a decrease in ΔCFS. The reason that decreases in seismicity rate are able to be resolved with the nearest neighbor technique is because in areas of low seismicity the sampling circle around the node must be sufficiently large to sample enough earthquakes that many of these events are responding to different ΔCFS than that observed at the node, or are sampling many widespread areas that are experiencing changes in rate that are not significant. While this does indicate that seismicity rate decreases are resolvable when the sampling area sufficiently large, it does not allow for determining if the observed rate changes correlate with changes in elastic ΔCFS as the large sample area covers areas of different values of ΔCFS. The techniques used by *Toda et al.* [1998] to quantitatively compare seismicity rate changes and ΔCFS following Kobe presents the comparison in such a way as to emphasize the positive correlation between the increases in both seismicity rate and positive ΔCFS while de-emphasizing the regions of negative ΔCFS and decreases in seismicity rate. Finally, many of the studies done for other earthquakes were either calculating the change in stress directly on known structures [*Reasenberg and Simpson*, 1992; 1997], looking at earthquake couplets [*Toda and Stein*, 2003; *Woessner, et al.*, 2004], looking at very large earthquakes like the 1906 San Francisco and 1857 Fort Tejon earthquakes with ruptures of hundreds of kilometers [*Harris and Simpson*, 1996; 1998], or examining thrust main shocks which change the Coulomb stress in the crust very differently than large strike slip events [*Ma, et al.*, 2005].

The remaining major question related to the inability to resolve seismicity rate decreases following Landers and Kobe is whether the gridding technique or the time intervals used permit the resolution of seismicity rate decreases. *Marsan* [2003] and *Marsan and Nalbant* [2005] note that parameters used to estimate seismicity rate changes

are biased towards positive rate changes, particularly on short time scales. They determine that there should be at least 100 days of data to resolve decreases in seismicity rate. The short time period explains why we are unable to resolve seismicity rate decreases in the first month following the Landers and Kobe main shocks, but not why using a year or more of data we are still unable to resolve rate decreases. *Ma et al.* [2005] observed that shadows following the ChiChi earthquake didn't appear until three months after the main shock. We also tested this time interval, instead of simply one month following the main shock, but saw no difference in the changes in the correlation between seismicity rate and ΔCFS. To test if shadows are even detectable for the grid and time intervals we created synthetic seismicity catalogs by running Monte-Carlo simulations while decreasing or increasing the background seismicity rate in each grid cell by 10%, 50% and 90% and calculating the z- and β-values. We find using the uniform grid that the resolution of detecting increases and decreases in seismicity rate are approximately equal, though it is difficult to resolve either at both the 1σ and 2σ levels. The only way that we are able to resolve any significant rate decreases with real data is using the nearest neighbor technique, whose limitations we have already addressed. If it were simply necessary to sample a larger area in regions of low seismicity to resolve rate decreases, the recursive gridding algorithm should have resolved the rate decreases seen with the nearest neighbor technique. That there were no seismicity rate decreases resolved using the recursive gridding algorithm implies that it is not simply the optimal grid that is preventing the resolution of rate decreases.

2.7 Conclusions

Triggering of earthquakes by changes in elastic Coulomb stresses predicts that seismicity rates should increase in areas of positive ΔCFS and decrease in areas of negative ΔCFS. To test this prediction, we quantitatively compared various models of ΔCFS from the Landers and Kobe earthquakes to long-term changes in seismicity rates following both events. While all the ΔCFS models appear to show positive ΔCFS with increased seismicity rate changes in >50% of the area for which rate changes could be measured, this is only because we measured rate increases almost everywhere and most

of the region experiences an increase in CFS. Since we are unable to measure a statistically significant decrease in seismicity rate, we are unable to verify or reject elastic Coulomb stress transfer as a triggering mechanism over other mechanisms, such as dynamic triggering. Also, as the complexity of the static ΔCFS models increased they appeared to better predict the locations of the observed increases in seismicity rate, but we found that this increase in correlation was simply reflecting the percentage of the region subject to positive values of ΔCFS.

Examination of the number of events in the year before and after the main shock relative to the sign of ΔCFS showed that only seismicity increases were measured following the main shock, and more so in areas of increased CFS. Areas of increased CFS have higher seismicity rates than areas of decreased CFS both before and after the main shock. The observation that seismicity rate is highest after the main shock where it was high before the main shock leads us to conclude that earthquake triggering, whether by static or dynamic stresses, is concentrated in critically stressed regions of the crust that were failing before the main shock, which explains why very small changes in stress are all that are needed to trigger additional seismicity. However, that we were unable to resolve decreases in seismicity rates even in areas of negative ΔCFS indicates that dynamic stresses remain a possible mechanism for triggering earthquakes. We thus conclude that everywhere seismicity rates could be resolved, rate increases following the Landers and Kobe earthquakes and did not reflect changes in elastic Coulomb stress.
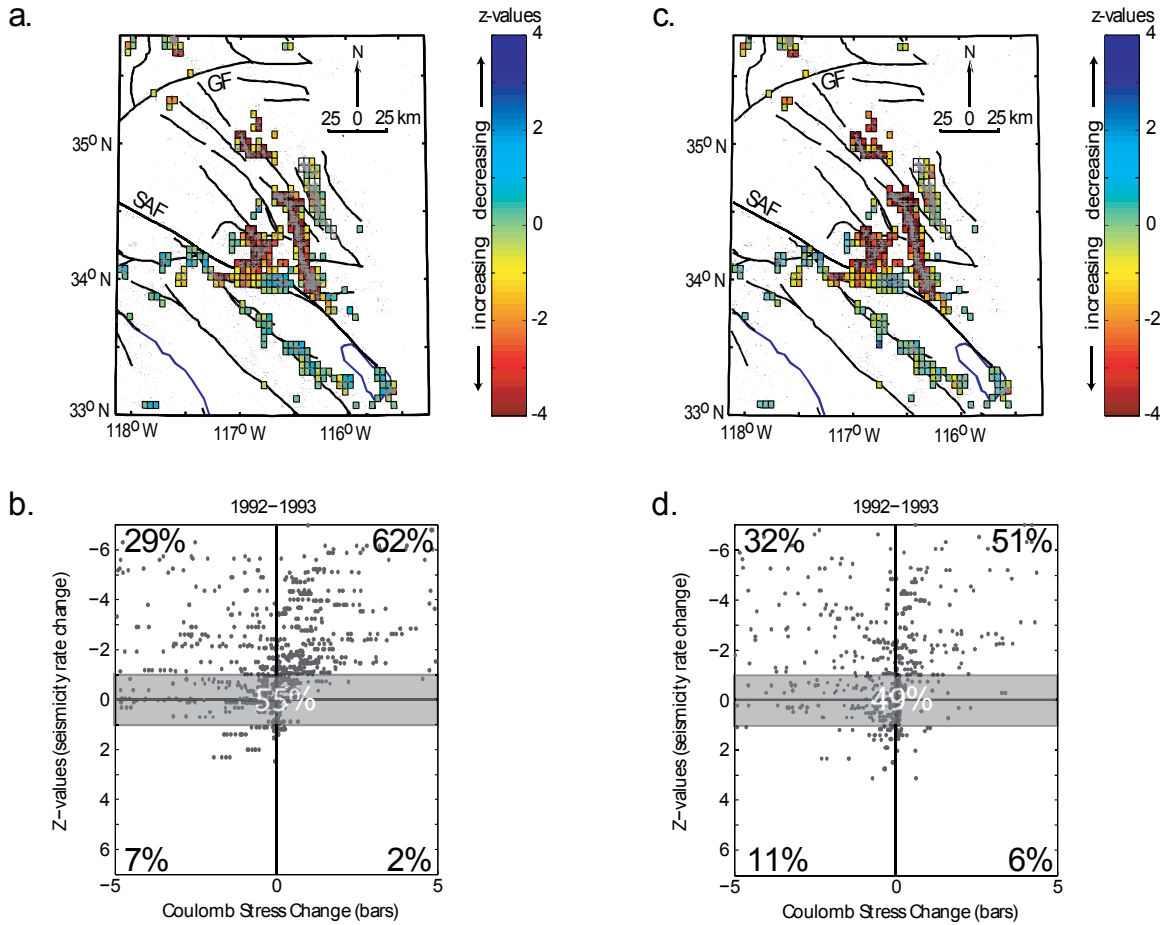
Supplemental Figure: When there are no events in either the before or after time period the denominator of the z-value becomes singular. In order to include the important instances when there are no events in the before or after time period there needs to be a substitution for the singular value, the obvious choices being 0 or 1. Here we test how the choice of 0 or 1 effects the rate changes and resulting quad-plots. We compared the rate changes using 1 (a and b) and 0 (c and d) to the simplest ΔCFS model assuming optimally oriented strike-slip planes and a uniform regional stress orientation. a. Seismicity rate change following the Landers earthquake using the z-value changing singular values to 1. Grid cells defined using seismicity from 1984-2000. Background rate determined by 1984-1992 compared to 1992.6-1993.6. b. The quad-plot comparing changes in Coulomb failure stress to the seismicity rate changes in a. c. Seismicity rate change following the Landers earthquake using the z-value changing singular values to 0. Grid and rate calculated the same as in a. d. The quad-plot comparing the changes in Coulomb failure stress to the seismicity rate changes in c. There are no significant changes between the rate changes calculated using 0 or 1 to replace the singular values in the rate change calculation. We use 1 for the singular values for the remainder of the paper.

Chapter 3

A Global Search for Stress Shadows[2]

Abstract

There continues to be debate regarding the relative proportion of earthquakes triggered by passing seismic waves versus static crustal stress changes from a main shock. Static stress changes are expected to have long term effects on earthquake probabilities and thus have implications for hazard assessments, whereas, dynamic stress changes due to the passing of seismic waves are not thought to have an effect on long term earthquake probabilities. Both mechanisms are expected to raise seismicity rates in some areas, but only static stress change calculations predict that some crustal volumes near a main shock will undergo systematic earthquake rate reductions, or stress shadows. Thus identification of post-main-shock earthquake suppression is diagnostic of a static stress-change process. However, since pre-main-shock earthquake rates are often low to begin with, post-main-shock rate reductions are difficult to identify. We note that, in principle, static-stress change theory predicts suppression of particular earthquake mechanisms in a shadow zone rather than an overall rate reduction. A stress shadow can therefore be characterized by a change in the average focal mechanism of seismicity before and after the main shock that results from suppression of a given mechanism type.

We examined a global catalog of 119 $M_s \geq 7$ main shock earthquakes and associated events drawn from the Harvard CMT catalog. We first examined the average mechanism before and after the main shock, and then compared this with the changes in rate of each of the mechanisms. Of 119 main shocks, only 2 showed significant average-mechanism changes caused by earthquake suppression, which are difficult to explain with a dynamic stress change hypothesis. However, by stacking the data we were able to resolve statistically significant suppression of particular post-main-shock focal mechanisms. This indicates that, while static stress signals and stress shadows are subtle, they are indeed present in the global catalog.

3.1 Introduction

Earthquakes modify stress in the crust surrounding a main shock rupture and are expected to change the seismicity rate accordingly which has implications for future earthquake probabilities and hazard modeling [Working Group on California Earthquake Probabilities, 2003]. Dynamic stresses induced by the passage of seismic waves [*Cotton and Coutant*, 1997; *Belardinelli, et al.*, 1999; *Kilb, et al.*, 2000; *Gomberg, et al.*, 2003], or static stresses induced by fault offset [*Yamashina*, 1978; *Das and Scholz*, 1981; *Stein and Lisowski*, 1983; *King, et al.*, 1994] are both suggested sources of near-field earthquake triggering. A key difference between the two triggering processes is that static stress changes caused by M>7 earthquakes are expected to reduce stress, and hence suppress seismicity, in a relatively large volume of the surrounding crust [*Harris and Simpson*, 1998; *Parsons*, 2002]. This phenomenon of stress-induced seismicity rate decrease, such as the one observed following the 1857 Fort Tejon and 1906 San Francisco earthquakes in California [*Harris and Simpson*, 1996; *Stein*, 1999] is commonly known as a *stress shadow*. While this decrease in seismicity following large main shocks is predicted by static stress change models, some researchers have failed to show correlations between modeled stress decreases and observed seismicity rate changes [*Felzer and Brodsky*, 2005; *Mallman and Zoback*, 2007a]. A possible explanation for the lack of resolvable decreases in seismicity rate following M>7 earthquakes is that earthquakes triggering is

dominated by the dynamic process as opposed to static stress changes [*Felzer, et al.*, 2004; *Felzer and Brodsky*, 2005].   While mechanisms have been proposed for dynamic stress changes to suppress some earthquakes [*Richardson and Marone*, 1999; *Parsons*, 2005], only changes in static stresses predict broad, systematic increases and decreases in seismicity rate. We propose that a lack of observable seismicity rate decreases can be explained using static stress triggering if there is systematic suppression of particular focal mechanisms after a main shock. Using this hypothesis we performed a global search for stress shadows following $M_s \geq 7$ main shocks.

3.1.1 *Stress shadow definition*

Stress shadows have traditionally been defined as a seismicity-rate decrease that corresponds to the static stress decrease following an individual main shock. A clear stress shadow followed the 1906 San Francisco earthquake [*Harris and Simpson*, 1998]. While earthquakes were triggered near the ends of the 1906 rupture [*Meltzner and Wald*, 2003], seismicity rates appear to have been reduced adjacent to the rupture; in the San Francisco Bay area, there were numerous *M*>6 events during the 75-year period before 1906, while in the 75 years following 1906 there was only one *M*>6 event [*Stein*, 1999]. If the change in Coulomb failure stress (CFS) is resolved on N34°W striking right-lateral planes (similar orientation to the San Andreas Fault (SAF)) most of the region is predicted to experience a decrease in CFS, thus predicting a seismicity rate decrease similar to the observations (Figure 3.1a). However, not all of the active faults in the San Francisco Bay area fail in a right-lateral sense like the SAF; there are also numerous thrust faults, such as the fault that failed in the 1989 Loma Prieta earthquake [*Reasenberg and Simpson*, 1992]. If the change in CFS is resolved on thrust faults striking N34°W (the dominant orientation of the thrust faults in the coast range) there is an increase in the CFS (Figure 3.1b). This would predict an increase in seismicity instead of a shadow, which is predicted by the decrease in CFS seen in Figure 3.1a. Similar patterns are observed when resolving the change in CFS on faults of different orientations following a thrust main shock as is shown in *Lin and Stein* [2004]. In addition to different faulting mechanisms (the sense of slip on the faults) responding differently to the same main

shock there is the added complication of the difficulty in resolving seismicity rate decreases. Since seismicity is typically low before a main shock in any given year, and it is impossible to have a negative seismicity rate, stress shadows in the traditional sense are fundamentally hard to identify.

Due to the difficulty in resolving traditional stress shadows and the differences in the static stress change for different faulting styles, we develop an extended definition of a stress shadow. We suggest that a static stress process is uniquely identified by a post-main shock change in average focal mechanism caused by a decrease in the seismicity rate for a given faulting regime. For example, following the 1906 San Francisco strike-slip earthquake shown in Figure 3.1 we would expect to see a decrease in the number of strike-slip events, but an increase in thrust events, thus satisfying the requirements of our definition.
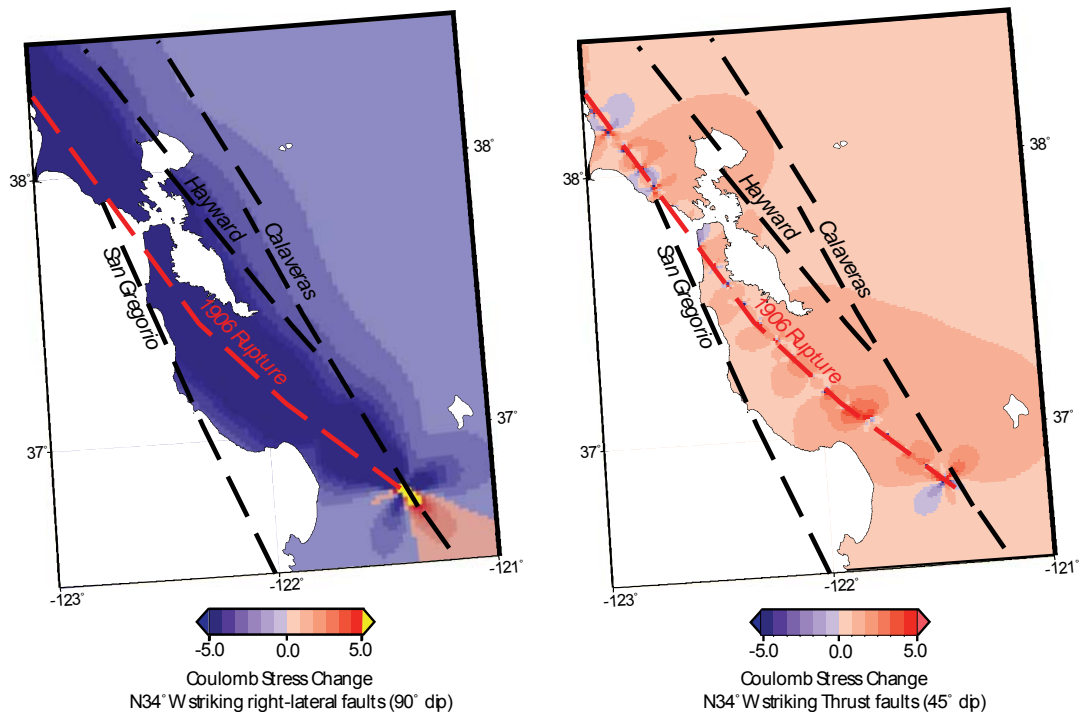
Figure 3.1: Changes in the Coulomb stress following the 1906 San Francisco earthquake resolved on N34°W striking right-lateral planes (left), and N34°W striking dip-slip planes (right). Cool colors indicate a decrease in the Coulomb stress on the planes, implying a decrease in the seismic potential, while the warm colors indicate an increase in the Coulomb stress and an increase in the seismic potential. The figure on the left is the traditional view of the stress shadow following the 1906 earthquake, but by calculating the change in stress on planes of a similar orientation to the Loma Prieta earthquake of 1989 it becomes apparent that the 1906 earthquake would have encouraged events of this mechanism.

3.1.2 *Motiviation*

Using this new definition for a stress shadow we examine a catalog of $M_s \geq 7$ events to see if stress shadows are present on a global scale. Working on a global scale allows for the identification of general trends instead of focusing on individual events as has been primarily done in the past [*Simpson and Reasenberg*, 1994; *Toda, et al.*, 1998; *Stein*, 1999; *Wyss and Wiemer*, 2000; *Freed and Lin*, 2001; *Gomberg, et al.*, 2001; *Felzer, et al.*, 2002; *Masterlark and Wang*, 2002; *Pollitz and Sacks*, 2002; *Lin and Stein*, 2004; *Woessner, et al.*, 2004; *Ma, et al.*, 2005; *Marsan and Nalbant*, 2005; *Mallman and Zoback*, 2007a]. To search for stress shadows globally we will use the Harvard CMT catalog between January 1977 and September 2000 to examine the average focal mechanisms and rate changes for each faulting regime following $M_s \geq 7$ main shocks.

3.2 Data

The use of a global catalog allows us to identify processes that are active globally instead of generalizing from individual earthquakes and the large data sample implies better statistics. We stack the data to enhance small signals which allow us to detect rate and mechanism variations that would not be apparent or statistically significant for an individual event. We use the Harvard CMT global catalog between January 1977 and September 2000 for this study for which solutions are regularly produced for events with $M_s \geq 5.5$ [*Dziewonski, et al.*, 1981]. Over the time period used in this study there were 17,402 events globally that have CMT solutions.

We use the same selection criteria and thus the same subset of the CMT catalog as *Parsons* [2002] used for his global Omori-law study. We first select all $M_s \geq 7$ earthquakes as potential triggering, or stress shadow inducing events; the choice of $M_s \geq 7$ was made in advance and not changed in the course of this study. We then remove any $M > 7$ events within 1-spatial degree of this set as potentially triggered, even if it was larger than its predecessor. This selection process resulted in 119 events identified as main shocks (Figure 3.2a). Of these 119 events 67 fall in the time window of 1985-1995 which allows an 8 year time window before and 5 year window after each main shock. These time windows before and after each main shock are necessary for the
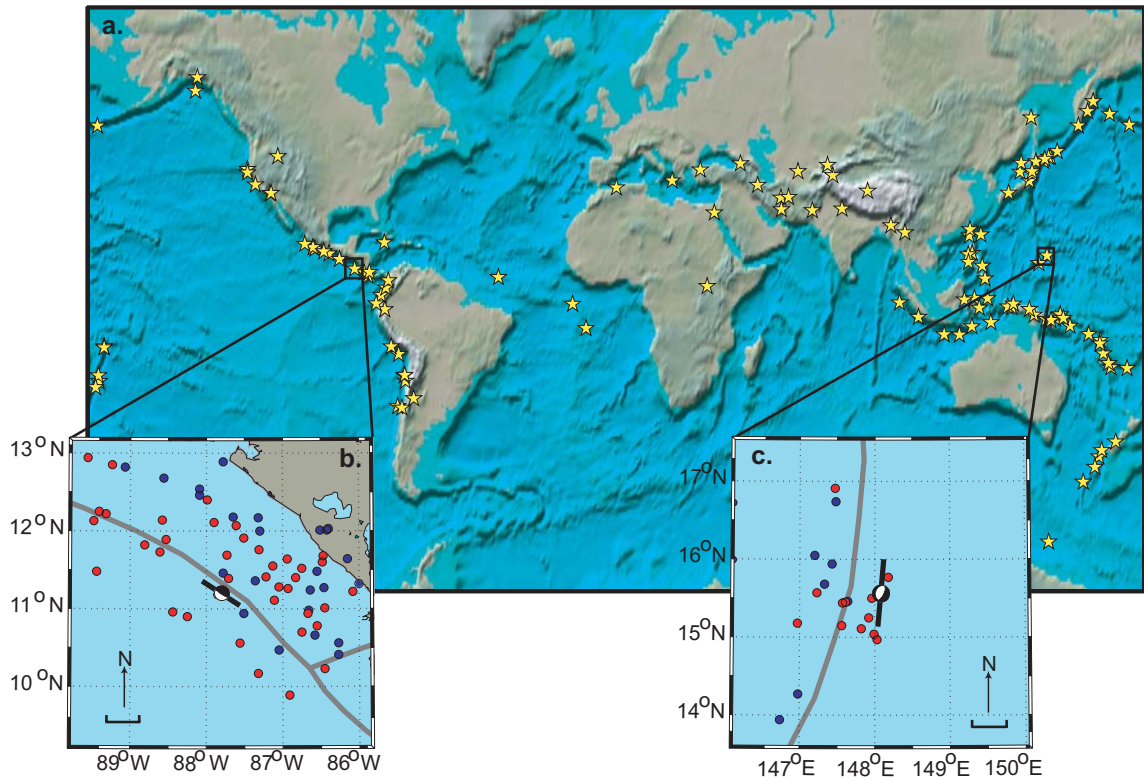
Figure 3.2: Earthquakes used in this study. a. The stars indicate the 119 $M_s \geq 7$ main shocks used in this study. b. and c. show the mechanism, approximate rupture length (black line) and spatial distribution of events within $\pm 2°$ before (blue) and after (red) the main shock for the two events whose statistics are shown in figures 3.4 and 3.5. b. is the Near Coast of Nicaragua event in Figure 3.5 and c. is the Mariana Islands Region event in Figure 3.4.

determination of rate changes and for some of the statistical tests described later. These 67 events are classified as main shocks for the remainder of this study. For each of the identified main shocks all the earthquakes in the CMT catalog within $\pm 2°$ of that particular main shock are selected. By selecting events in a $\pm 2°$ box we are likely selecting events outside the zone affected by changes in static stress changes, at least for some of the main shocks. However, performing the identical analyses selecting only events in a ± 100km ($\sim 1°$) box (an area more likely affected by changes in static stress) produced the same results as the larger area, so we will continue using the larger area to increase the number of events for more robust statistics. For the subsequent analysis we focus on the 5 years before and after the main shock as this is the time period before the seismicity rate has returned to the background rate (see Figure 9 of *Parsons* [2002]). As illustrated in Figure 3.2a, the identified main shocks are dominated by circum-Pacific

subduction zone events and the overall mechanism diversity in the catalog mimics the mechanism diversity observed globally. Figures 3.2b and 3.2c show the events in the 5 years before (dark blue) and after (red) for two of the identified main shocks. We will look at these two events in more detail later in the paper.

3.3 Methods

One complication with static stress change calculations, especially when dealing with a global catalog, is the requirement of choosing the nodal plane that slipped for each event. In order to avoid this complication we use a graphical method developed by *Frohlich* [1992; 2001] which uses the plunge of the P-, T-, and B-axes (principal stress axes) from the focal mechanism solution to quantitatively display the focal mechanisms on a ternary plot. Using this method to visualize the orientation of the focal mechanism solutions for all of the earthquakes within ± 2° of the identified main shocks avoids the complication of having to choose nodal planes for each of the events and allows quantitative observations of small changes in the average focal mechanism before and after the main shock. Each of the vertices on the ternary plot represents one of the "pure" mechanisms depending on which axis is vertical; thrust when the T-axis is vertical, strike-slip when the B-axis is vertical, and normal when the P-axis is vertical (Figure 3). Following *Frohlich* [1992] we classify focal mechanisms as thrust when the plunge of the P-axis is greater than 50°, and normal or strike-slip when the plunge of the T- or B-axis is greater than 60°.

For each identified main shock, the main shock and events within the ± 2° box are plotted on a ternary diagram (Figure 3.3a). The main shock is plotted as a star, the events before the main shock as blue circles, and the events after the main shock as red circles. This allows general observations on the orientation and distribution of focal mechanisms before and after the main shock. To identify changes in the average focal mechanisms we calculate the average mechanism before and after the main shock (Figure 3.3b). The change in average mechanism is quantified by calculating the Euclidean distance between the two average focal mechanisms.

We use a bootstrap analysis to determine the significance of the change in average focal mechanisms following a main shock. Using the 8 years of catalog data before the M>7 triggering event, we select random 5-year windows and perform the analysis described above to calculate the mean and standard deviation of the average focal mechanism change when there is no triggering event. Following the bootstrap iterations, we have a distribution of the variation in average focal mechanisms without a M>7 triggering event. We use this to determine if the change in average post-shock focal mechanism is significant compared to the variation in mechanism present before the triggering event.
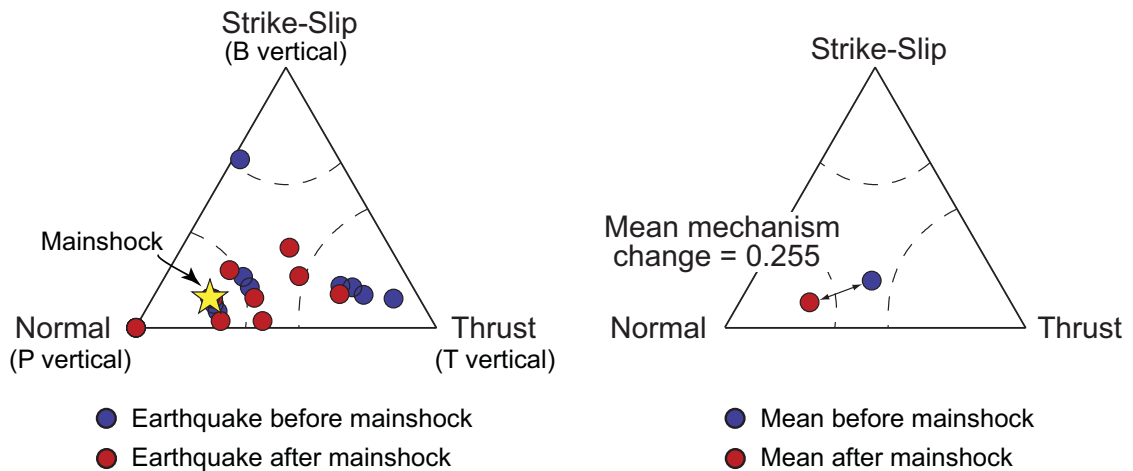
Figure 3.3: Example of how events are plotted on the ternary plots. The location of the earthquake's mechanism on the ternary plot is determined by the plunge of the P, T and B-axis. A pure strike-slip event will have a B-axis that is vertical (plunge of 90°) and will plot at the top vertex of the triangle. The main shock is represented by a yellow star. Events before the main shock are shown as blue dots, while events after the main shock are red dots. For all of the events before and after the main shock we calculate an average mechanism, which are shown as the blue and red dots in the right hand figure. The mean mechanism change is simply the Euclidean distance between these two mean mechanisms.

3.4 Individual main shocks

Using the method detailed above we analyzed the 67 M>7 events in our catalog. This analysis found 13 events with a change in mechanism that is significant at the 1σ level compared to the pre-shock variation. We use the lower requirement of 1σ to increase the number of events causing a significant change in average mechanism which we will further analyze.

Under our definition of a stress shadow, while the over all seismicity rate may increase, we would expect to see a decrease in the rate of at least one mechanism after the main shock to account for the mean change. We thus, look in detail at the evolution of seismicity for each of the mechanisms before and after the main shock for the 13 events that show a significant change in the average mechanism following the main shock. For the 13 events that show a significant change in average mechanism we then examine the number of events per year for each mechanism and the annual rate of events for each mechanism during the 5 years before and after the main shock. However, only 2 of the 13 events show a decrease in rate of at least one mechanism which current understanding of dynamic triggering can not explain.
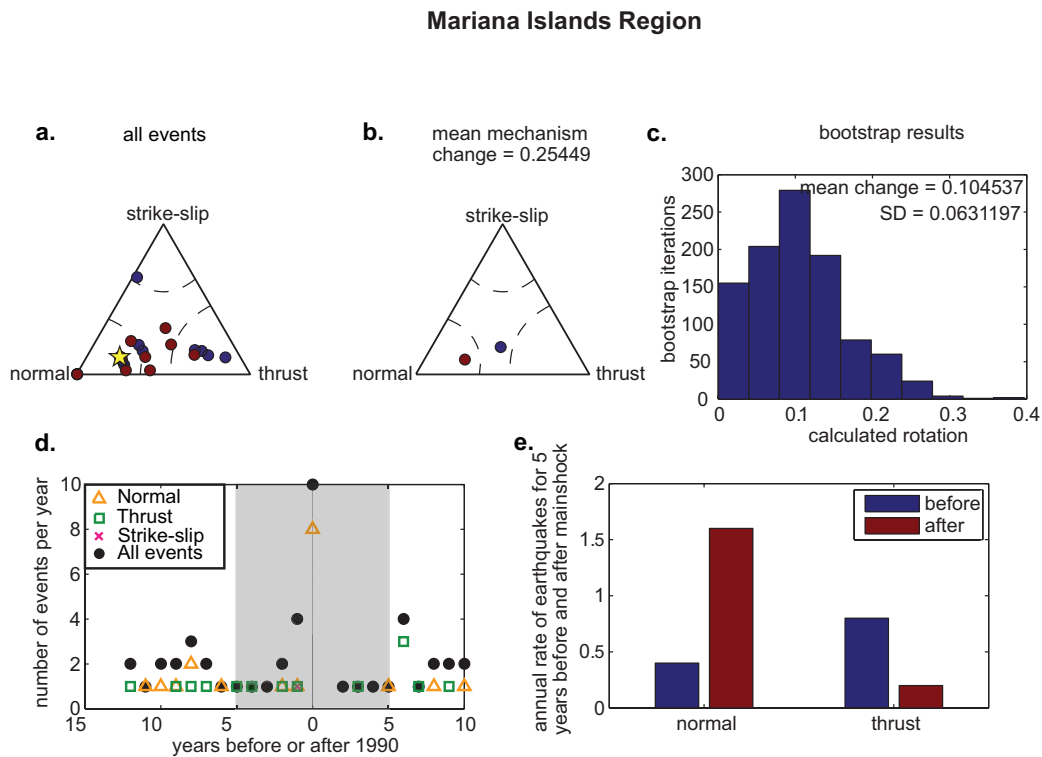
Figure 3.4: Statistics for the Mariana Islands Region main shock. a. ternary plot of the main shock (yellow star), events before (blue dots), and after (red dots) the main shock. b. The mean mechanism before (blue) and after (red) the main shock and the mean mechanism change. c. Bootstrap results of the variability of focal mechanism orientation before the main shock with the mean change and standard deviation to test the significance of the observed mechanism change. d. plot of the number of events per year for all mechanisms showing the initial spike in seismicity at the time of the main shock. The grey box indicates the 5 years before and after the main shock which are used to determine the annual rate of earthquakes. e. The annual rate of earthquakes for the 5 years before and after the main shock. There is a decrease in the number of thrust events, thus, while there is an overall increase in the number of events after the main shock relative to before, there is a change in the mean mechanism and a decrease of at least one mechanism indicating a stress shadow.

Figure 3.4 shows one of the 2 events that have a significant change in the mean mechanism and a decrease in seismicity rate for at least one mechanism; in this case there is a decrease in the number of thrust events. Figure 3.5 shows an example of an earthquake that caused a significant change in the mean focal mechanism that we do not interpret as a stress shadow. In this example there were rate increases for all mechanisms, but some mechanisms were disproportionately increased such that the mean mechanism changed. Since both the static and dynamic stress triggering models explain rate increases, this type of mean mechanism change cannot be unambiguously attributed to either the static or dynamic model.

Near Coast of Nicaragua
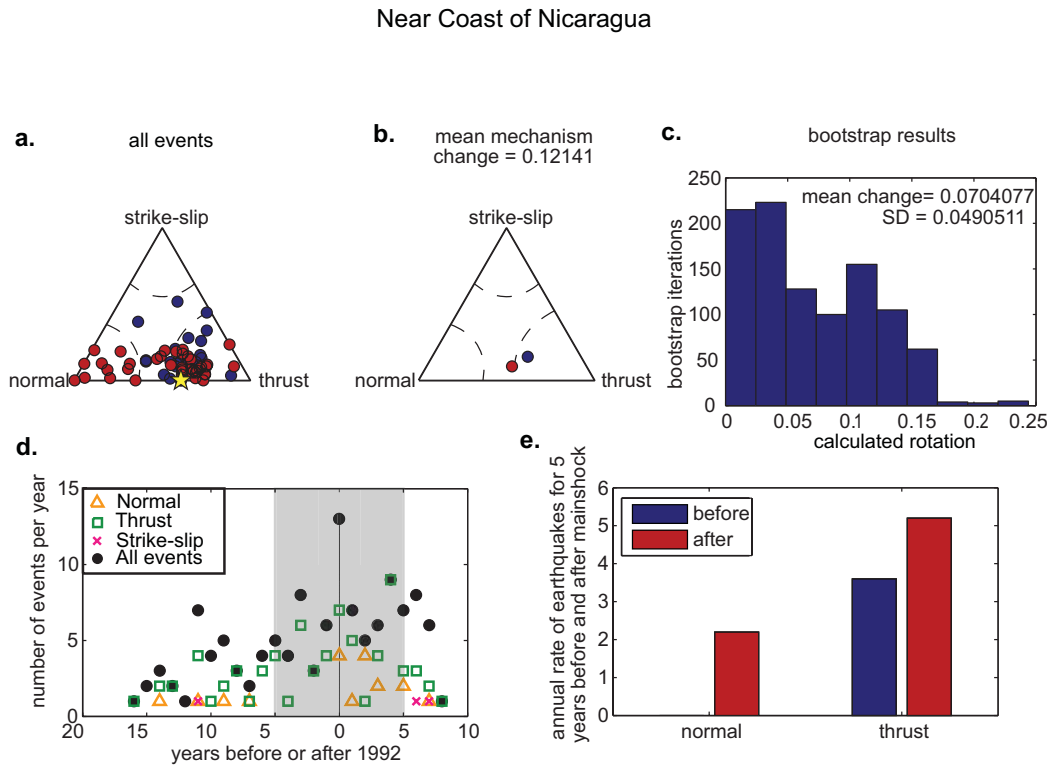
Figure 3.5: Statistics for the Near Coast of Nicaragua main shock. a. ternary plot of the main shock (yellow star), events before (blue dots), and after (red dots) the main shock. b. The mean mechanism before (blue) and after (red) the main shock and the mean mechanism change. c. Bootstrap results of the variability of focal mechanism orientation before the main shock with the mean change and standard deviation to test the significance of the observed mechanism change. d. plot of the number of events per year for all mechanisms showing the initial spike in seismicity at the time of the main shock. The grey box indicates the 5 years before and after the main shock which are used to determine the annual rate of earthquakes. e. The annual rate of earthquakes for the 5 years before and after the main shock. There is a decrease in the number of thrust events, thus, while there is an overall increase in the number of events after the main shock relative to before, there is a change in the mean mechanism and a decrease of at least one mechanism indicating a stress shadow. Despite the significant change in mean mechanism the number of events after the main shock increases for all mechanisms. Where there were no normal events before there are a substantial number after causing the change in mean mechanism.

The observation that, for 67 earthquakes of $M_s \geq 7$, only 2 show a decrease in seismicity for any mechanism indicates that stress shadows like the one following the 1906 San Francisco earthquake are rare, or are not identifiable with relatively short data sets (i.e. ±5 years) before and after the $M_s \geq 7$ main shock. This is important because it suggests that any signal of static stress triggering and especially shadows is subtle. This leads us to consider whether these signals can be extracted by stacking the data.

3.5 Stacked Data

There appear to be few significant changes in mean earthquake mechanism after individual mainshock events in the CMT catalog. However, the 1906 earthquake stress shadow would not have not have been readily apparent within the first 5 years after the mainshock either (the time span of our data). Thus, is it possible that stress shadows are present in our catalog, but are sufficiently small such that they are not apparent for individual events. However, by stacking the data we may begin to reinforce the signal. We combine the effects of multiple main shocks to identify any small signals that are not apparent for single events. We create three stacked catalogs grouped by main shock mechanism. Each catalog consists of all of the main shocks of a given mechanism and the associated events within each ± 2° boxes. For each stacked catalog we align all the main shocks to the same mechanism (arbitrarily chosen to be the central mechanism in the region of the ternary plot for that main shock mechanism). Mechanisms of each earthquake associated with each main shock are changed by the same amount, preserving the relative structural relationships. Once all the main shocks and associated earthquakes are aligned, they can be stacked. We then use these newly stacked catalogs to perform the average mechanism and significance calculations outlined in the method section.

Using the stacked catalogs we determine the number of events per year of each mechanism before and after the main shock (top row of Figure 3.6). The histograms in Figure 6 illustrate that in all cases, the number of events per year increases following the main shock for all mechanisms. However, one of the benefits of stacking the data is that by increasing the number of events analyzed we are better able to resolve small changes

in average mechanism than would not be apparent for a single main shock. To resolve small changes in average mechanism we grid the ternary diagram into equal 10-degree regions and calculate the difference in the number of earthquakes in the 5 years before and 5 years after the main shock for each stacked catalog. We calculate the rate change in each of the sub-grids in the ternary plot by:

$$\frac{n_a - n_b}{n_a + n_b} \tag{3.1}$$

where n_a is the number of events after the main shock and n_b is the number of events before the main shock. This gives a number between -1 and +1 where the sign indicates whether there is a rate increase (positive) or decrease (negative) and the magnitude of the value indicates the strength of the rate change. The bottom row of Figure 3.6 shows the results of determining the rate change in the gridded ternary diagram. The presence of blue grid cells indicates that we are beginning to illuminate decreases of certain mechanisms by the main shock. However, we still need to determine if this signal is statistically significant.

To test the significance of the sub-regions of decreased seismicity rate in the gridded ternary plots, we generate two different synthetic stacked catalogs. The first synthetic catalog is generated by randomizing the event time and the second catalog generated by randomizing the event mechanism while maintaining the same overall average mechanism (such that the overall distribution of mechanisms for a given main shock mechanism is preserved). Using the two synthetic catalogs we perform a Monte-Carlo analysis on the variance of the changes in the number of events in a grid cell and the change in average mechanism. The first row of Figure 3.7 shows the variance for the Monte-Carlo analysis on the synthetic catalogs with events randomized in time (light grey) and mechanism (dark grey) with the black line representing the variance for the global catalog. The variance for the global catalog is within the spread of the variances for the synthetic catalogs, indicating that the overall spread of the global catalog is the same as the spread of the synthetic catalogs. This implies that any significant changes in mean mechanism are due to the distribution of events following the main shock.
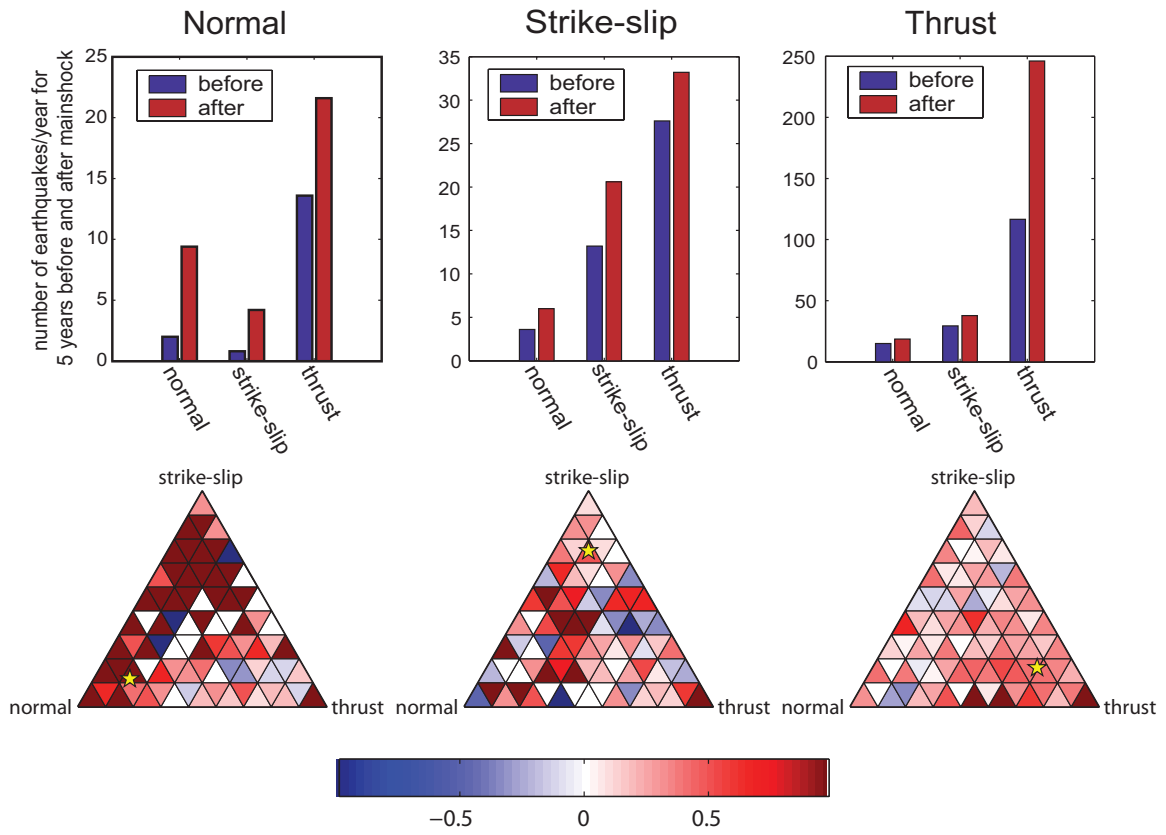
Figure 3.6: The number of events per year and rate changes for the stacked catalogs. Each catalog consists of main shocks of the same mechanism, and all the corresponding seismicity. Each of the main shocks is rotated to a mean mechanism in the center of the region on the ternary plot and stacked. The top row shows the number of events per year before and after the main shocks for each main shock mechanism. There is an increase in the number of events per year of all mechanism types following the main shock, but if we look at smaller sub-mechanisms as identified by gridding the ternary plots decreases in rate of certain mechanisms become evident as is shown in the bottom row. The color in each sub-triangle represents the normalized rate change following the main shock as defined by Equation 3.1. Blue represents a decrease in seismicity while red indicates an increase.

The change in mean mechanism following the main shock for both the synthetic catalogs and the global catalogs is shown in the bottom row of Figure 3.7. For all main shock mechanisms the change in average mechanism seen in the global catalog is significant at greater than 95% confidence compared to the synthetic catalogs. Figure 3.8 shows the mean mechanisms before and after the main shock for the stacked catalogs plotted on the ternary diagrams. The synthetic catalog changes in mechanism are shown as 1 and 2σ contours around the mean mechanism before the main shock (blue). Again, this plot illustrates that for all three main shock mechanisms, the change in average

mechanism following the main shock is significant at 95% confidence, indicating that globally, main shocks do change the average mechanism of events following an earthquake of $M_s \geq 7$. This indicates that while we can't say with confidence that a main shock will suppress earthquakes of a given mechanism, or even of a given sub-mechanism (from the gridded ternary plots), there is a change in the mean mechanism that may be indicative of static stress triggering.
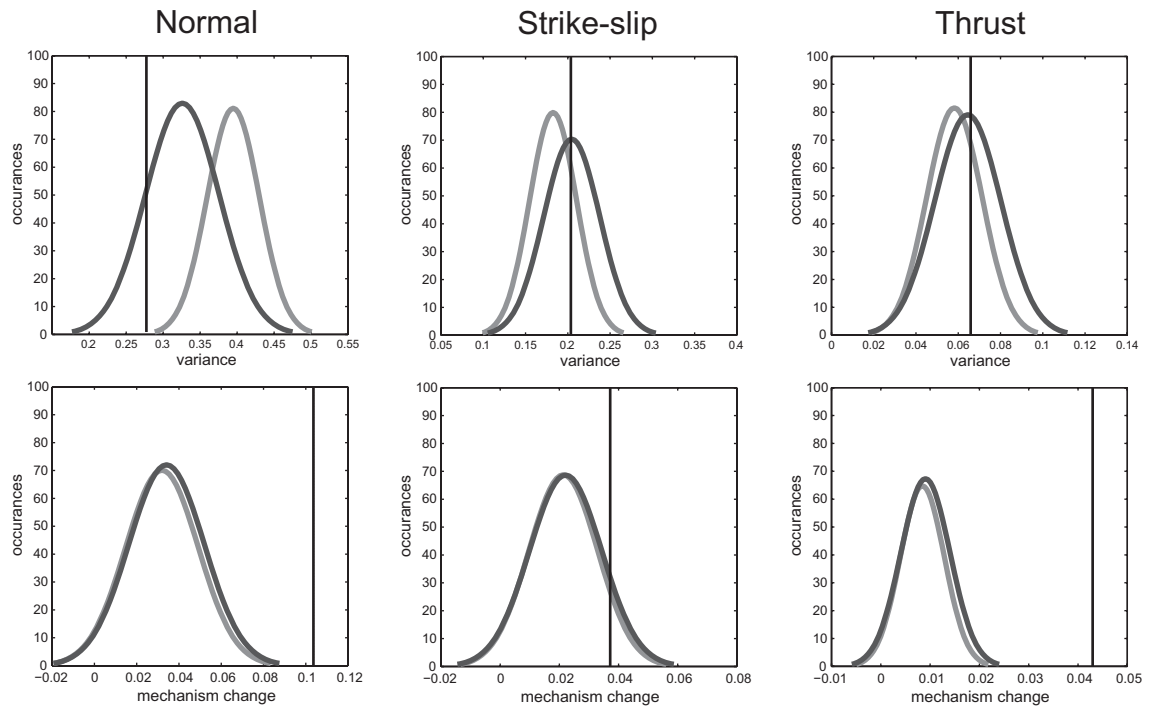
Figure 3.7: The variance and mean mechanism change for the stacked catalogs compared to Monte-Carlo simulations of two synthetic catalogs with events randomized in time (light grey) and mechanism (dark grey). The variance is calculated as simply the variance of the rate changes calculated for the sub-triangles in the ternary plots shown in the bottom row of Figure 3.6. The variance for the data falls within the variance for both the synthetic catalogs indicating that any significant changes to the mechanism is due to the actual distribution of events following the main shock. The bottom row indicates the change in mean mechanism for the data (black line) and the expected distributions of mechanism change for the two synthetic catalogs. For all three stacked catalogs the change in mean mechanism is significant at the 2σ level.
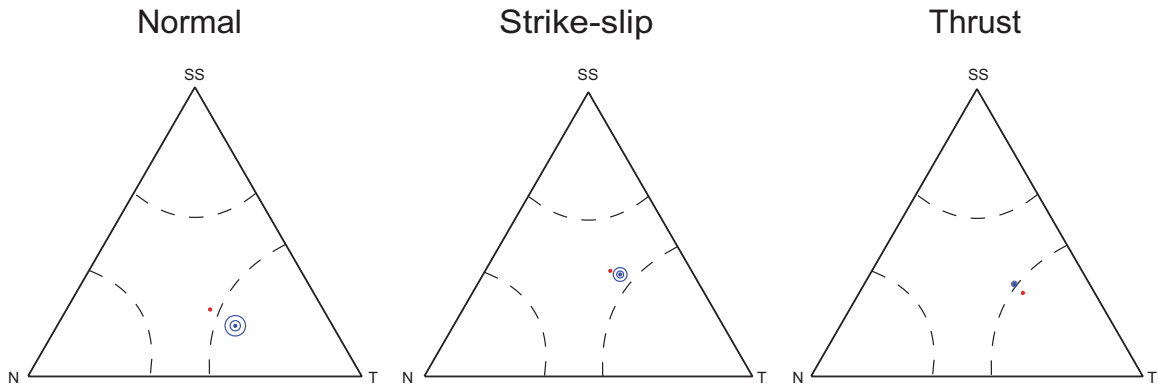
Figure 3.8: Another way of representing the significance of the change in mechanism for each of the stacked catalogs. The blue and red dots indicate the mean mechanism of the data before and after the main shock, respectively. The 2 blue contours around the mean mechanism before the main shock indicate the 1 and 2σ mechanism changes expected for the synthetic catalogs. In all cases the observed mechanism changes lies outside the 2-sigma contour.

An alternative explanation of the observed change in average mechanism following $M_s \geq 7$ main shocks is that some regions were dominated by certain earthquake mechanisms before the main shock, but that after the main shock there are events of all mechanisms. This result is could be caused by static or dynamic stress triggering. As an experiment, we eliminate events in the first year following the main shock which may be most affected by dynamic triggering signals. *Parsons* [2002] found that globally, there is a large initial spike in seismicity following a $M_s \geq 7$ main shock that occurs in stress shadow zones that decays back to the background rate in the first year; that population of aftershocks might most readily be explained as dynamically-triggered events. If we remove all events that occurred during the first year after main shocks, are there significant changes in mechanism?

We repeat the analysis on the stacked data after removing events that occurred in the first year following the main shock. The first row of Figure 3.9 shows the number of events per year before and after the main shock. The seismicity rate increases are substantially smaller than when the first year following the main shock is included (Figures 3.6 and 3.9). There remains a modest increase in normal events following normal and thrust main shocks. There is now a small decrease in the average rate of normal and strike-slip events following strike-slip main shocks, though the changes are small enough that their significance is questionable. The bottom row of Figure 3.9 shows
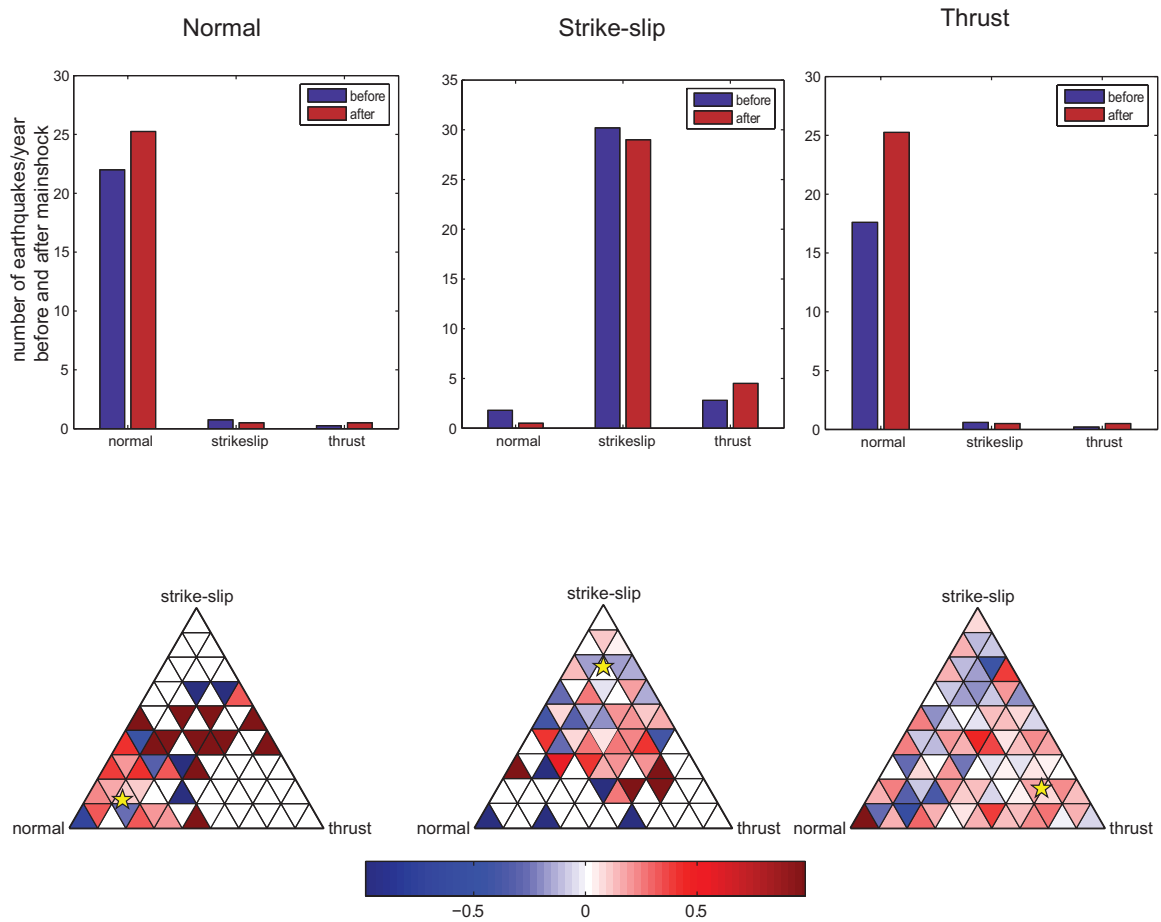
Figure 3.9: The number of events per year and rate changes for the stacked catalogs excluding the first year following the main shock. The top row shows the number of events per year before and after the main shocks for each main shock mechanism. There are now slight decreases in the number of events of strike-slip and normal events following strike-slip main shocks. The bottom row indicates the change in rate for sub-mechanisms on the ternary plot. The color in each sub-triangle represents the normalized rate change following the main shock as defined by Equation 3.1. Blue represents a decrease in seismicity while red indicates an increase.

the gridded ternary plots with the colors indicating the change in seismicity rate following the main shock in each sub-grid. In all cases there are more sub-grids that show seismicity rate decreases, but again, the question is whether these changes are significant. Figure 3.10 shows the variance and change in average mechanism for the data (black line) compared to Monte-Carlo analysis for synthetic catalogs randomized in time (dark grey) and mechanism (light grey). Unlike when the first year following the main shock is included, the data variance falls outside the spread of the synthetic catalog variance at 95% confidence in all but one of the cases. However for all 3 of the main

shock mechanisms the change in average mechanism is significant at the 2-sigma level (Figure 3.10 b and c).

Statistically significant changes in the mean mechanism of the stacked catalogs are present whether or not the first year of data following the main shock is included, despite the differences in the variances of the stacked catalogs relative to the synthetic catalogs. This indicates that when the first year of data is included some of the change in mechanism observed is due to turning on events of all mechanisms (i.e. dynamic triggering). However, when the first year of data is removed, the variance of the stacked catalogs is significantly different than that of the synthetic catalogs indicating that any observed change in mechanism is not due to turning on events of all mechanisms, but turning on or off selective mechanism (i.e. static triggering). This, it is less likely that the change in mechanism is due to events of all mechanisms being triggered by the main shock since there is a significant change in mean mechanism when the first year of events following the main shock are removed. This indicates that while the signal is very subtle, and superimposed on a dynamic stress triggering signal, the changes in average mechanism following $M_s \geq 7$ are likely indicative of static stress triggering.
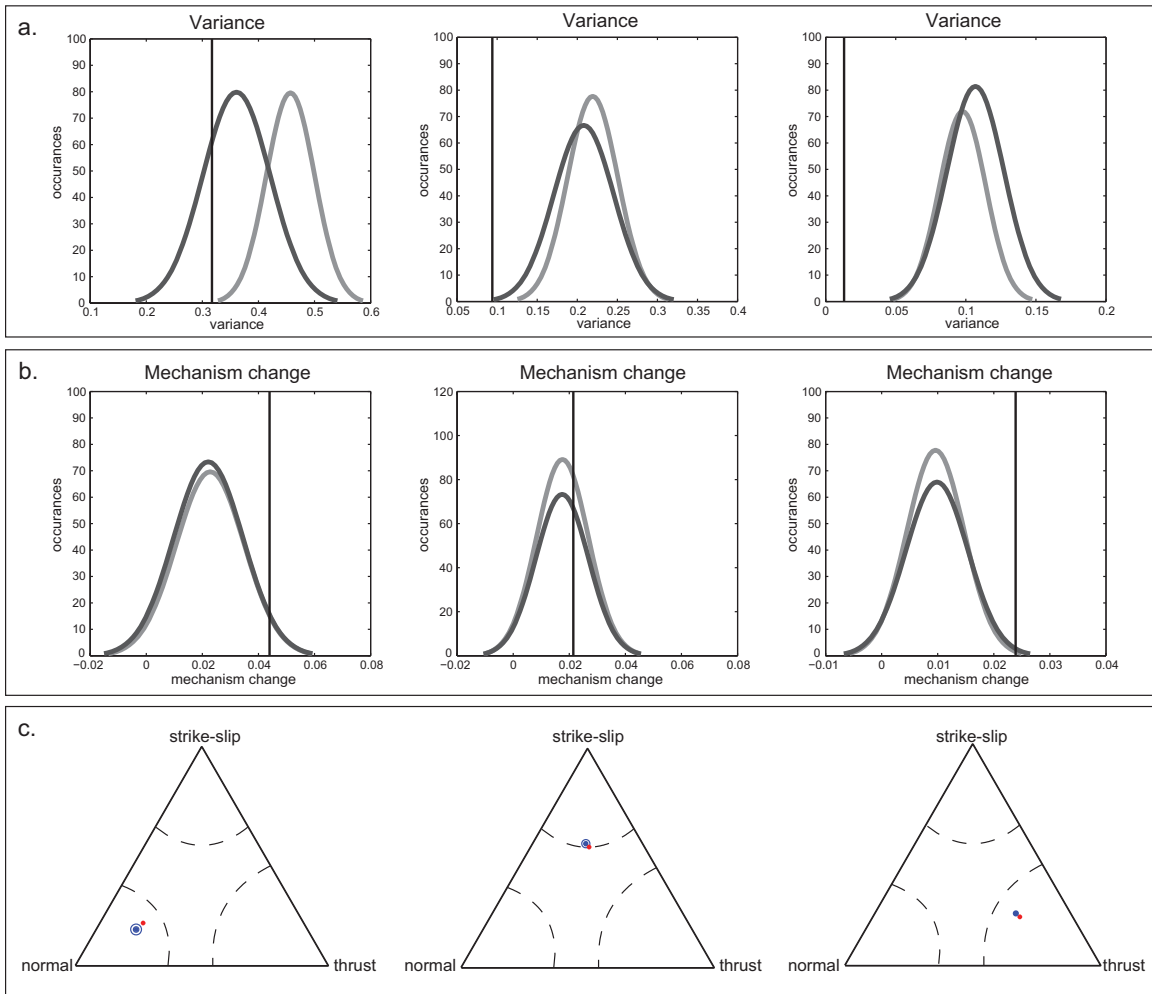
Figure 3.10: Comparison of the variance and mechanism change for the stacked catalogs excluding the first year following the main shock and the two synthetic catalogs. Again, the mechanism change observed in the data is significant at the 2σ level over what is expected from the synthetic catalogs.

3.6 Discussion

We began this study looking for changes in the mean mechanism of earthquakes associated with individual $M_s \geq 7$ events induced by the main shock that would indicate a stress shadow according to the definition established at the beginning of this paper. Of the 67 main shocks that were identified as potential triggering events, 13 showed a mechanism change significant at the 1σ level. However, only 2 of these 13 events didn't show an over-all increase in seismicity rate across all focal mechanisms. Thus, for only

two of the 67 main shocks could a dynamic process not explain observed seismicity rate changes. These two events may exhibit a stress shadow caused by changes in the static stress. This indicates that obvious stress shadows are rare globally.

If stress shadow signals induced by changes in the static stress are subtle, it is possible that the stress shadows are still present, but can not be resolved for individual events. Using the global catalog of main shocks and their associated events, we stacked the data for each main shock mechanism to amplify any small signals present. The increased number of events allowed us to grid our ternary plots, and examine seismicity rate changes in smaller mechanism bins. We found that rate decreases could be resolved for some sub-mechanism bins, but the significance of the decreases in any part of the ternary diagram was not statistically significant. However, the changes in average mechanism following the main shock in the stacked data sets were statistically significant. The change in mechanism in the data was significant at the 2σ level compared to synthetic catalogs where the events were randomized in both time and in mechanism.

The mean mechanism change in the stacked data sets does not fit our definition of a stress shadow because it is accompanied by an increase in all mechanisms. Thus the mechanism change could be interpreted as dynamic earthquake triggering. If there were very few, or no events of a given mechanism before the main shock, and then after the main shock, events of all mechanisms were increased, there would be a change in the average mechanism. This result could be due to either a static or dynamic triggering processes. By removing the first year of events following the main shock, we limit most of the events that may have been triggered by dynamic stresses. In that instance we observed statistically significant suppression of sub-mechanisms, thus the overall change in mean mechanism may represent static stress shadowing. However, that we can only resolve these changes in average mechanism indicative of a stress shadow after stacking the data indicates that the role of static stresses in changing seismicity rates is very subtle, We thus cannot rule out a hypothesis that the majority of earthquake triggering results from a dynamic process, but we can identify a static stress process operating at some level.

These results are consistent with observations made by *Parsons* [2002] for the evolution of seismicity globally following events M$_s$ ≥ 7 for regions of static shear stress increase and decrease (Figure 3.11). The light grey line indicates events associated with

Harvard CMT Catalog: Triggered Earthquake Rate vs. Time
Rates before and after 117 Ms>7 earthquakes shown stacked
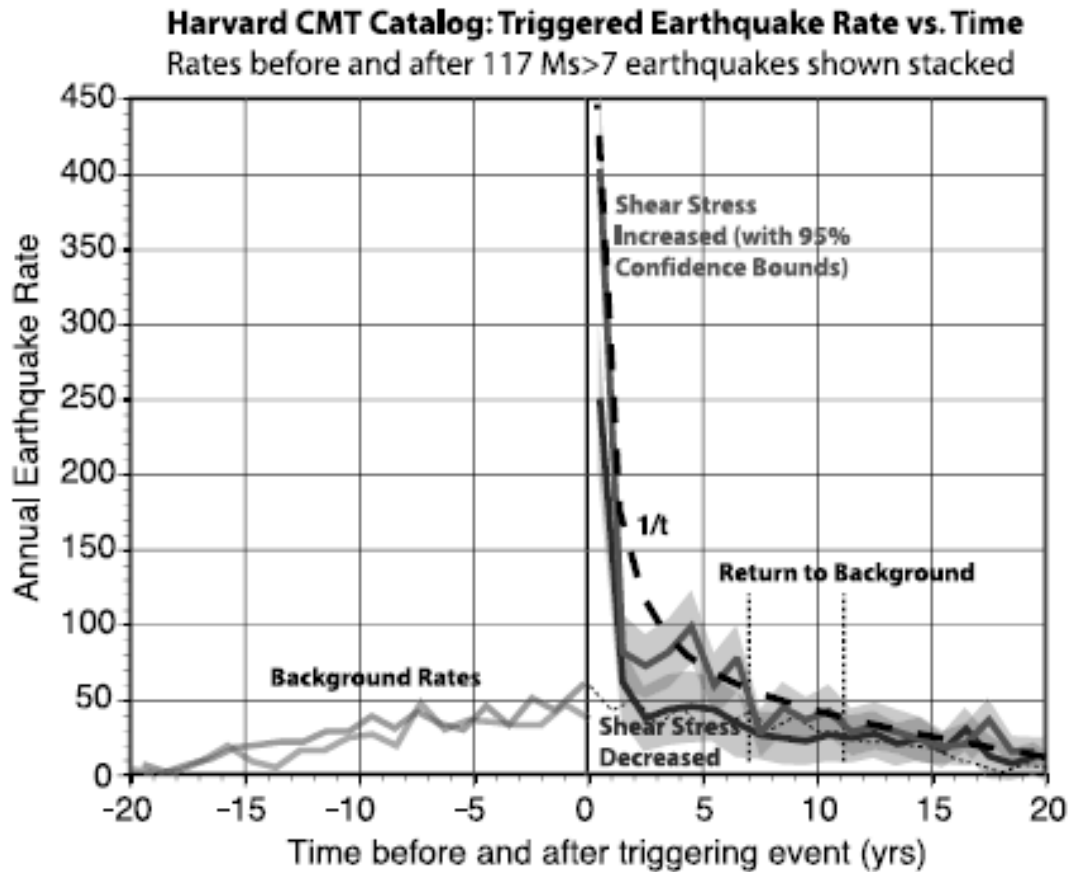
Figure 3.11: Modified after *Parsons* [2002]. That there is a spike in both number events that see shear stress increases and decreases is indicative of dynamic triggering being a part of the signal. The additional number of events that experience a shear stress increase is likely indicative of changes in static stress. The increases in the dark grey line drop back to the background quickly supporting a dynamic mechanism where there are few to no long term effects on the seismicity rate. The larger increase in the light grey line can be explained by a combination of both static and dynamic triggering. The initial increase in the red line also drops off quickly as expected for dynamic triggering, but remains higher than the background for more than 5 years indicative of static triggering. This overprinting of both static and dynamic effects is likely the reason that stress shadows are very rarely observed for individual earthquakes, and it is only with the stacking of data on a global scale that we are able to begin to resolve them, but even then the signal is subtle and not the strong 1906-type signal predicted by traditional stress shadow studies.

an increase in the shear stress due to the main shock while the dark grey line indicates events associated with a shear stress decrease. While both lines show a significant spike in seismicity following the main shock followed by an Omori-type decay, the increase in the number of events in areas of shear stress increase is almost twice as large as that for

events in areas of shear stress decrease. The observations made by Parsons [2002] coupled with the results of this work imply that the increase in rate for events experiencing a shear stress decrease is due to dynamic triggering while the increase for events experiencing a shear stress increase is likely due to both dynamic and static triggering. The difference in the magnitude of the spike in seismicity rate for the regions experiencing shear stress increase versus a shear stress decrease can possibly be attributed to the triggering of events by static stress changes. In addition, the events associated with shear stress decreases drop back to the background seismicity rate in approximately 1-2 years following the main shock while the events associated with shear stress increase take 8-12 years to return to the background rate. The overprinting of both static and dynamic effects likely explains why stress shadows are rarely observed for individual earthquakes. Further, static stress changes caused by slip heterogeneity in the main shocks that was not modeled here or by *Parsons* [2002] is expected to generate isolated zones of seismicity increases within broad shadow zones [*Marsan*, 2006 *Dieterich*, 2005]. We were required to stack seismicity from a global catalog to overcome these effects and resolve stress shadows. However, the stress shadow signal from the global catalog was still not the strong 1906-type signal that often informs our thinking, although with only a ±5-year observation period as we've applied in this study, we might have had a difficult time identifying the 1906 shadow, the impact of which is most evident over ±75 year periods [*Bakun*, 1999; *Stein*, 1999]. Instead we observe changes in average mechanism, which might be a more typical form of stress shadow.

Our observation that the static signal is very subtle and requires stacking of many events to resolve is consistent with work by *Pollitz and Johnston* [2006]. Examining aftershock rates associated with both impulsive and aseismic M~5 events near San Juan Batista, CA, *Pollitz and Johnston* [2006] find that the impulsive events trigger much higher aftershock activity. As the moment release of the impulsive and aseismic events is roughly equivalent, they attribute the difference in aftershock rate to the dynamic stresses following the impulsive events, which the aseismic events lack.

Clearly identified stress shadows, similar to the one observed following the 1906 San Francisco earthquake, appear to be rare globally. However, the 1906 shadow was

observed as a decrease in the number of M=6 events and took decades to become apparent, much longer than our catalog data. Thus, it could be argued that not seeing stress shadows for individual events in our catalog is not an indication of the lack of stress shadows, but that our catalog is too short to identify the change in seismicity rate. It is also possible that if the catalog following the 1906 earthquake were complete down to M=4, the stress shadow would have become apparent earlier due to the greater number of background M=4 and 5 events compared to M=6 events. In addition, the 1906 San Francisco earthquake was unusual in that it was an extremely long strike-slip rupture with most of the regional faults sub-parallel to the rupture, reducing the static stress on most of the active faults in the region. Since the global catalog is dominated by thrust events, and events with ruptures much shorter than the rupture of the San Andreas Fault in 1906 it isn't surprising that we don't see many seismicity rate reductions following $M_s \geq 7$ events globally, and in fact the lack of rate reductions does not appear to be very diagnostic of stress shadows after all. Instead, we suggest that static triggering (and thus, shadows) does occur by the demonstration of a mean mechanism change following the main shock. This indicates that the static stress model for earthquake triggering and suppression cannot be excluded; at the same time it appears that the static signal is very subtle and is generally not resolvable until many events are stacked. Thus, the observed changes in seismicity rate that are observed following most individual main shocks appear to be dominated by the dynamic stresses as was found by *Pollitz and Johnston* [2006].

3.7 Conclusions

Globally we find that out of 67 testable main shocks, only 2 show changes in seismicity rate and average mechanism that can not be explained by dynamic effects. However, by stacking all the events by the main shock type and gridding associated earthquakes by mechanism, there do appear to be sub-mechanisms that show decreases in seismicity following the main shock, but these observed decreases in seismicity are not statistically significant. There is a significant change in the mean mechanism following the main shock for the 5 years following the main shock, and for some sub-mechanisms when the first post-main shock year is excluded. We thus conclude that stress shadows

are present, but that their signal is subtle and is not identifiable for most main shocks taken individually. In addition, since for none of the 67 main shocks $M_s \geq 7$ examined was there a traditionally defined stress shadow, a decrease in overall seismicity similar to what was observed post-1906, appears to be very rare, at least on the time scales of most seismicity catalogs. While over longer time periods decreases in seismicity similar to those observed following the 1906 San Francisco earthquake may be present, the blanket assumption that seismic risk is lower in the years following a major earthquake may not be accurate. In this work we have been able to identify very subtle signals of static stress shadows, indicating that stress shadows may need to be incorporated into hazard calculations. However, the more conservative hazard estimates would benefit from not assuming there will be a decrease in seismic hazard following major earthquakes as the stress shadow signals found in this study were very subtle on a 5-year time scale.

Chapter 4

Subsidence in the Louisiana Coastal Zone due to Hydrocarbon Production[3]

Abstract

Coastal wetland loss in southern Louisiana poses a great threat to the region's ecologic and economic stability. Wetland loss in the Louisiana Coastal Zone is caused by the interactions of multiple natural and human induced mechanisms, and it has been suggested that subsurface oil and gas production may be a large contributing factor. We model the effect of oil and gas production in Lafourche Parish, Louisiana on surface subsidence using a first-order leveling line along highway Louisiana 1 to constrain our model. Using geologic and pressure data, we estimate the amount of compaction in modeled reservoirs. We find the subsidence predicted from reservoir compaction is consistent with observations of localized subsidence between 1982 and 1993. Both modeling and observations show that subsidence due to reservoir compaction is a highly localized signal that is not consistent with observations of regional subsidence. Interestingly, while predictions of subsidence from compaction of the reservoir sands fit the observed subsidence in one time epoch, the leveling data shows an increasing rate of

subsidence from the 1965-1982 to 1982-1993 epoch – a time when production rates decreased. This indicates the potential for a time-dependent mechanism for production-induced subsidence. This work is a critical part in the development of an integrated model of subsidence and wetland loss in southern Louisiana.

4.1 Background

About 40% of the United State's coastal wetlands are located in Louisiana and land loss in the Louisiana Coastal Zone accounts for 80% of the total coastal wetland loss in the United States since the 1930s. If wetland loss continues at this rate the Louisiana Coastal Wetlands Conservation and Restoration Task force and the Wetlands Conservation and Restoration Authority (COAST 2050) estimate the lost public use value to exceed $37 billion by 2050.

In Louisiana, wetland loss is a combination of land subsidence along with eustatic sea level rise or ~2.29 mm/yr [*Penland, et al.,* 1988], sediment accumulation, erosion, and filling and drainage [*Boesch, et al.,* 1994]. *Penland et al.* [1988; 2000] determined that more than half of the land loss in coastal Louisiana between 1932 and 1990 was related to subsidence, which itself is the combination of multiple mechanisms, both natural and anthropogenic. There is natural subsidence due to compaction of Holocene, Pleistocene, and Tertiary sediments, lithospheric flexure due to the Mississippi delta, and tectonic activity along the regional growth faults. In addition, there are the anthropogenic effects of subsurface fluid withdrawal, induced faulting due to fluid production, and the absence of sedimentation which enhances the natural compaction signal (Figure 4.1). These various mechanisms all produce different temporal and spatial signatures. Compaction of Holocene sediments in the Mississippi River delta results in a spatially variable, but temporally constant subsidence pattern [*Suhayda, et al.,* 1993] and contributes between 0.1 and 1 mm/yr to overall subsidence rates [*Kooi and de Vries,* 1998]. Lithospheric flexure, as a response to sediment loading, has been shown to lead to geological subsidence rates of 0.05 mm/yr for other portions of the gulf coast [*Scardina, et al.,* 1981; *Paine,* 1993]. Much of the wetlands losses identified in aerial photographs are inferred to be on the downthrown sides of faults. It has been suggested
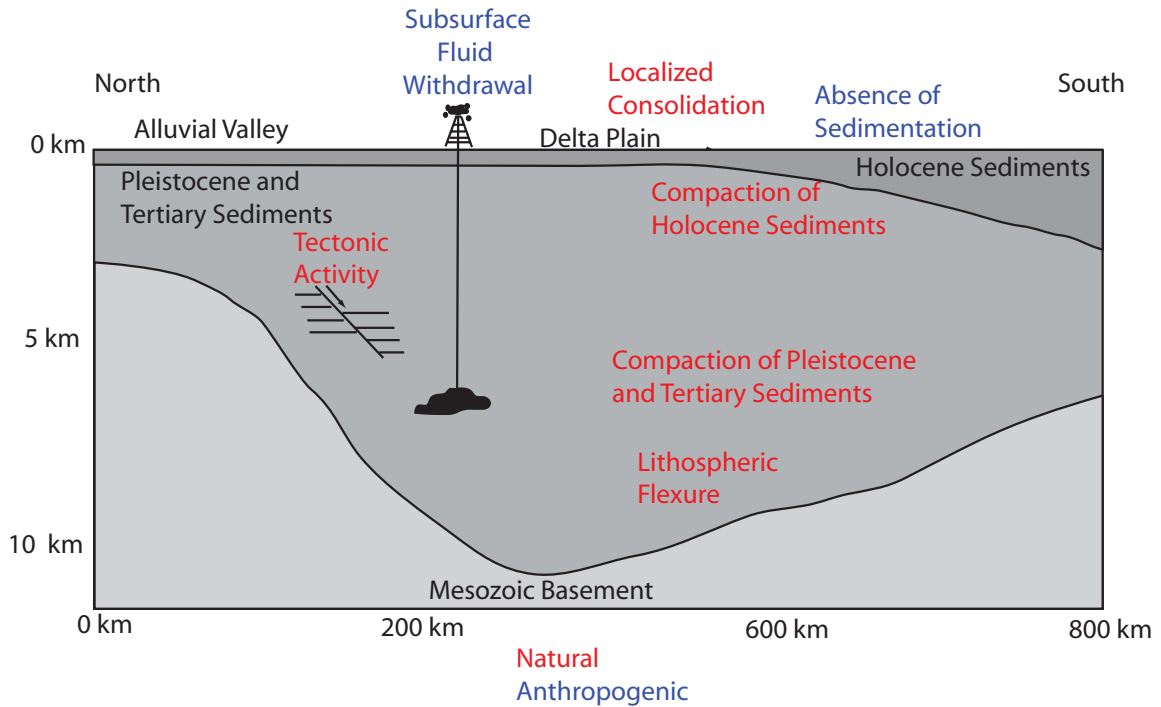
Figure 4.1: Mechanisms of subsidence. Red text indicates natural mechanisms; blue text indicates anthropogenic mechanisms; green text indicates processes affected by both natural and anthropogenic processes. Modified after *Penland et al.*,1989.

that much of the wetland losses are related to natural episodic movement along these faults [*Gagliano, et al.*, 2003; *Dokka*, 2006]. However, due to the time spanned by aerial photographs and leveling surveys it is impossible determine the component of subsidence due to the faults as opposed to other mechanisms. The subsidence rate from these four mechanisms (~3 mm/yr) is significantly lower than the observed historical subsidence rates of 9 mm/yr to as high as 23 mm/yr locally [*Morton, et al.*, 2002]. The effect of hydrocarbon production-induced fault reactivation and reservoir compaction on surface subsidence has been suggested as a means of explaining these recent high subsidence rates [*Sharp and Hill*, 1995; *White and Morton*, 1997; *Morton, et al.*, 2001; 2002; 2003b; 2005b; 2005a; 2006].

Subsidence related to subsurface fluid withdrawal in the Gulf of Mexico region was first recognized along the Texas coast [*Swanson and Thurlow*, 1973; *Neighbors*, 1981]. In the Houston-Galveston area subsidence rates of up to 120 mm/yr greatly exceeded the natural subsidence rates estimated to be up to 13 mm/yr. *Gabrysch and Copland* [1990] found that the rapid subsidence rates and subsidence of up to 3 m was

induced by large-scale groundwater withdrawal forming a large subsidence bowl. In Louisiana it has been more difficult to link wetland loss to fluid withdrawal as both are pervasive throughout the region and the land loss is likely caused by many interacting processes and conditions. Previously, many authors felt that oil and gas production would only cause local subsidence and be small due to the depth of production and thus have little affect on regional wetland loss. [*Suhayda*, 1987; *Coleman and Roberts*, 1989; *Boesch, et al.*, 1994]. However, *Morton et al.* [2001] found that periods of rapid wetland loss corresponded to times of high oil and gas production and inferred that the fluid production was driving the wetland loss (Figure 4.2). We can use the analytical method developed by *Geertsma* [1973] to model the role that hydrocarbon production at depth has on the observed surface subsidence and resulting land loss in the Louisiana Coastal Zone (LCZ).
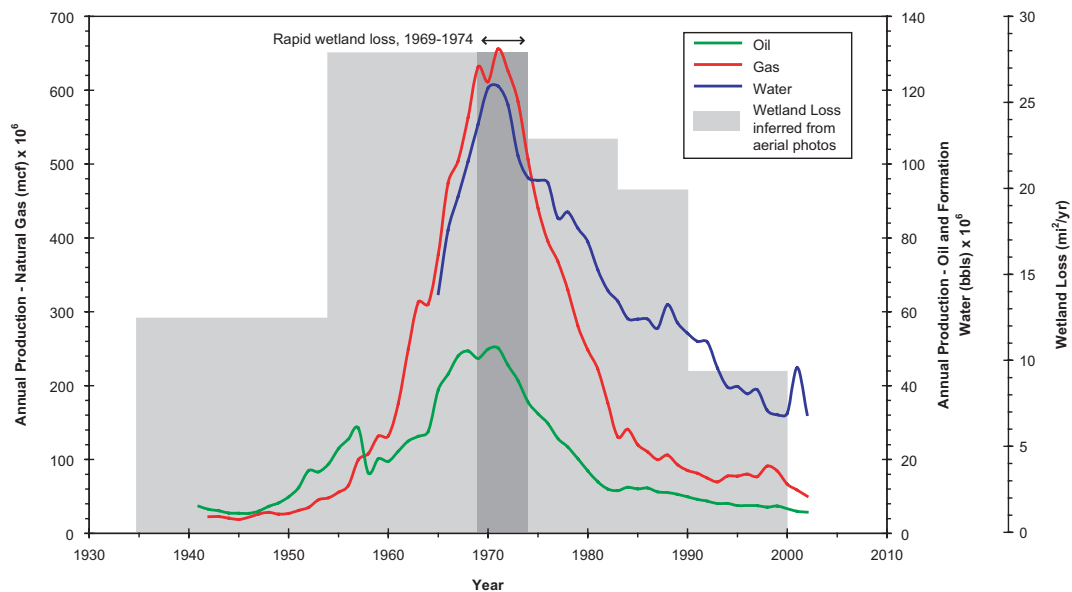
Figure 4.2: Cumulative annual production data for the Louisiana Delta Plain. Morton noted that the period of rapid observed wetland loss as shown by the dark grey box coincided well with a peak in the fluid production in the Louisiana coastal zone. This observation led *Morton et al.* [2005b] to conclude that the fluid withdrawal was driving the observed wetland loss. (Figure modified from Morton et al., 2005b)

4.2 Study Area

In this work we extend the work of *Chan and Zoback* [2007] which modeled the role of subsidence due to production on the Lapeyrouse field and induced faulting along the Golden Meadow Fault by building a more regional model of subsidence due to hydrocarbon production in Lafourche Parish, Louisiana. This is an ideal location because there is a first-order leveling line along Louisiana Highway 1 (LA 1) from Grand Isle in the south to Racelend in the north, with multiple time epochs and recently re-calculated rates, which crosses multiple large oil and gas fields and regional growth faults (Figure 4.3) [*Shinkle and Dokka*, 2004]. While leveling is an older geodetic technique and only provides changes in vertical elevation, the leveling data provide a better profile across the study area and cover a longer time period than the GPS in the region which is sparse and
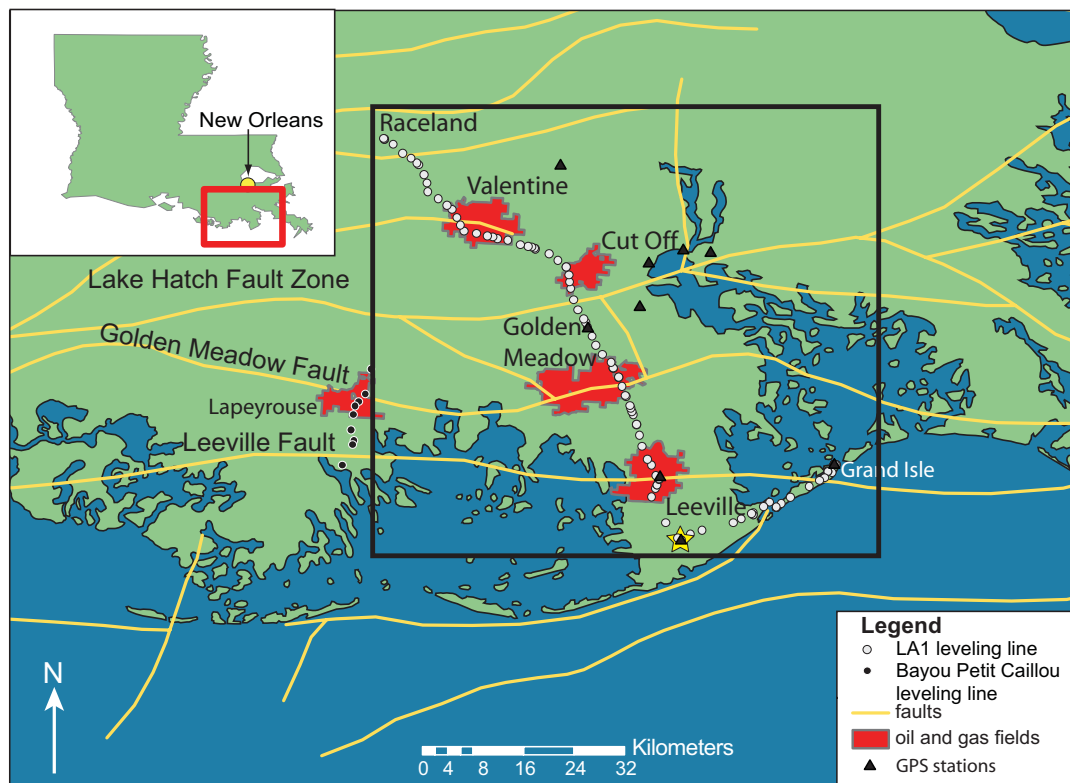
Figure 4.3: Regional map showing the major oil and gas fields of Leeville, Golden Meadow, Cut Off, Valentine and Lapeyrouse, the leveling lines used in *Chan and Zoback* [2007] (black circles), and this study (white circles), the regional faults in gold, and the GPS stations as black triangles. The black box indicates the modeled area in this study. All profiles along the leveling line will be relative to the station marked by the yellow star.

consists of stations with short time series. In addition, this is an area where small amounts of subsidence can have a large impact as the region has elevations between 1 and 5 meters above sea level. In addition, LA 1 is the only hurricane evacuation route for the estimated 80,000 residents in southern Lafourche Parish including Port Fourchon, Louisiana's southernmost port, and an important port for oil and gas. Much of this road is built on levees within the wetlands or on small areas of land surrounded by wetlands. There are also numerous wetland restoration projects in this area making it critical that we understand the mechanisms causing subsidence and wetland loss so that restoration efforts can be carried out effectively.

Shinkle and Dokka [2004] recently recalculated elevation rate changes for a network of leveling lines throughout Louisiana, including the leveling line along LA 1. There are multiple epochs of leveling data, but here we present only the elevation changes between 1982 and 1993. The elevation changes shown in Figure 4.4 are all
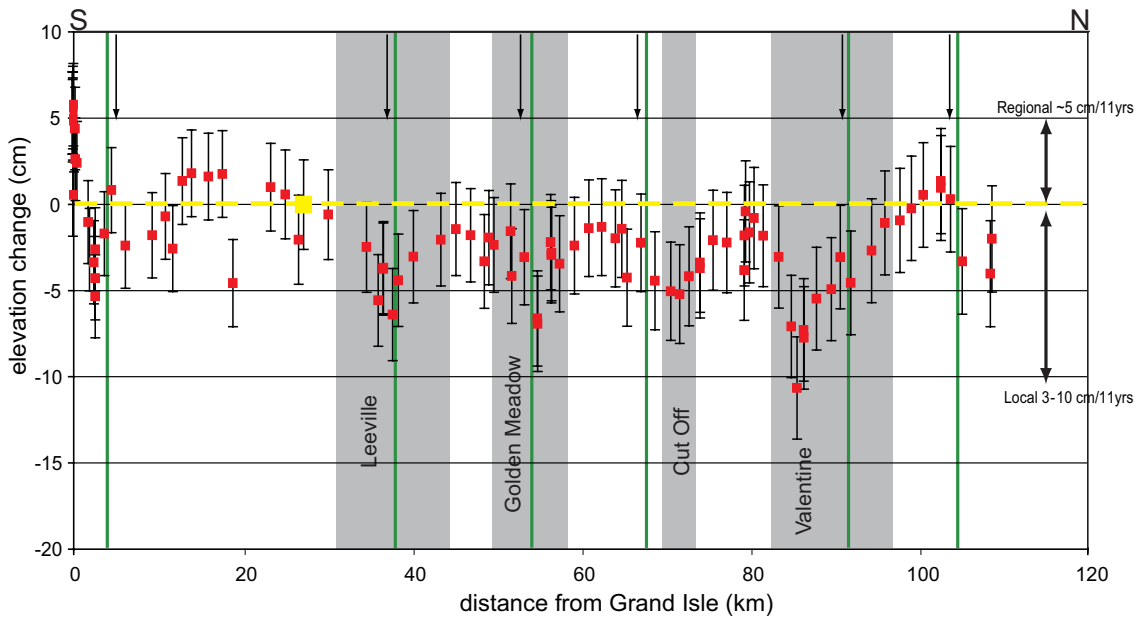
Figure 4.4: Leveling line between Grand Isle in the south and Raceland in the north showing subsidence in cm for 1982-1993 epoch relative to the station in yellow. The extent of the oil and gas fields crossed by the leveling line are indicated by grey boxes. Inferred locations of the regional normal faults are indicated by green lines with arrows indicating down thrown side. However, due to no surface expression of the faults their location relative to the leveling line may move as much as 2-3 stations in either direction. The leveling line shows ~5cm of regional subsidence relative to Grand Isle with additional localized subsidence of ~3-11 cm over the 1982-1993 leveling epoch.

relative to the station marked by the yellow square, however, the line originated at Grand Isle, and this base station is tied to a tide gauge and GPS station at the Coast Guard Station. The error bars represent the error in measuring elevation at each location along with the error accumulated along the leveling line. The entire line shows a regional subsidence signal on the order of ~5 cm, with regions of higher localized subsidence of ~3-11 cm. These areas of higher subsidence correlate well with the Leeville, Golden Meadow, Cut Off, and Valentine oil and gas fields, and the inferred location of the regional growth faults.

The regional map only shows the major oil and gas fields that the leveling line along LA 1 crosses, however oil and gas fields are pervasive through southern Louisiana and the region of high rates of land loss. This, along with the observation that periods of wetland loss correlated well with periods of high fluid production [*Morton, et al.*, 2005a], leads to our two motivating questions: (1) is the subsidence signal higher over the oil and gas fields? and (2) does the rate of subsidence correlate with the rate of oil and gas produced?

4.3 Method

The Geertsma solution is an analytical model for estimating the surface deformation due to the depletion of an idealized reservoir of radius R at depth D [*Geertsma*, 1973]. The Geertsma solution calculates the vertical and radial components of surface displacement from:

$$u_z(r,0) = -2C_m(1-\nu)\Delta p H R \int_0^\infty e^{-D\alpha} J_1(\alpha R) J_0(\alpha r) d\alpha$$

$$u_r(r,0) = 2C_m(1-\nu)\Delta p H R \int_0^\infty e^{-D\alpha} J_1(\alpha R) J_1(\alpha r) d\alpha$$

(4.1)

Where u_z is the vertical displacement and u_r is the radial displacement for a reservoir of radius R at depth D and thickness H. C_m is the compaction coefficient of the reservoir, ν is the Poisson ratio, Δp is the change in pore pressure, r is the distance from the center of the reservoir on the surface, and J_0 and J_1 are Bessel functions. We can define the change in height of the reservoir as:

76

$$\Delta H = \int_0^H C_m(z)\Delta p(z)dz \qquad (4.2)$$

However, C_m as defined by Geertsma is not an appropriate estimate of the compaction coefficient as it is assumed to be the same throughout the entire half space as opposed to the reservoir having a different compaction coefficient than the surrounding medium. Instead, we estimate ΔH using Deformation Analysis in Reservoir Space (DARS) [*Chan and Zoback*, 2002; *Chan*, 2004] which incorporates the bottom hole pressure decline, an elastic-plastic end cap constitutive law for reservoir sands developed for an off shore Gulf of Mexico reservoir, and a generalized stress path for the Gulf of Mexico.

A generalized Geertsma solution is shown in Figure 4.5 which allows for a first-order estimation of surface displacements for reservoirs of various sizes and depths. The shallower the reservoir is the larger and more localized the surface signal is. However, even for deep reservoirs where the surface signal is broader the deformation is still limited to within approximately three reservoir radii.

Chan and Zoback [2007] extended the observations of *Morton et al.* [2005a] by adding numerical and analytical models, which incorporated physical changes in the formations associated with depletion and the resulting stress changes, to estimate surface subsidence due to oil and gas production in the Lapeyrouse field in Terrebonne parish and the potential for induced slip along the nearby Golden Meadow Fault. They used changes in reservoir pore-pressure to model the role of reservoir compaction on surface subsidence and compared this to observations of elevation change along a leveling line that transects the study area. Surface subsidence predicted by only compaction of the reservoirs did not fully explain the subsidence observed along the leveling line, thus *Chan and Zoback* [2007] then created a numerical model to determine the effect that the compacting reservoirs have on the nearby Golden Meadow Fault. They were able to show that depletion of oil and gas reservoirs in the Lapeyrouse field can have a significant impact on surface subsidence and fault slip locally; however, they were still not able to fully reproduce the subsidence observed along the leveling line. One of the limitations of this local study is that the Golden Meadow Fault lies to the north of the
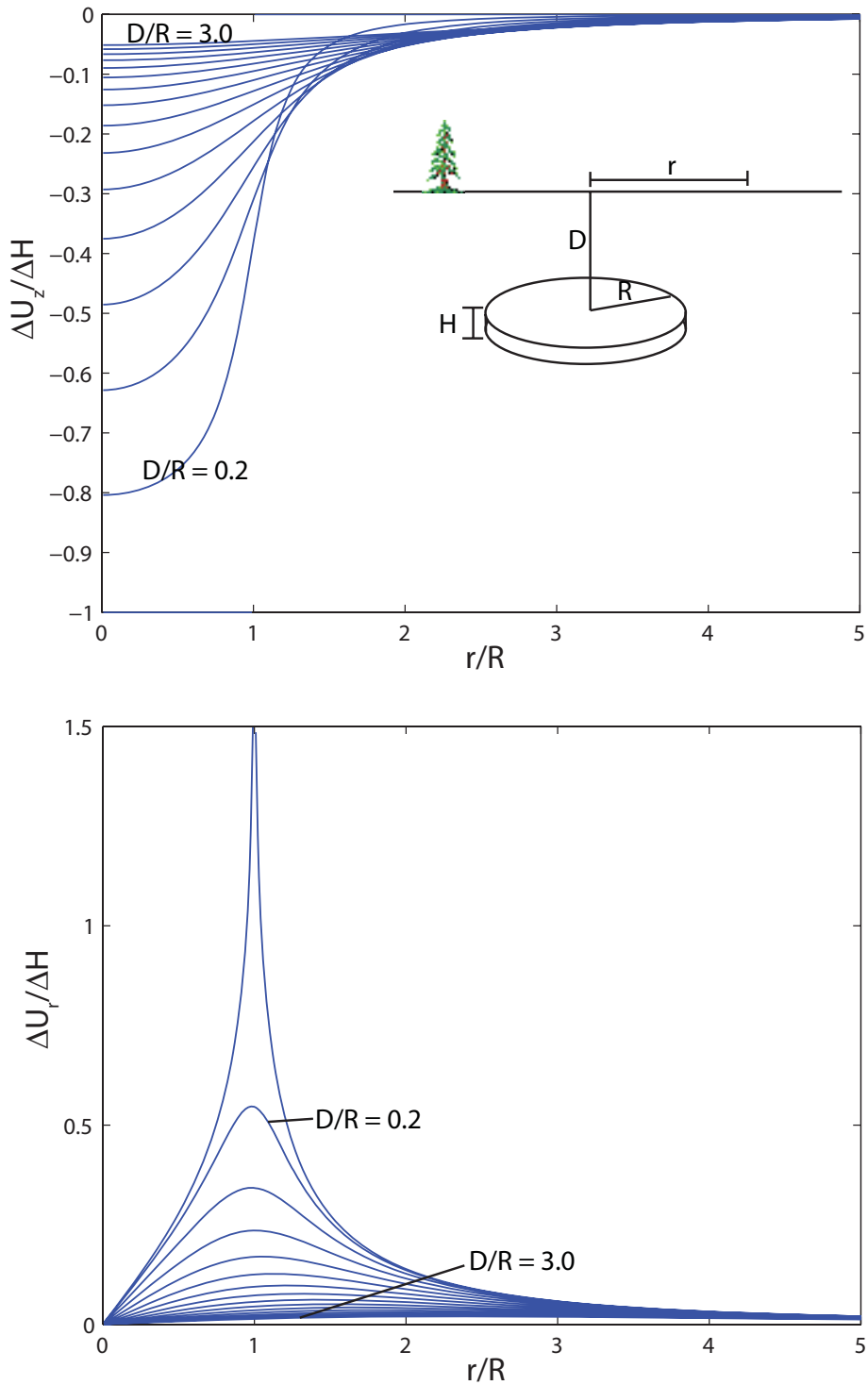
Figure 4.5: Generalized Geertsma solution for varying ratios of reservoir depth (D) and radii (R) [*Geertsma*, 1973]. The top panel shows the vertical displacements observed at the surface, and the second panel shows the horizontal displacements observed at the surface. As the reservoirs become deeper the surface signal becomes broader, but is still limited to ~3 reservoir radii.

modeled reservoirs and the Lapeyrouse field whereas in much of the LCZ the large fields are cut by the regional faults or there is production on both the upthrown and downthrown sides of the fault. The findings of *Chan and Zoback* [2007] indicate that subsurface fluid withdrawal is a mechanism that needs to be seriously considered when modeling subsidence in the LCZ, and that future modeling should be more regional in order to incorporate it with other subsidence mechanisms and to accurately assess its impact on the regional subsidence picture.

We use well logs and pressure data over the same time period as the leveling data (in this case 1982-1993) from the Leeville, Golden Meadow, Cut Off, and Valentine oil and gas fields to identify reservoir compartments and estimate the amount of reservoir compaction due to production. Examination of the pressure data relative to time for wells within various units allows us to identify which wells are in the same reservoir compartments, that is which ones are in hydrologic communication with each other. Figure 4.6 shows an example of the pressure through time for the Valentine field's 9000 ft. sand. Wells that show different pressure gradients during depletion (i.e. Well 208020 in magenta) are interpreted to be in different reservoir compartments and thus not in hydraulic communication with the other wells in the same sands. On the other hand, wells such as 52303 and 59487 shown as blue and yellow dots show the same pressure trend with depletion and are thus interpreted to be in the same reservoir compartment. All of the wells used in the study show pressures that are initially close to hydrostatic and are depleted down to less than a few hundred psi. This major pressure drop may have strong implications for production induced subsidence in the region. Figure 4.7 shows the location of the wells from Figure 4.6 in map view with the colors of the dots representing the same wells as in Figure 4.6. The blue and yellow dots were interpreted as being in the same reservoir compartment based on the pressure data, and looking at them in map view validates this interpretation. The wells are relatively close spatially, and are both on the up-thrown side of the fault running through the area while the other wells are all on the down thrown side. It is commonly accepted that the majority of the faults in the LCZ are sealing faults that compartmentalize reservoirs. The radius of the

idealized reservoir is large enough to encompass all the wells in the same compartment without overlapping any other compartments. For compartments with only one well we center the idealized reservoir on the well by default.
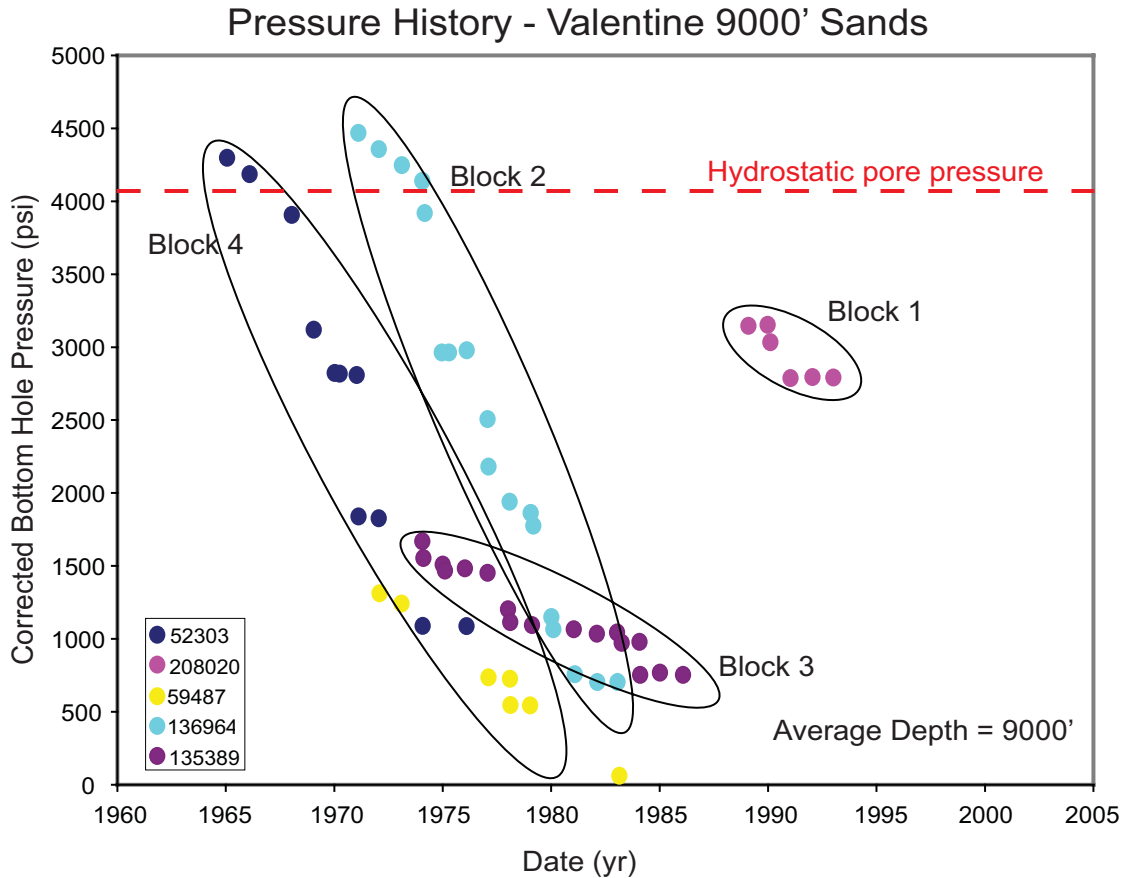
Figure 4.6: Bottom hole pressures in psi for wells in Valentine field's 9000 ft. sand. The blue and yellow dots show the same pressure trend with depletion indicating they are in the same reservoir compartment (or block), whereas the light blue, purple, and magenta dots all show differing pressure trends indicating they are in different reservoir compartments. All of the wells are severely under pressured by the time production ends.

Once we have determined the size of the various reservoir compartments using pressure data and validating the compartments with the map locations of the wells we need to determine the initial thickness of the producing reservoir. We start by using the perforation interval that is reported to the Louisiana Department of Natural Resources during permitting (http://sonris-www.dnr.state.la.us). We then check this against well logs if they are available for the wells we have pressure data for. Figure 4.8 shows a well log for well 136964 in Valentine's 9000 ft sand. In this instance the operator actually

marked the interval where gas was found, but this is quite rare. In some instances the perforation zones reported to the DNR are 100 ft thick or greater. Upon checking the well logs for these intervals it is commonly found that the perforated zone consists of many very small sands (~1-5 ft thick). We use the well log to estimate the actual producing thickness and use this instead of the reported perforation zone for the Geertsma modeling.
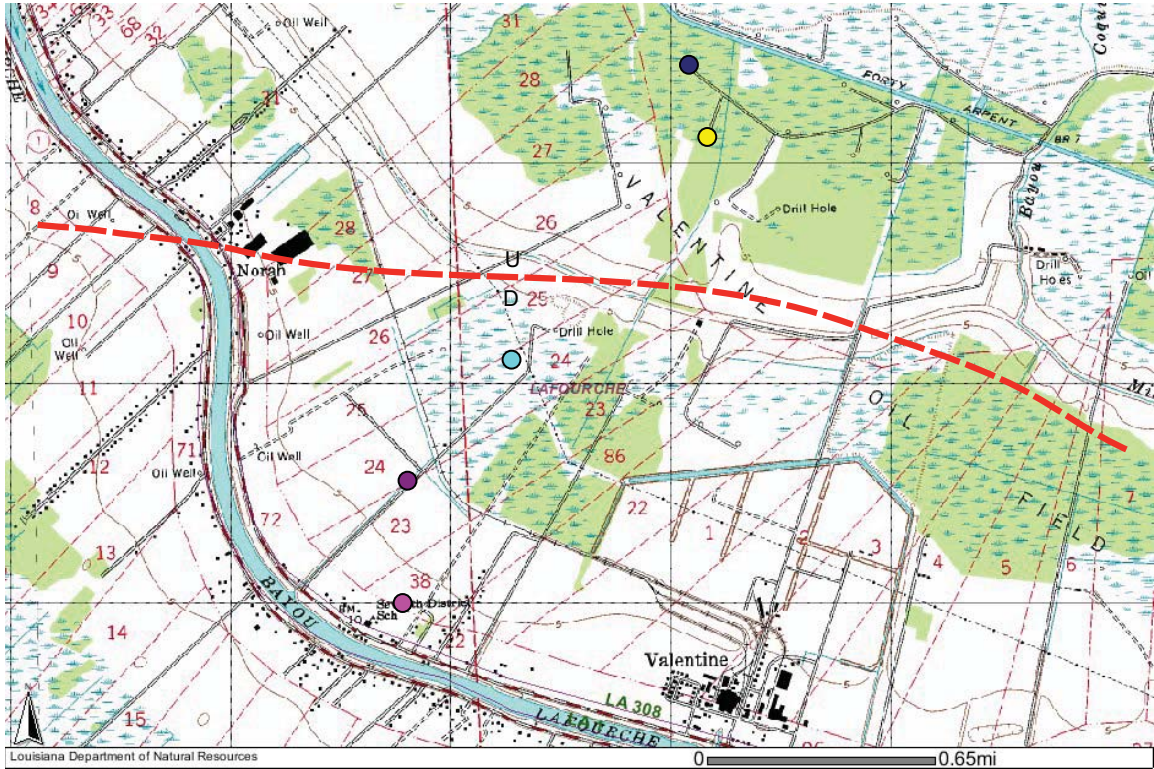
Figure 4.7: Well locations in map view for the wells shown in Figure 4.6. The two wells determined to be in the same reservoir compartment (blue and yellow) are both located on the upthrown side of the fault running through this part of the field (red dashed line with upthrown side marked by a U and the down thrown side marked by a D). All the other wells are on the down thrown side. This validates the conclusions drawn from the pressure data that the blue and yellow wells are in a different pressure compartment than the rest of the wells in the field.

Figure 4.8: Example well log for well number 136864. The operator in this instance marked the gas zone, which is highlighted in pink. Well logs are particularly important in the cases where the perforation zone reported is >100 ft as the operators are generally perforating a very large region to produce from many small sands so the actual producing interval is much smaller than the reported perforation zone.

All four fields began producing between the 1920s and 1940s and produce from intermediate depth (~1800-3700 m or 6000-12000 ft) mid to late-Miocene sands. Production in this area peaked in the 1970s and then declined rapidly. Valentine is the only field directly associated with a salt structure; in this case the reservoirs are all along the flank of an intermediate depth salt dome. The model estimates the surface subsidence signal expected due to the depletion of all the modeled reservoirs over the time period of interest. Figure 4.9 shows the modeled reservoirs in map view which are used in the Geertsma modeling to determine the amount of surface subsidence due to production induced compaction of the reservoirs. The results of this modeling are presented in the next section.

Figure 4.9: Reservoirs used in Geertsma modeling. All the reservoirs are at depths corresponding to their producing sands. The leveling line is shown as white dots with the station in yellow representing the station all the results will be plotted relative to.

4.4 Results

Figure 4.10 shows the results of the Geertsma model for compacting reservoirs in the Leeville, Golden Meadow, Cut Off, and Valentine oil and gas fields for a 50x50 grid in map view for production between 1982 and 1993. Significant subsidence bowls are identifiable over all four fields with maximum predicted subsidence of approximately 10 cm over the 11 year time period. It is notable that despite the depth of the reservoirs (~1800-3700 m or 6000-12000 ft) the signals remain localized over the producing fields.
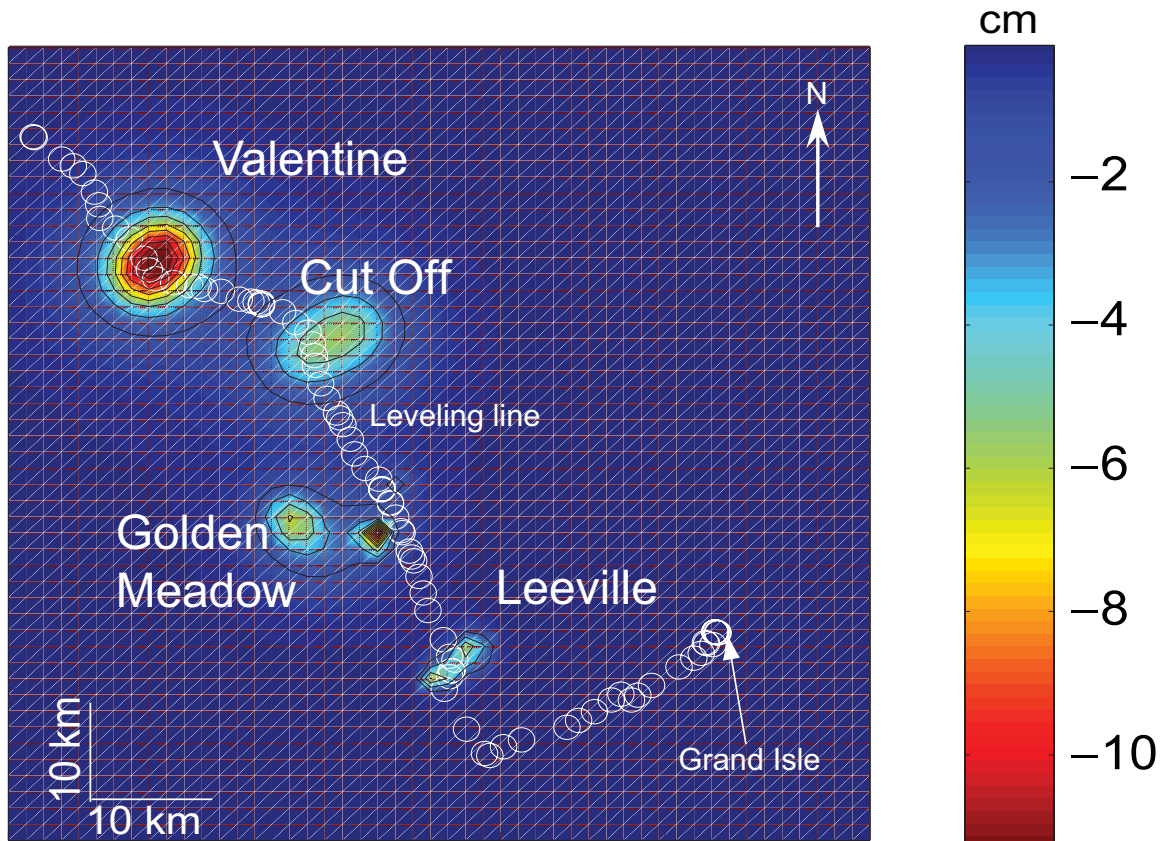
Figure 4.10: Map view of model results. Leveling line is shown as white circles, magnitude of subsidence between 1982-1993 in cm. The subsidence bowls are localized over each of the oil and gas fields and have maximum subsidence of about 10 cm.

In Figure 4.11 we compare the subsidence observed along the leveling line with what is predicted by Geertsma in the same locations. In order to remove some of the regional signal present in the leveling data we show the changes in elevation relative to the station marked by the large square as opposed to Grand Isle. This allows us to identify approximately 5 cm of regional subsidence over the 11 year time period as noted by the dashed line. The model results are shown as the solid line. The model fits the observed subsidence at Leeville and Cut Off within the errors of the leveling data. At Golden Meadow the model greatly under predicts the observed subsidence. This is likely due to only modeling ~50% of the production over the time of interest and most of these reservoirs are located off the transect of the leveling line. At Valentine the model over predicts the observed subsidence which could be due to using the incorrect constitutive law for the reservoir sands. The offset in the modeled Valentine signal is due to the

simplified nature of the reservoirs and the placing of the wells at the center of the reservoir, which is likely not an accurate assumption. Like the results in map view, the profile of the model along the leveling line shows that while depleting oil and gas reservoirs has a measurable effect; it is highly localized over the depleting fields. Even though the constitutive law was developed for an offshore field the location and shape of the subsidence bowls will not change by using a different law, only the magnitudes, and thus will not change our conclusions. There also appears to be little to no effect from the faults transecting the fields, but this will be further examined in future work. Going back to the first motivating questions, we find that in Lafourche Parish the subsidence signal is higher over the oil and gas fields, but it is a highly localized signal, and on the same order of magnitude as the regional subsidence.
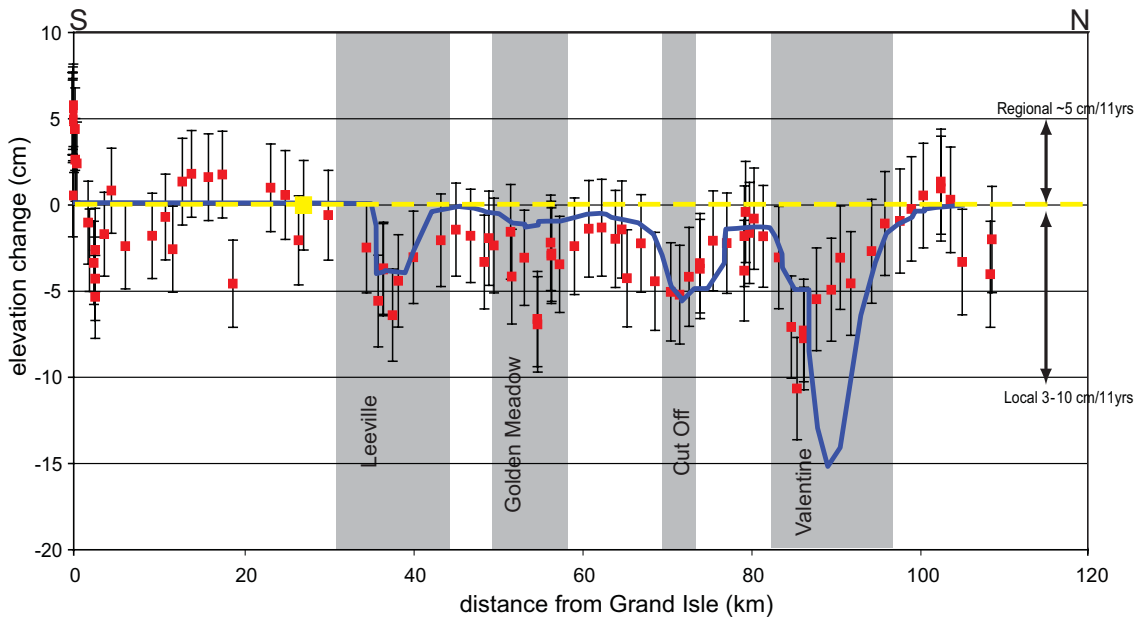
Figure 4.11: Comparison of subsidence model (solid line) to leveling data relative to station marked by the yellow square. Important oil and gas fields are shown in grey boxes. Dashed line indicates the approximate regional subsidence signal observed along the entire line. Compaction of reservoirs in the Leeville, Golden Meadow, Cut Off, and Valentine fields add an additional 3-10 cm of localized subsidence to the regional signal.

To determine if the rate of subsidence correlates with the rate of oil and gas produced we begin by examining the subsidence rates for both epochs of leveling data and compare that to the fluid production rates. Figure 4.12 shows the subsidence rate,
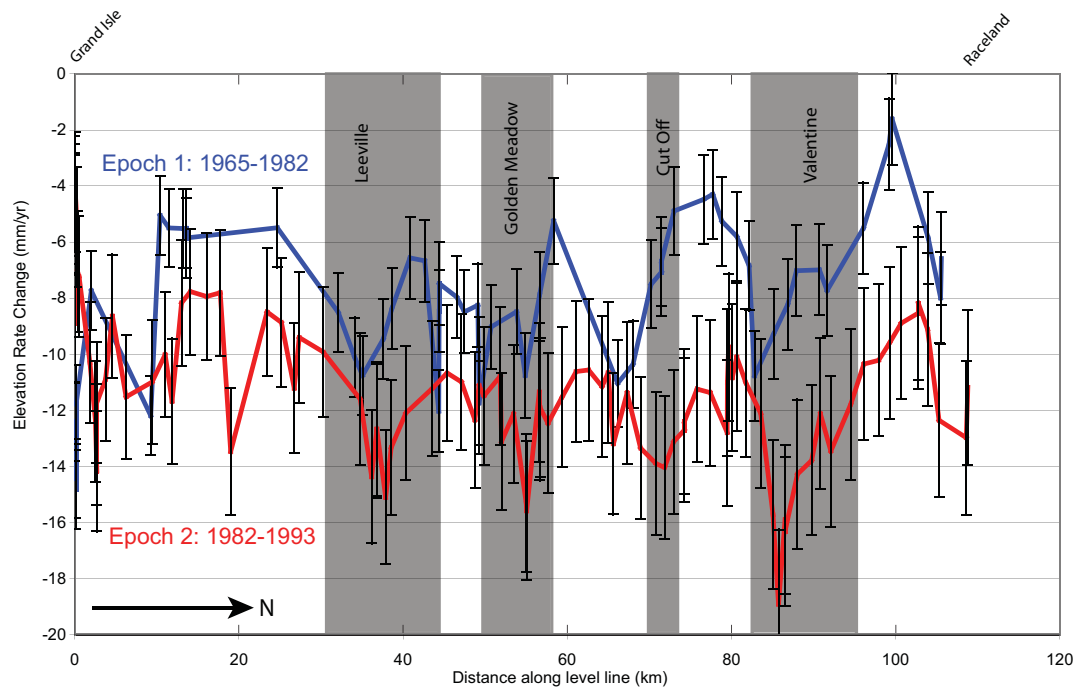
Figure 4.12: Subsidence rate along LA 1 leveling line for two time-epochs: 1965-1982 (blue line) and 1982-1993 (red line). Subsidence rate increases over the entire line in the second time epoch.

in mm/yr, along the LA 1 leveling line for the two leveling epochs of 1965-1982 (blue line) and 1982-1993 (red line). It is apparent that subsidence rates have almost doubled along the entire line in the second time epoch (1982-1993). If the change in subsidence rate was due solely to changes in fluid production it would be expected that the production rate of fluids in the four major fields crossed by the leveling line would also increase in the second time period. However, for all four fields the production of fluids decreased in the second time epoch while the subsidence rate increased as is illustrated in Figure 4.13 for Leeville. This indicates that there may be a time dependent subsidence mechanism that is not being modeled by the simple Geertsma model with an elastic-plastic constitutive law. There are multiple mechanisms that may explain this discrepancy between the production and subsidence rates, including that the reservoirs undergo time-dependent compaction [*Chan, et al.*, 2004], and that the reservoir bounding shales are compacting due to the decrease in reservoir pressure. As the pore pressure decreases in the reservoir due to production the difference in pressure between the reservoir and the

sealing shale increases the effective stress on the shales causing them to dewater over longer time periods. This is the same mechanism as used to explain delayed subsidence following water production observed in California's San Joaquin Basin [*Poland, et al.*, 1975]. In addition, that the subsidence rate is higher everywhere in epoch 2 suggests a regional process as opposed to the local signal expected from oil and gas production.
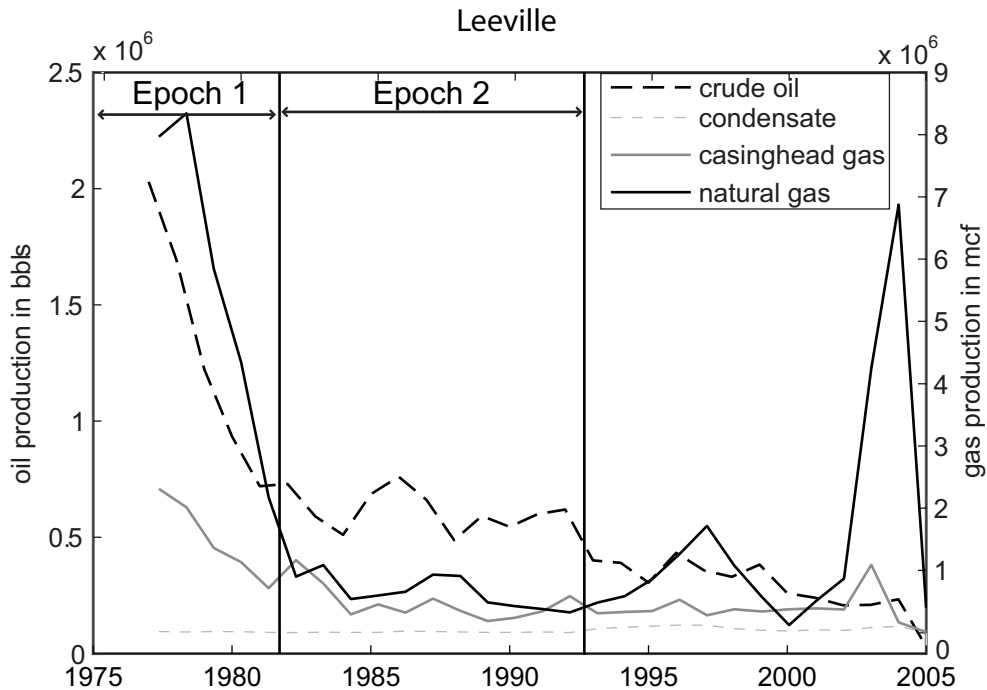
Figure 4.13: Annual fluid production for the Leeville oil and gas field. Production is lower in the second time epoch when subsidence rates are higher indicating that either fluid production is not responsible for the increase in subsidence rate, or there is a time dependent deformation that is not modeled in the simple elastic-plastic Geertsma solution. Similar results are seen for the Golden Meadow, Cut Off, and Valentine fields.

4.5 Discussion

This work is an extension of previous work attempting to identify the mechanisms responsible for subsidence in the LCZ. Most previous studies correlating fluid withdrawal with regional subsidence have been largely qualitative [*Morton, et al.*, 2001; 2002; 2003b; 2003a; 2005b; 2005a; 2006]. Generally these researchers simply compared aerial photographs to identify submerged regions regardless of the mechanism that caused the submergence. Leveling data was only used to show the rate of subsidence and the regions of increased subsidence rate correlate with the oil and gas fields. *Morton et al.* [2006] observed that wells in the Lapeyrouse field showed marked pressure declines to

substantially sub-hydrostatic levels, and that this, along with observations in Texas of regional depressurization from fluid withdrawal, leads them to conclude that depressurization due to hydrocarbon production in the LCZ must also be leading to a regional depressurization. However, examination of bottom hole pressure data from multiple fields in the LCZ by *Chan and Zoback* [2007] and this study show that the producing reservoirs are highly compartmentalized such that depressurization caused by production in one well may not have any effect on the pressures in adjacent or nearby wells. Due to this compartmentalization, more detailed pressure data and modeling needs to be used to determine the role of fluid withdrawal on regional depressurization and subsidence. The generalized Geertsma model shown in Figure 4.5, along with the modeled results in Figures 4.9 and 4.10, indicates that with reservoirs of a finite diameter the surface subsidence due to fluid withdrawal is highly localized, and can't explain the entire regional subsidence signal.

Morton et al. [2006] suggest that since the most rapid period of wetland loss in the LCZ correlates well with the period of highest fluid production, and that as production decreases so will the subsidence such that in the future subsidence due to fluid withdrawal will likely be a decreasing problem. However, they also observe the acceleration of subsidence rate along LA 1 from the 1965-1982 to the 1982-1993 leveling epochs which we have shown is actually a time when the production rates were decreasing. These two points contradict each other, or indicate that another mechanism not addressed by *Morton et al.* [2006] is driving the increased subsidence rate.

In addition to fluid withdrawal driving subsidence, some authors argue for a tectonic component of subsidence in the LCZ [*Gagliano, et al.*, 2003; *Dokka*, 2006]. *Dokka* [2006] specifically argues that some, if not all, of the subsidence signal in the LCZ is due to natural movement along the regional growth faults. *Dokka* chooses a study area near the identified Michoud fault near New Orleans where the lack of oil and gas wells along with the magnitude of subsidence observed indicate that the observed subsidence signal is driven by a large, deep-seated, tectonic component, and that other subsidence mechanisms are inadequate to explain the observed subsidence [2006]. While the Michoud fault may have a strong influence on the local subsidence in *Dokka's* [2006]

study, many other locations in the LCZ either show evidence of production induced faulting [*Chan and Zoback*, 2007] or no strong signal of fault movement (this study). So, while natural movement along regional growth faults is a mechanism that needs to be considered and included in modeling subsidence in the LCZ, the dominating signal is highly spatially varying.

Fluid withdrawal is one of many mechanisms that contribute to subsidence in the LCZ. Other researchers are modeling the effect of compaction of Holocene sediments [*Meckel, et al.*, 2006], lithospheric flexure due to the loading of the Mississippi Delta, and natural movement of the regional growth faults [*Dokka*, 2006]. These studies illustrate that at any given location in the LCZ these different subsidence mechanisms will have varying influences on the local subsidence signal. Thus, one simple model of subsidence will be inadequate to explain the spatial and temporal variability of subsidence in the LCZ. Future work would benefit greatly from lab data for on-shore reservoir samples to constrain the constitutive laws, more and better pressure data including possible pressure recoveries after production has ended, better surface data from either long-term, permanent GPS stations or InSAR, and more detailed finite-element modeling. Any study of wetland loss and its impact on the local ecosystem will benefit greatly from an accurate, spatially variable model that accounts for all important mechanisms of land subsidence, including subsidence related to reservoir compaction and induced fault movement.

4.6 Conclusions

Using bottom hole pressure data, a constitutive law for Gulf of Mexico sands, and a generalized Gulf of Mexico stress path, we modeled the effect of fluid withdrawal in the Leeville, Golden Meadow, Cut Off, and Valentine oil and gas fields had on the regional subsidence between 1982 and 1993. We then compared with observations along the first order leveling line along LA 1 in Lafourche Parish, Louisiana. We find that observations of localized subsidence of ~3-10 cm over the modeled fields between 1982 and 1993 are consistent with what is theoretically expected from reservoir compaction. The amount of localized subsidence over the fields is comparable to the regional signal of

~ 5 cm over the same 11 years. The subsidence due to reservoir compaction is highly localized over the oil and gas fields, whereas regional subsidence is seen everywhere. In this location, induced fault slip will likely contribute only a small amount to the localized subsidence, and the signal is within the error of the leveling data. Compaction due to fluid withdrawal in the Leeville, Golden Meadow, Cut Off, and Valentine fields does have an effect on localized subsidence, but can not account for the entire observed regional subsidence signal. In addition, acceleration of subsidence rates from the 1965-1982 to the 1982-1993 leveling epochs while production rated decreased indicates that there is a time-dependent component due possibly to compaction of shales after production, or another un-modeled regional subsidence signal. In order to accurately model subsidence in the Louisiana Coastal Zone reservoir compaction due to fluid withdrawal must be integrated with other more regional subsidence mechanisms, such as compaction of Holocene sediments and lithospheric flexure, to create an integrated model of subsidence.

Chapter 5

The Role of Shale Compaction due to Hydrocarbon Production on Subsidence in the Louisiana Coastal Zone[4]

Abstract

Coastal wetland loss in southern Louisiana poses a great threat to the region's ecological and economic stability. Wetland loss in the Louisiana Coastal Zone is caused by the interactions of multiple natural and human induced mechanisms, and it has been suggested that compaction of sands due to subsurface oil and gas production may be a large contributing factor. We have modeled the effect of oil and gas production in Lafourche Parish, Louisiana on surface subsidence using a first-order leveling line along highway Louisiana 1 to constrain our model. Using geologic and pressure data, we estimated the amount of compaction in the modeled reservoirs and the resulting surface subsidence. We found that the subsidence predicted from reservoir compaction is consistent with observations of localized subsidence over the same time period. Both modeling and observations show that subsidence due to reservoir compaction is a highly localized signal that is not consistent with observations of regional subsidence. The

---

[4] This work is in preparation for publication

leveling data in our study area covers two time epochs, 1965-1982 and 1982-1993. Over these two epochs the leveling data shows an increasing rate of subsidence from the 1965-1982 to 1982-1993 epoch – a time in which production rates decreased. This indicates the potential for a time-dependent mechanism for production-induced subsidence in the Louisiana Coastal Zone. Using MODFLOW-2000 we model the role that time-dependent compaction of the confining shales has on the regional subsidence signal. We find that MODFLOW is able to adequately capture the observed subsidence during the 1965-1982 and 1982-1993 leveling epochs including the increased subsidence rate during the 1982-1993 epoch that an elastic-plastic model can not. We then extend the model to two additional time epochs after modeled production has ended: 1993-2000 and 2000-2050. We find that subsidence over the oil and gas fields will continue until at least 2050 as the shales compact in response to previous pressure decreases in the reservoir sands. However, the subsidence signal remains localized over the producing fields even over these long time periods indicating the production-induced compaction of the reservoir sands and reservoir bounding shales can not explain the entire observed regional subsidence and land loss in the Louisiana Coastal Zone. This work indicates that production-induced subsidence will remain an important mechanism for land loss on the Louisiana coastal zone for at least the next 50 years and must be considered in regional restoration and protection plans.

5.1 Background

In Louisiana, wetland loss is a combination of land subsidence along with eustatic sea level rise of ~2.29 mm/yr [*Penland, et al.*, 1988] sediment accumulation, erosion, filling and drainage [*Boesch, et al.*, 1994]. Relative sea-level changes result in temporally variable, but spatially constant subsidence patterns along the entire coastal zone [*Suhayda*, 1987; *Penland, et al.*, 1988; *Penland and Ramsey*, 1990; *Roberts, et al.*, 1994]. According to *Penland* [1988; 2000] more than half of the land loss in coastal Louisiana between 1932 and 1990 was related to subsidence. The subsidence is due to natural mechanisms such as compaction of Holocene, Pleistocene, and Tertiary sediments, lithospheric flexure due to the Mississippi delta, and tectonic activity along

the regional growth faults, and the anthropogenic effects of subsurface fluid withdrawal and building of levees and canals in the region. These various mechanisms all produce different temporal and spatial signatures, however, the natural mechanisms of compaction, lithospheric flexure and fault movement suggest a maximum regional subsidence rate of about 3 mm/yr [*Scardina, et al.*, 1981; *Kooi and de Vries*, 1998; *Gagliano, et al.*, 2003]. However, aerial photographs and leveling data in the historical record shows subsidence rates ranging from 9 mm/yr to as high as 23 mm/yr locally; much larger than what was previously expected naturally [*Morton, et al.*, 2002]. Several authors have recently suggested that these high subsidence rates are due to either increased episodic slip along the regional growth faults [*Dokka*, 2006] or hydrocarbon production-induced reservoir compaction and triggered slip along faults [*Sharp and Hill*, 1995; *White and Morton*, 1997; 2001; 2002; 2003b; 2005b; 2005a; *Morton, et al.*, 2006; *Chan and Zoback*, 2007].

Subsidence related to subsurface fluid withdrawal in the Gulf of Mexico region was first recognized along the Texas coast [*Swanson and Thurlow*, 1973; *Neighbors*, 1981]. In the Houston-Galveston area subsidence rates of up to 120 mm/yr greatly exceeded the natural subsidence rates estimated to be up to 13 mm/yr. *Gabrysch and Copland* [1990] found that the rapid subsidence rates and subsidence of up to 3 m was induced by large-scale groundwater withdrawal forming a large subsidence bowl and triggering slip along faults. Subsidence of this magnitude in coastal wetland areas can have a dramatic impact on the ecosystem, as even slight decreases in elevation can lead to frequent flooding which will eventually destroy vegetation and accelerate erosion.

In Louisiana it has been more difficult to link wetland loss to fluid withdrawal as both are pervasive throughout the region and the land loss is likely caused by many interacting processes and conditions. Previously, many authors felt that oil and gas production would only cause local subsidence and be very small due to the depth of production, and thus have little effect on regional wetland loss [*Suhayda*, 1987; *Coleman and Roberts*, 1989; *Boesch, et al.*, 1994]. However, *Morton et al.* [2001] found that periods of rapid wetland loss corresponded to times of high oil and gas production and inferred that the fluid production was driving the wetland loss. Following this

observation *Chan and Zoback* [2007] used numerical and analytical models to estimate surface subsidence due to oil and gas production in the Lapeyrouse field in Terrebonne Parish and the potential for induced slip along the nearby Golden Meadow Fault. *Chan and Zoback* [2007] were able to show that depletion of oil and gas reservoirs in the Lapeyrouse field can have a significant impact on surface subsidence and fault slip locally; however, they were still not able to fully reproduce the observed surface subsidence. This limitation was likely due to the local nature of the study and may be addressed by more regional studies. The findings of *Chan and Zoback* [2007] indicate that subsurface fluid withdrawal is a mechanism that needs to be seriously considered when modeling subsidence in the Louisiana Coastal Zone, and that future modeling should be more regional in order to incorporate it with other subsidence mechanisms and to accurately assess its impact on the regional subsidence picture.

5.2 Study Area and Previous Work

In this chapter we build on the work presented in Chapter 4 using the same study location in Lafourche Parish, Louisiana (Figure 5.1). This region was chosen for multiple reasons. First, this is an area where small amounts of subsidence can have a large impact as the region has elevations between 1 and 5 meters above sea level. In addition, Louisiana Highway 1 is the only hurricane evacuation route for the estimated 80,000 residents in southern Lafourche Parish which includes Port Fourchon, Louisiana's southernmost port, and an important oil and gas port. Much of this road is built on levees within the wetlands or on small areas of land surrounded by wetlands. In addition, there are also numerous wetland restoration projects in this area and more being planned along with increased coastal protection in the wake of Hurricanes Katrina and Rita in 2005 [*Day Jr., et al.*, 2007] making it critical that we understand the mechanisms causing subsidence and wetland loss so that restoration and protection efforts can be carried out effectively. Finally, the first-order leveling line along Louisiana Highway 1 (LA1) that was used to constrain the modeling in Chapter 4 has multiple time epochs providing insight into time-dependent compaction and subsidence processes.

In Chapter 4 we modeled the effect of production-induced reservoir compaction on surface subsidence between 1982 and 1993 over the Leeville, Golden Meadow, Cut Off, and Valentine oil and gas fields. This work found that using an analytical elastic-plastic reservoir compaction model developed by *Geertsma* [1973] accurately explains the localized subsidence bowls present in the leveling data. However, while production-induced reservoir compaction can explain the localized subsidence over the producing fields, it is unable to explain the regional subsidence signal.
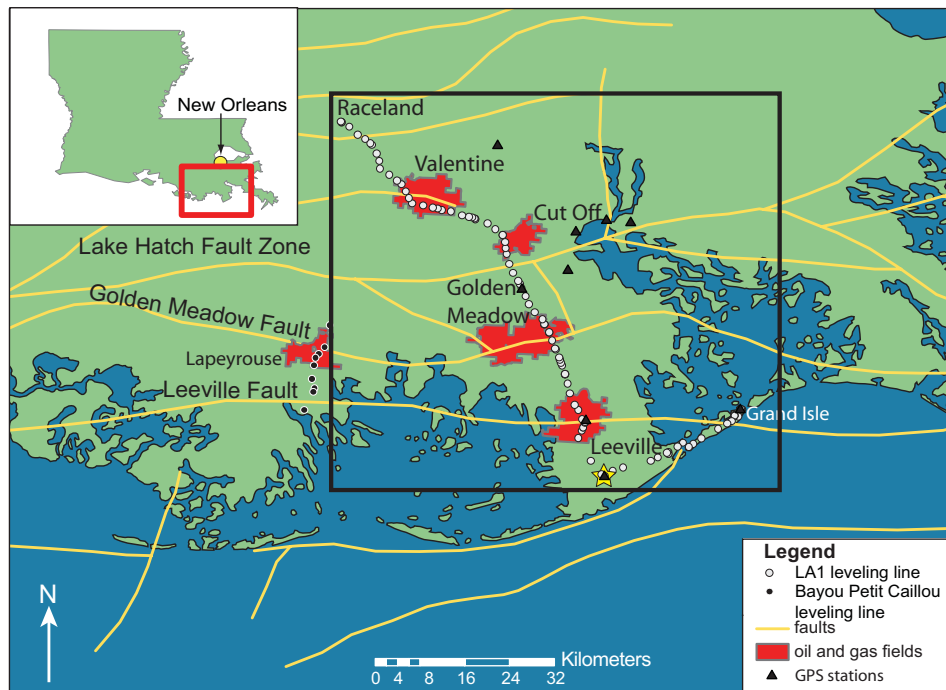
Figure 5.1: Regional map showing the major oil and gas fields of Leeville, Golden Meadow, Cut Off, and Valentine in red, the leveling lines used this study (white circles), the regional faults in gold, and GPS stations as black triangles.

5.3 Time Dependent Shale Compaction

While the analytic *Geertsma* [1973] model for subsidence due to reservoir compaction works well to model the short term subsidence due solely to compaction of the reservoir, one of the advantages of this study area is that the leveling line along highway LA 1 has multiple epochs of data providing insight into potential time dependent mechanisms of subsidence. Figure 5.2 shows the subsidence rates for the first epoch, 1965-1982, in blue and the second epoch, 1982-1993, in red. The subsidence rate

in the second epoch is markedly higher than the subsidence rate in the first epoch. However, if the observed subsidence rate was due solely to the plastic compaction of reservoir sands periods of increased subsidence rate should correlate with periods of increased fluid production. The correlation between wetland loss rates and rates of fluid production in the Louisiana Coastal Zone is what led *Morton et al.* [2001] to hypothesize that the fluid production was driving the wetland loss. However, when production rates from the four fields crossed by the leveling line are compared to the observed subsidence rates we find the exact opposite (except for the Valentine field). Figure 5.3 shows the rates of fluid production for the Leeville, Golden Meadow, Cut Off, and Valentine fields since 1970 (when digital data became available from the Louisiana Department of Natural Resources). In all of the fields production peaked during epoch one (1965-1982) and either decreased markedly (Leeville, Golden Meadow, and Cut Off) or remained about the same (Valentine) during epoch two (1982-1993). That the observed subsidence rate increased while production decreased indicates that either the fluid production is not driving the accelerating subsidence, or that there is a time-dependent subsidence mechanism that is not modeled by the simple elastic-plastic reservoir compaction.
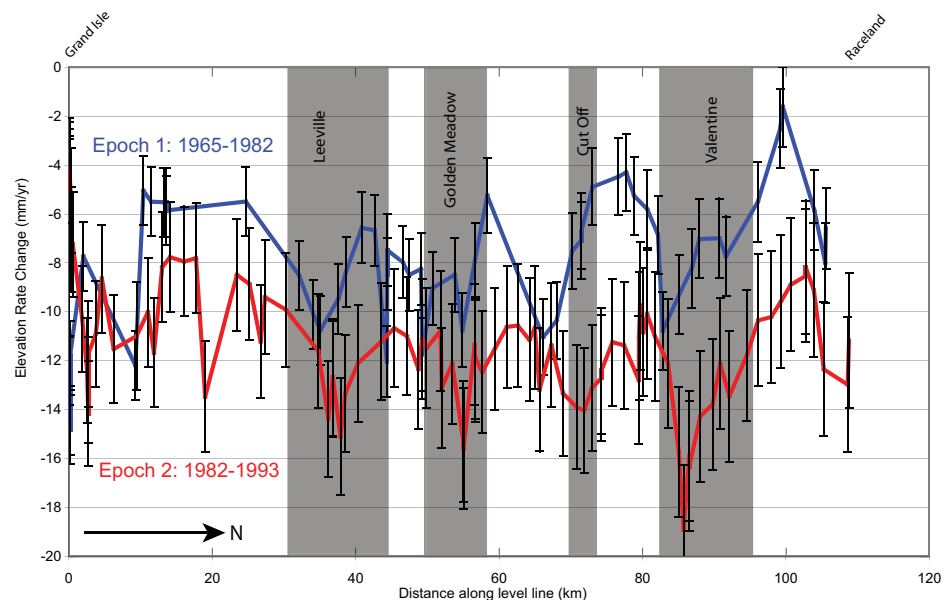
Figure 5.2: Subsidence rates along LA 1 leveling line for two time epochs: 1965-1982 (blue line) and 1982-1993 (red line). Subsidence rate increases over the entire line in the second time epoch.
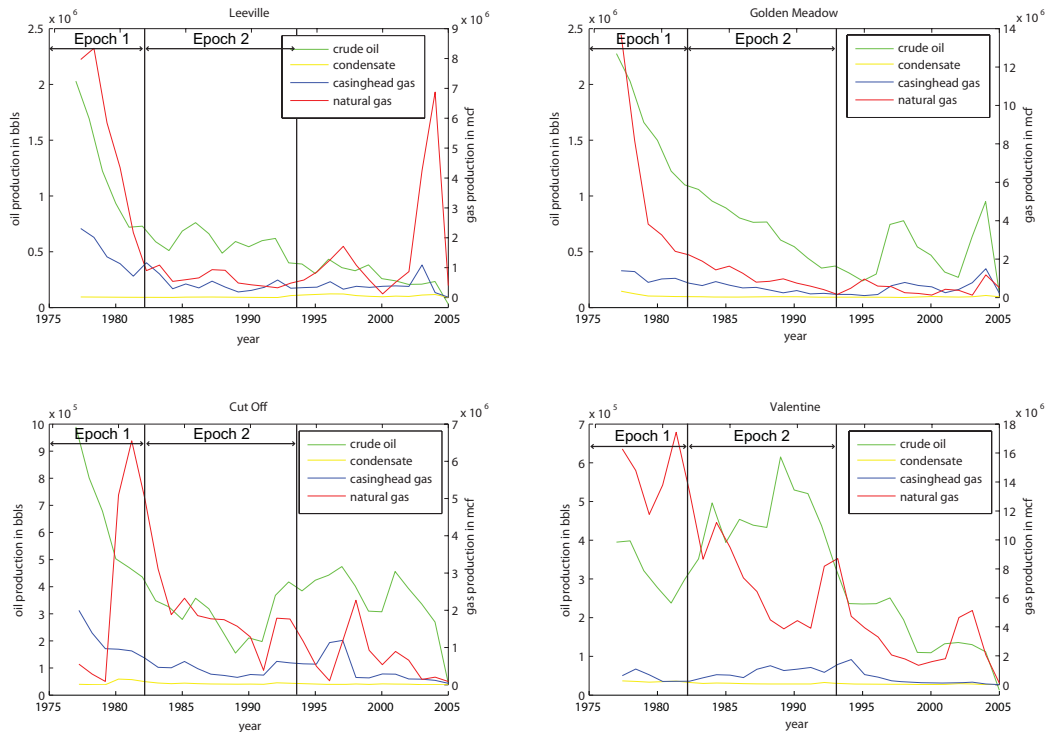
Figure 5.3: Annual fluid production for the major four fields crossed by the LA 1 leveling line. Production is lower in the second time epoch when subsidence rates are higher indicating that either fluid production is not responsible for the increase in subsidence rate, or there is a time dependent deformation due to the fluid production that is not modeled in the simple elastic-plastic Geertsma solution.

Subsidence that continued or increased following the maximum fluid production was also observed in California's San Joaquin Valley where between 1925 and 1977 there was more than 9m of subsidence due to ground water production. In California much of the subsidence happened after ground water production was limited or stopped. This led researchers to look to a time-dependent mechanism as an explanation. It was determined that the continued subsidence in the San Joaquin Valley was due to compaction of the aquifer bounding shales. High permeability reservoirs are frequently bounded above and below by low permeability confining units such as shales. As fluids are being produced from the high permeability aquifers the pore pressure drops throughout the reservoir due to the ease with which fluids flow through the pore space. In a poorly or unconsolidated aquifer, similar to those in the San Joaquin Valley and the Louisiana Coastal Zone, this drop in pressure leads to almost instantaneous plastic compaction of the reservoir sands. This compaction and resulting subsidence is what is modeled by the Geertsma analytical model. However, even as the pore pressure drops in

the reservoir, the low permeability of the confining units inhibits the movement of fluids on the same time scales as seen in the reservoirs. This causes a large pressure differential to build up between the reservoir and the confining unit and an increase in the effective stress acting on the confining unit. Over time periods of months to years the fluids in the confining unit will begin to flow towards the lower pressure reservoir in an attempt to equilibrate the pressures throughout the system. As fluids move out of the shales they will begin to compact and contribute to the subsidence observed at the surface. In addition, as the unconsolidated sands of the reservoir deformed plastically due to production-induced pressure declines they will not recover any of the lost porosity from compaction. This mechanism of time-delayed subsidence due to compaction of reservoir bounding shales is represented schematically in Figure 5.4.
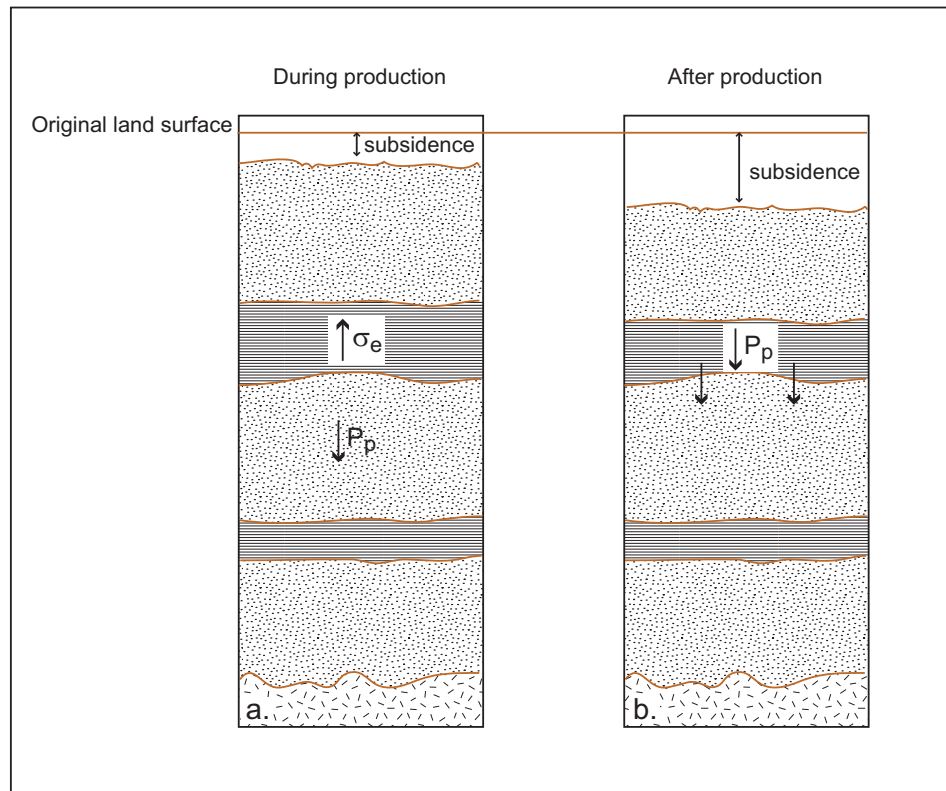
Figure 5.4: Schematic representation of the effect of fluid production from an unconsolidated reservoir bounded by confining shales and the resulting subsidence. a. As fluid is produced from the reservoir the pore pressure (P_p) decreases and thus increases the effective stress (σ_e) on the confining unit. During this time there is also subsidence observed during production. b. After production ends fluids begin to flow out of the low permeability confining unit to equilibrate the pressure differential due to earlier production. This flow of fluids leads to compaction of the reservoir bounding shales and continued subsidence even though production has ended.

As we have determined that time-dependent compaction of the reservoir bounding shales may play an important role in the subsidence signal in the Louisiana Coastal Zone we need to re-address the constitutive parameters used in our previous Geertsma model. During the first modeled time epoch, 1965-1982, we can assume that the subsidence signal will be dominated by the elastic-plastic compaction of the reservoir sands. Thus, the Geertsma model should be able to model most of the observed subsidence. We modify the constitutive law that was used in our previous work (detailed in Chapter 4) [*Mallman and Zoback*, 2007b] such that the modeled subsidence fits the observed subsidence along the leveling line. The results of this revised constitutive law are shown in Figure 5.5. We then use this same constitutive law to model the subsidence due to compaction of the reservoir sands during the 1982-1993 time epoch (Figure 5.6). When using constitutive parameters that fit the first epoch of leveling data, when the subsidence signal should be dominated by the sand compaction, we under predict the subsidence observed in the second time epoch when both sand compaction and time-dependent shale compaction are likely contributing to the subsidence signal. This indicates that the constitutive parameters that were used by *Chan and Zoback* [2007] and in our previous work [*Mallman and Zoback*, 2007b] were likely too compliant for the onshore sediments and thus over estimated the production induced sand compaction and resulting subsidence. In the rest of this paper we will examine whether including time-dependent shale compaction can fit both the 1965-1982 and 1982-1993 subsidence observations and explain the observed acceleration in the subsidence rate in the second time epoch despite a decrease in the production over the same time period.
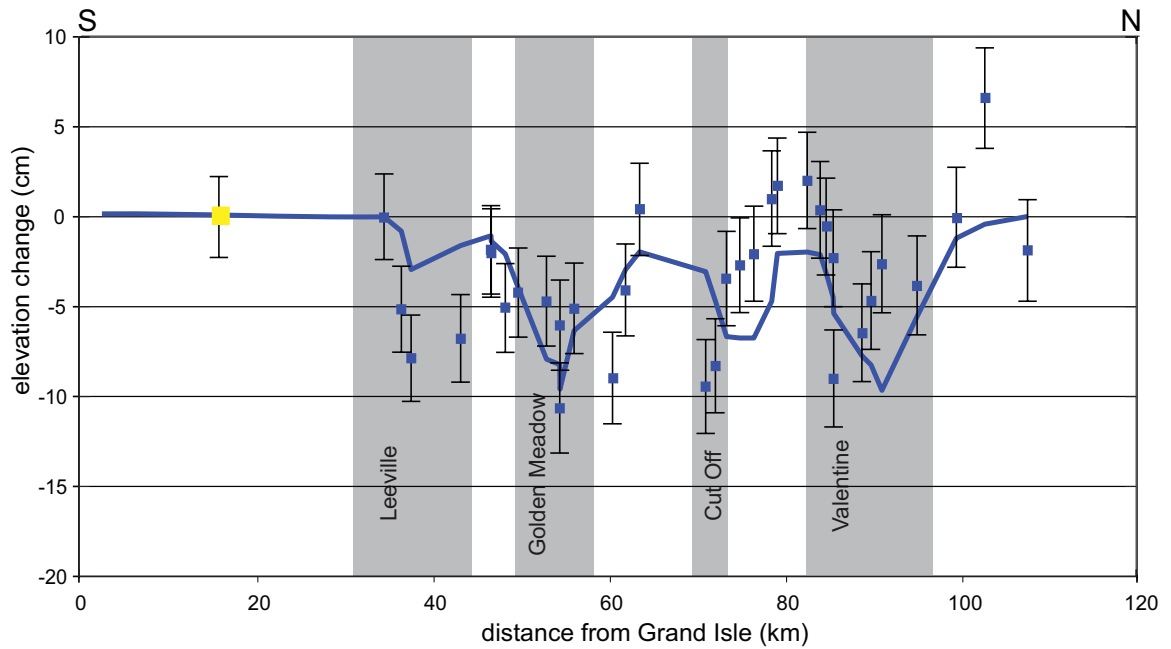
Figure 5.5: Model results using Geertsma for the 1965-1982 leveling epoch with new constitutive parameters meant to fit this subsidence data.
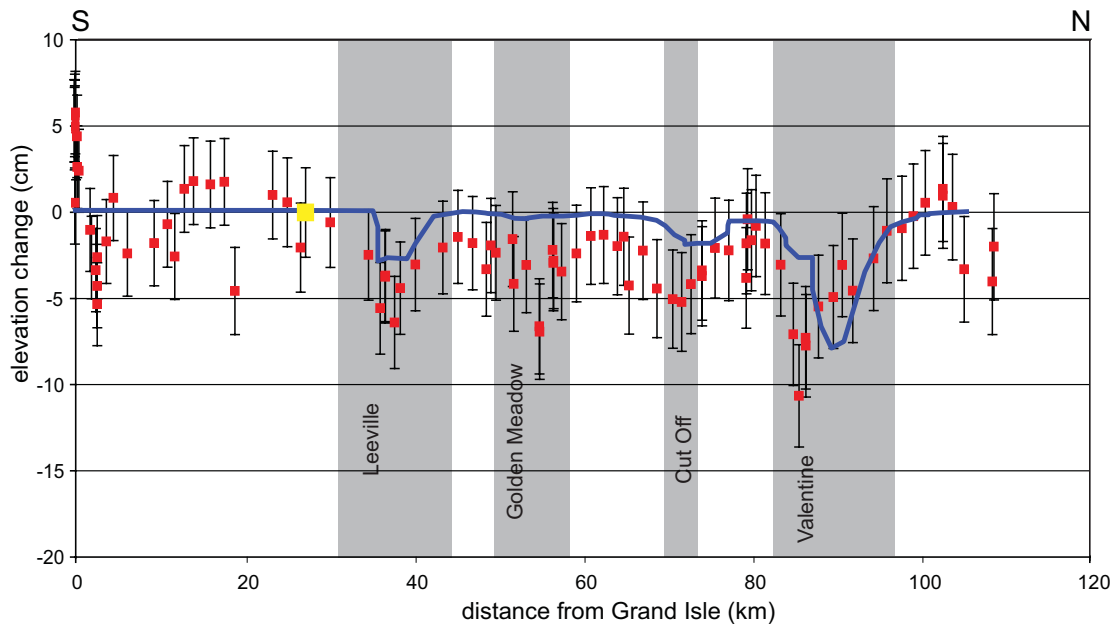
Figure 5.6: New model results for 1982-1993 leveling epoch using the same constitutive parameters as in figure 5.5. The model now under predicts the observed subsidence since the Geertsma modeling can only model compaction of the reservoir sands and not time-dependent compaction of the reservoir bounding shales.

5.4 Modeling Shale Compaction and Subsidence

We model the time-dependent shale compaction and resulting subsidence using the finite difference groundwater flow program MODFLOW-2000 developed by the Unites States Geological Survey. MODFLOW-2000 in conjunction with the subsidence package (SUB) [*Höffmann, et al.*, 2003] simulates the drainage, changes in ground-water storage, compaction of aquifers, interbeds, and confining units and the resulting surface subsidence. The subsidence package couples the sediment compaction and changes in pressure based on the Terzaghi principle of effective stress in one dimension:

$$\sigma'_{zz} = \sigma_{zz} - p \qquad (5.1)$$

where σ'_{zz} is the vertical component of the effective stress tensor, σ_{zz} is the vertical component of the total stress tensor, and p is the pore fluid pressure. However, in hydrology one generally expresses pore fluid pressures in terms of head, thus substituting p in Equation 5.1 with:

$$h = \frac{p}{\rho_w g} + h_e \qquad (5.2)$$

where h is the total hydraulic head, ρ_w is the density of water (or the pore fluids), g is the gravitational acceleration, and h_e is the elevation head for an arbitrary datum. Thus for a confined aquifer the change in effective stress for a given change in head (or pressure) is:

$$\Delta\sigma'_{zz} = -\rho_w g \Delta h \qquad (5.3)$$

If the change in effect stress is due only to a change in pore pressure we can express the change in thickness of a control volume with initial thickness b as:

$$\frac{db}{dh} = \rho_w g \overline{\alpha} b = S_{sk} b = S_k \qquad (5.4)$$

S_k is the skeletal storage coefficient, S_{sk} is the skeletal specific storage, and $\overline{\alpha}$ is the one dimensional compressibility. MODFLOW-2000 is then essentially solving Darcy's Law in 3D:

$$\frac{\partial}{\partial x}\left(K_{xx}\frac{\partial h}{\partial x}\right)+\frac{\partial}{\partial y}\left(K_{yy}\frac{\partial h}{\partial y}\right)+\frac{\partial}{\partial z}\left(K_{zz}\frac{\partial h}{\partial z}\right)-W = S_s\frac{\partial h}{\partial t} \qquad (5.5)$$

Where K is the component of the hydraulic conductivity tensor in the given direction, W is the volumetric flux per unit volume of sources and/or sinks, and S_s is the specific storage. The depletion is incorporated into the volumetric flux (W) term and subsidence into the right hand side of the equation.

There are a number of advantages to using MODFLOW-2000 and the subsidence package to model shale compaction and the resulting subsidence. First, it should be possible to invert for the constitutive law parameters using observed subsidence and either pore pressure changes or well flow rates. In addition, at well locations where pressure changes are available, it is possible to perform a history match with flow rates to determine permeability of the reservoir thus permitting the inclusion of wells where only production data is known, and not pressure changes, into the modeling. And finally, it allows for the inclusion of both elastic-plastic deformation in the sands and the time-dependent deformation of the shales when modeling the drainage-induced surface subsidence. However, there are some limitations with using MODFLOW as there are with any modeling program. First, MODFLOW only considers one-dimensional consolidation and subsidence; that is it ignores horizontal strains and stresses. Since the only surface observations used in this work are from leveling data, we would have no constraints on any modeled horizontal strains and stresses if they were calculated. Thus, the vertical consolidation and subsidence modeled by MODFLOW is sufficient for our constraints. MODFLOW also does not use any stress or strain tensors, but only hydraulic head (pore pressure). To simplify the math MODFLOW converts the constitutive law into a two state linear elastic/plastic law, and does not include dry frame viscoplasticity. And finally, unknowns about the constitutive law are replaced in MODFLOW with unknowns about specific storage.

5.4.1 *Building the MODFLOW model*

Using the reservoirs identified in the Leeville, Golden Meadow, Cut Off, and Valentine fields from previous work and the well logs we built a generalized geologic

model for the MODFLOW subsidence modeling. The depth and thickness of the sand units was determined using the pressure data and well logs as in the Geertsma modeling. Unlike the Geertsma modeling which placed the reservoirs in a uniform elastic half-space, MODFLOW uses a layered approach. Due to the layered model needed by MODFLOW each of the sand units was assumed to be laterally continuous over the entire model. To account for the reservoir compartments and faults we bound the edge of each modeled reservoir with a horizontal flow boundary which prohibits lateral flow of fluids. One other problem encountered during the building of the MODFLOW model was that MODFLOW does not allow for overlapping reservoirs. In Geertsma the reservoirs modeled during the two time epochs occasionally overlapped, but since they were run separately this was not a problem. However, as there is only one MODFLOW model built for the entire time period (1965-2050) with different stress periods defining the various time epochs overlapping reservoirs became a problem. To remedy this we made minor changes to the size of some of the reservoirs in MODFLOW to remove the overlapping problems. There was one instance where a reservoir modeled in Geertsma was simply removed for the MODFLOW modeling. The effect of this is obvious in the miss-match between the model results for the 1965-1982 time epoch over the Cut Off field. Once the sand layers were determined the remainder of the section was filled in with shale layers.

While the MODFLOW model is a generalized model of the actual stratigraphy of the Louisiana Coastal Zone, it is representative of the shale dominated section seen in the well logs. In addition, missing non-producing sand layers will likely not have a large effect on the results of the model due to the very low hydraulic conductivity of the shale layers which limits the zone of influence of the depleting reservoirs to a relatively small area above and below the reservoirs relative to the thickness of the shales. Finally, even if we have missed smaller, inter-bedded sand units the entire model ends up working as an effective medium, and thus, this is compensated for by small variations in the constitutive law parameters. In addition, we do not place any horizontal flow barriers in the shale layers. There are multiple reasons for this. First, while it is known that there are many faults in this region which do compartmentalize the sands it is unclear what the exact throw is along these faults. Since the faults are primarily growth faults, their throw

varies along dip with the deeper portions having significantly higher throw and the shallower portions. Without good seismic data over the study area we have no way of knowing how the throw varies over depths and if it is enough to compartmentalize the shales similarly to the sands. By allowing the shales to be in communication laterally over the entire region the subsidence due to the shale compaction that is modeled will be a worst case scenario as it will allow for the shales to dewater over a larger area then if they were compartmentalized. Second, the actual strike and dip of the regional and sub-regional faults is also unknown, so it isn't clear where exactly the faults would even compartmentalize the shales. Due to the lack of detailed knowledge of the fault structure we chose to take the simplest and thus worst case scenario in our modeling so as not to underestimate the role of shale compaction on the regional subsidence signal. The production-induced subsidence modeled by MODFLOW is generating an upper bound on the subsidence due to shale compaction as a result of the laterally extensive nature of the modeled shales. And while the production-induced sand compaction can be seen as a lower bound due to our inability to model all production in the fields, much of this variation is accounted for through modifications of the constitutive parameters to fit the observed subsidence in the leveling data.

5.4.2 *MODFLOW Parameters*

MODFLOW was originally developed as a groundwater flow modeling package, and thus the parameters that it requires are those frequently used in hydrogeology as opposed to those used in rock deformation. In the Geertsma modeling (described in Chapter 4) we needed the pore pressure of the reservoir through time and to determine the compaction in the reservoir due to the change in pore pressure we use a constitutive law and stress path for Gulf of Mexico sands. MODFLOW on the other hand requires head observations for the sand layers, hydraulic conductivities, specific yield and specific storage for all modeled layers.

Many of the parameters used by MODFLOW are directly analogous to those used in the Geertsma modeling. Head can be computed directly from pore pressure observations relative to a datum:

$$h = \frac{p}{\rho_w g} + h_e$$

(5.6)

where h is the hydraulic head, p is the pore pressure, ρ_w is the density of water, g is the acceleration due to gravity and h_e is the elevation head relative to an arbitrary datum. Since the study area has very little topography and is at approximately sea level we use sea level as our datum, thus $h_e = 0$.

Hydraulic conductivities, K, are related to the porosity of the material, but are functions of not only the porous medium, but also the fluid, whereas permeability is a function only of the porous medium. Since we have no information on the permeabilities or hydraulic conductivities of the sands and shales in the region we will use published ranges of values for unconsolidated sands and shales [*Freeze and Cherry,* 1979]. The values of published hydraulic conductivities range between 0.3 - 3000 ft/day (10^{-6} - 10^{-2} m/day) for unconsolidated sand and $3e^{-4}$ – 3 ft/day (10^{-9} - 10^{-5} m/day) for unconsolidated shale. Published hydraulic conductivities are generally only horizontal conductivities, K_x, or are an average conductivity for the entire medium. Because much of our section is shale we know that there should be a significant difference between the horizontal and vertical hydraulic conductivities. Thus, in addition to testing various published hydraulic conductivities we also tested varying ratios of horizontal (K_x) and vertical (K_z) hydraulic conductivities (K_x/K_z). These ratios varied between 3/1 and 10/1 for the sands (that is the horizontal hydraulic conductivity was 3 times as great as the vertical hydraulic conductivity in the 3/1 case) and 30/1 to 100/1 for the shales.

Specific yield is defined as the volume of fluid that is capable of draining from a saturated area as a result of the force of gravity [*Fetter,* 2001]. The value of specific yield is related to grain size. The more fine grained the sediments, the more surface area there is for the fluids to cling to, and thus the lower the specific yield of the material. Again, we have no information on the true values of specific yield of the sediments in out

study area so we use published ranges of values from *Domenico* [1972] and *Gabrysch* [1982] of 15-32% for sand and 3-19% for shale.

The specific storage of a reservoir is defined as the volume of fluid that a unit volume of reservoir will release from storage under a unit decline in hydraulic head [*Freeze and Cherry*, 1979]. The specific storage, S_s, is:

$$S_s = \rho_w g (\alpha + \eta \beta)$$
(5.7)

where ρ_w is the density of water, g is the acceleration due to gravity, α is the compressibility of the aquifer skeleton, η is the porosity and β is the compressibility of water. To determine the skeletal specific storage, S_k, we can drop the porosity and compressibility of water to leave:

$$S_k = \rho_w g \alpha$$
(5.8)

We can use the published ranges of specific storage values of $1.3e^{-4} - 1e^{-3}$ for sand and $1.3e^{-3} - 1e^{-2}$ for shale [*Freeze and Cherry*, 1979]. Alternatively, we can use the sand compressibility from the previous Geertsma modeling to determine the specific storage of the sands in the MODFLOW modeling which gives a sand specific storage of $1.4e^{-1}$. We test both of these methods for determining specific storage. Table 5.1 shows the values for hydraulic conductivity, specific yield, and specific storage used to test the model sensitivity to each of the parameters.

Name	Sand					Shale			
	K_x ft/day	K_z ft/day	Specific Yield	Specific Storage		K_x ft/day	K_z ft/day	Specific Yield	Specific Storage
Dutton et al., 2003 values	6.2	1.30E-03	0.26	3.00E-06		9.00E-01	3.50E-05	2.00E-03	2.30E-04
Hydraulic Conductivity anisotropy sands: 10/1 shales: 100/1 Freeze and Cherry, 1979	3000	300	0.32	1.00E-03		3	0.03	0.19	2.00E-02
Hydraulic Conductivity anisotropy sands: 3/1 shales: 30/1 Freeze and Cherry, 1979	3000	900	0.32	1.00E-03		3	0.09	0.19	2.00E-02
High perm sand, high perm unconsolidated shale	3000	300	0.32	1.00E-03		3	0.03	0.19	2.00E-02
Low perm sand, high perm unconsolidated shale	0.3	0.03	0.32	1.00E-03		3	0.03	0.19	2.00E-02
High perm sand, low perm unconsolidated shale	3000	300	0.32	1.00E-03		3.00E-04	3.00E-06	0.19	2.00E-02
High perm sand, high perm consolidated shale	3000	300	0.32	1.00E-03		3.00E-04	3.00E-06	5.00E-02	2.00E-02
High perm sand, low perm consolidated shale	3000	300	0.32	1.00E-03		3.00E-08	3.00E-10	5.00E-02	2.00E-02
Effect of Specific Yield, Johnson 1967 High Sy	3000	300	0.32	1.00E-03		3	0.03	0.19	2.00E-02
Effect of Specific Yield, Johnson 1967 Low Sy	3000	300	0.15	1.00E-03		3	0.03	0.03	2.00E-02
Effect of Specific Yield, Gabrysch, 1982	3000	300	0.15	1.00E-03		3	0.03	0.006	2.00E-02
Effect of Specific Storage, Domenico, 1972 High Ss	3000	300	0.32	1.00E-03		3	0.03	0.19	2.00E-02
Effect of Specific Storage, Domenico, 1972 Low Ss	3000	300	0.32	1.30E-04		3	0.03	0.19	1.30E-03
Effect of Specific Storage, Fit to Geertsma	3000	300	0.32	1.40E-01		3	0.03	0.19	2.00E-02

Table 5.1: MODFLOW parameters used for sensitivity analyses.

5.5 Model Sensitivity

Due to our lack of knowledge of the reservoir parameters used by MODFLOW in the modeled region we carried out various sensitivity analyses of the parameters to provide some constraints on the model results. For published parameter ranges we tested the upper and lower limits to provide upper and lower bounds on the effect of the parameter. In addition to the published ranges for the parameters we also tested values that were published for the same or similar units in the Gulf Coast.

The first parameter we tested was the ratio of horizontal and vertical hydraulic (K_x/K_z) conductivities for high permeability unconsolidated sand and shale. In addition to the values published in *Freeze and Cherry* [1979] we also tested values for the Wilcox unit, a mid-Miocene sand and shale aquifer sequence in onshore Texas published by *Dutton et al.* [2003]. Figure 5.7 shows the effect of varying the K_x/K_z ratio for the first time epoch (1965-1982). The blue line represents the values published by *Dutton et al.* [2003], the magenta and green lines represent the values published by *Freeze and Cherry* [1979]. The magenta line assumes a 10/1 K_x/K_z ratio for the sands (that is, the horizontal conductivity is 10 times as great as the vertical conductivity) and a 100/1 K_x/K_z ratio for the unconsolidated shales. The green line assumes a 3/1 K_x/K_z ratio for the sands and a

30/1 K_x/K_z ratio for the unconsolidated shales. The values reported by *Dutton* [2003] significantly under predict the observed subsidence for this time epoch. This is not surprising however because the Wilcox unit in Texas is fairly well consolidated and cemented, which will lower the hydraulic conductivity compared to the unconsolidated sediments that are common throughout the Miocene section in onshore Louisiana. The magenta line with the 10/1 for sand and 100/1 for shale ratios of K_x/K_z fits the observed subsidence fairly well while the green line with the 3/1 for sand and 30/1 for shale ratios of K_x/K_z greatly over predicts the observed subsidence.

Figure 5.7: Effect of Kx/Kz ratio on modeled subsidence for 1965-1982 leveling epoch. The leveling data are shown as blue squares with associated error bars and the model results shown as blue, magenta, and green lines.

Figure 5.8 shows the same three sets of values for the second time epoch (1982-1993), which is a time when shale compaction is likely to become important. Again the blue Dutton line greatly under predicts the observed subsidence and the green 3/1 and 30/1 K_x/K_z ratio greatly over predicts the observed subsidence. The magenta 10/1 and

100/1 K_x/K_z ratio fits the observed subsidence fairly well with only slight under predictions at Leeville and over predictions at Valentine. During the first time epoch we were unable to model the observed subsidence over the Cut Off field. This was due to the one reservoir that was removed for the MODFLOW modeling that was used in the Geertsma modeling. Thus, the reservoir that is likely driving the observed subsidence was not modeled. However, since we were able to accurately model the observed subsidence over Cut Off in the second time epoch the mis-modeling in the first time epoch may not have a large impact on the long term modeling and subsidence predictions. Since the 10/1 K_x/K_z ratio for the sands and the 100/1 K_x/K_z ratio for the unconsolidated shales fits the observed subsidence data well for both the 1965-1982 and 1982-1993 time epochs all future sensitivity analyses will use this ratio for the hydraulic conductivities.
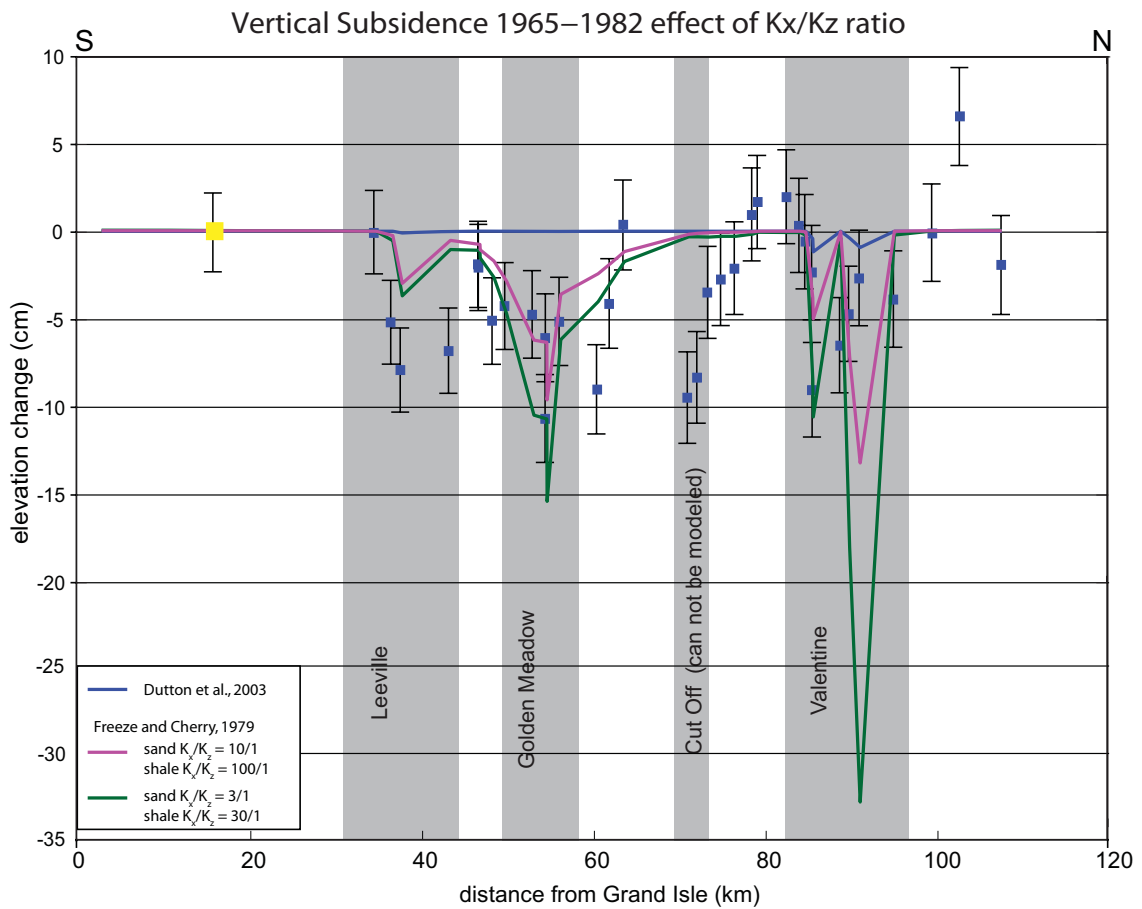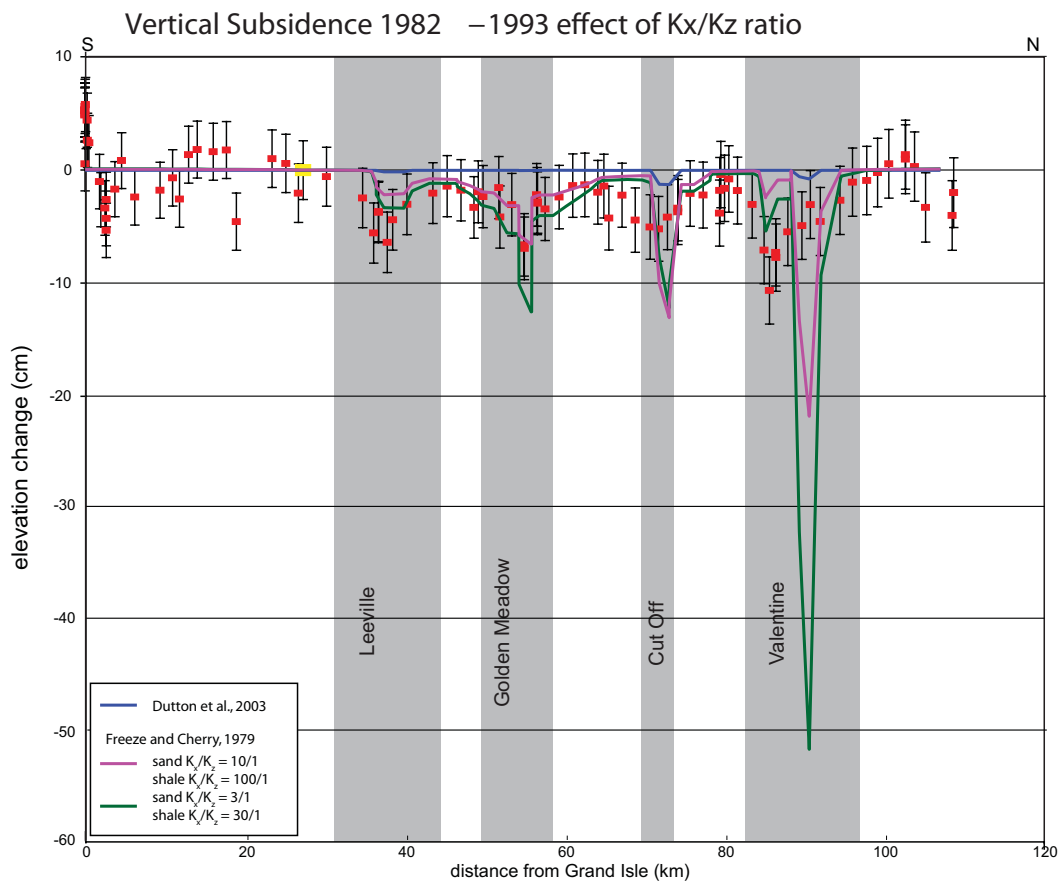

Figure 5.8: Effect of Kx/Kz ratio on modeled subsidence for 1982-1993 leveling epoch. The leveling data are shown as red squares with associated error bars and the model results shown as blue, magenta, and green lines.

Once we had an idea of the ratio of horizontal to vertical hydraulic conductivities we tested the effect of varying the values of hydraulic conductivity of the sands. We tested the upper and lower bounds of unconsolidated sand conductivities reported by *Freeze and Cherry* [1979]. The effect of high sand conductivities (blue line) and low sand conductivities (green line) on the MODFLOW subsidence modeling for the two time epochs is shown in Figures 5.9 and 5.10. The high sand hydraulic conductivity used is 3000 ft/day for the horizontal conductivity and 300 ft/day for the vertical conductivity. The low sand hydraulic conductivity used is 0.3 ft/day for the horizontal conductivity and 0.03 ft/day for the vertical conductivity. The models using low hydraulic conductivities for the sand predict very little subsidence due to reservoir compaction and greatly under estimate the observed subsidence while the models using high hydraulic conductivities match the observed subsidence quite well. This indicates that the unconsolidated sands in the modeled region of onshore Louisiana have fairly high hydraulic conductivities, and thus high permeabilities. This is not surprising because this area has been producing oil and gas since the early 1900s indicating that the reservoirs here produce well without any artificial stimulation that is used to overcome low permeability reservoirs today.
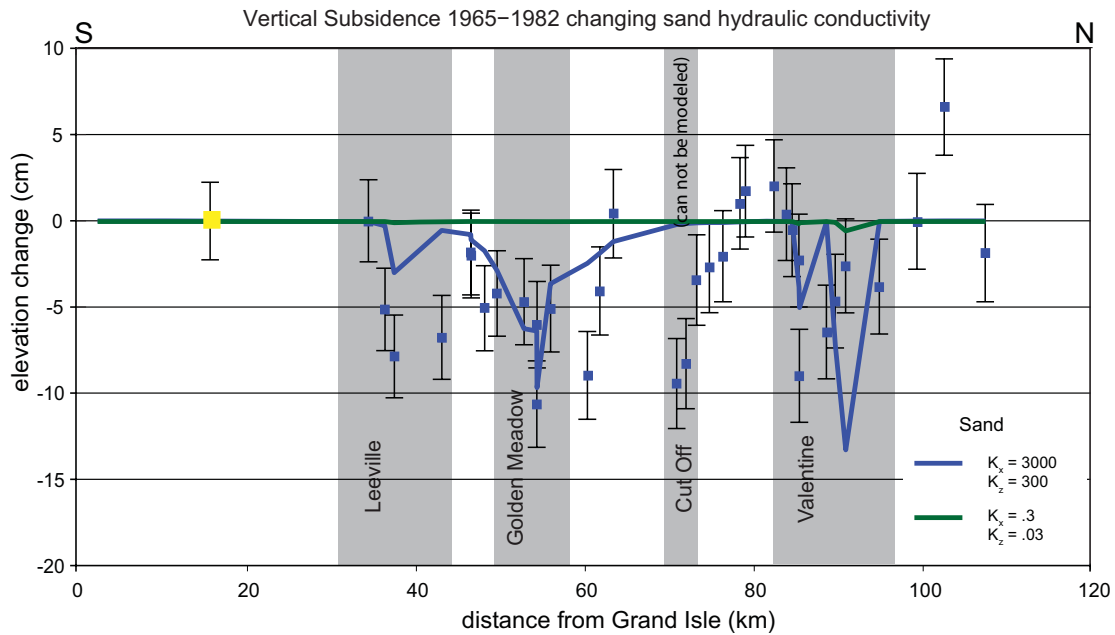

Figure 5.9: Effect of varying the hydraulic conductivity of the reservoir sands for 1965-1982 leveling epoch.
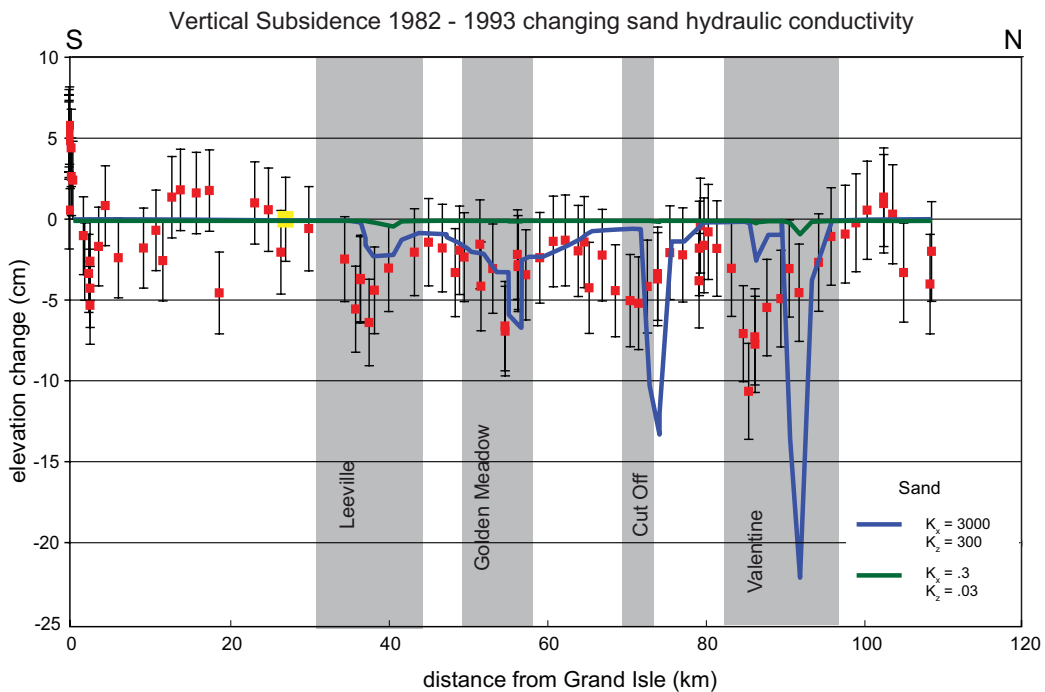
Figure 5.10: Effect of varying the hydraulic conductivity of the reservoir sands for 1982-1993 leveling epoch.

We next tested the effect of varying hydraulic conductivities of the confining units in the model. The confining units are frequently referred to as shales in the literature, but since the sand units are known to be unconsolidated it is unlikely that the confining units have been consolidated. To test this we looked at hydraulic conductivities for both high (blue line) and low (green line) conductivity unconsolidated shales as well as high (magenta line) and low (black line) conductivity consolidated shales. The results for varying the hydraulic conductivities for the confining units in both the 1965-1982 and 1982-1993 time epochs are presented in Figures 5.11 and 5.12. Again, in both cases the high hydraulic conductivities for unconsolidated shales fits the observed subsidence data the best with low hydraulic conductivity unconsolidated shales and all consolidated shales greatly under predicting the observed subsidence.
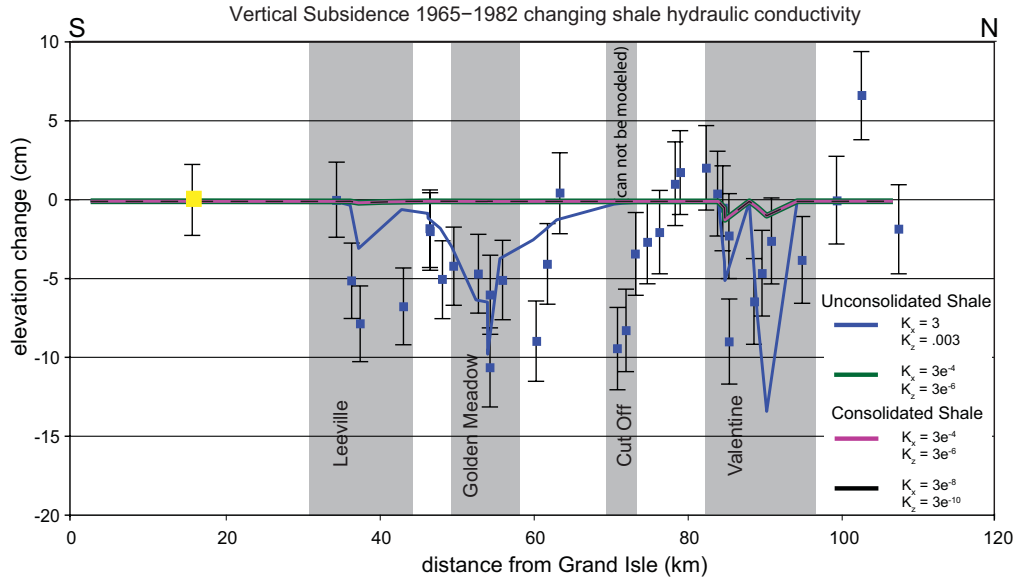
Figure 5.11: Effect of varying the hydraulic conductivity of the confining units for 1965-1982 leveling epoch.
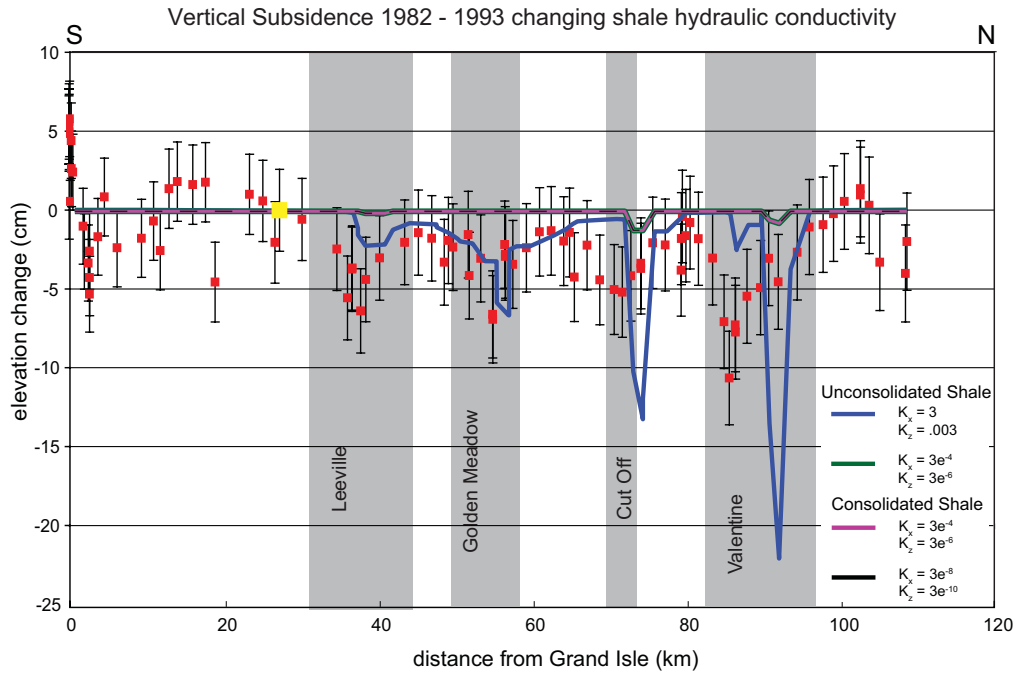
Figure 5.12: Effect of varying the hydraulic conductivity of the confining units for 1982-1993 leveling epoch.

Using the ranges of specific yield values reported by *Morris and Johnson* [1967] and *Gabrysch* [1982] for the Houston area we found that the MODFLOW model does not seem to be driven by variations in the specific yield. The results for the upper and lower limits of specific yield reported by *Morris and Johnson* [1967] and the values reported by *Gabrysch* [1982] are shown in Figures 5.13 and 5.14. Note that all of the modeled lines plot on top of each other.

Figure 5.13: Effect of specific yield on modeled subsidence for the 1965-1982 leveling epoch.
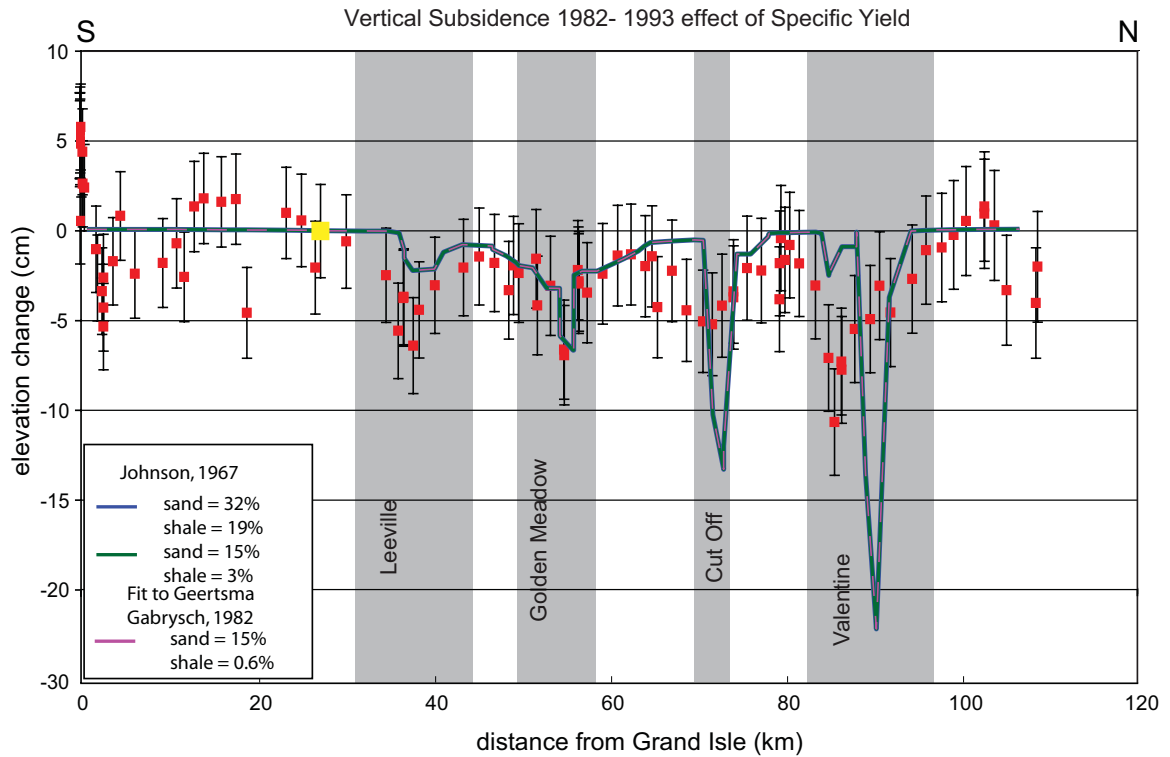
Figure 5.14: Effect of specific yield on modeled subsidence for the 1982-1993 leveling epoch.

Finally, we tested the effect of varying the specific storage on the modeled subsidence results in MODFLOW. As shown earlier, specific storage is effectively related to the compressibility of the sands and unconsolidated shales. We tested three specific storage parameters, the first two are the upper (blue line) and lower (green line) limits reported by *Domenico* [1972], and the last was determined using equation 5.8 and the compressibility used in the Geertsma modeling described in Chapter 4 (magenta line). The results are shown in Figures 5.15 and 5.16 for the two time epochs. We find that differing values of specific storage fit the leveling data over each field for both the 1965-1982 and 1982-1993 time epochs. This indicates that the compressibilities vary over the region.
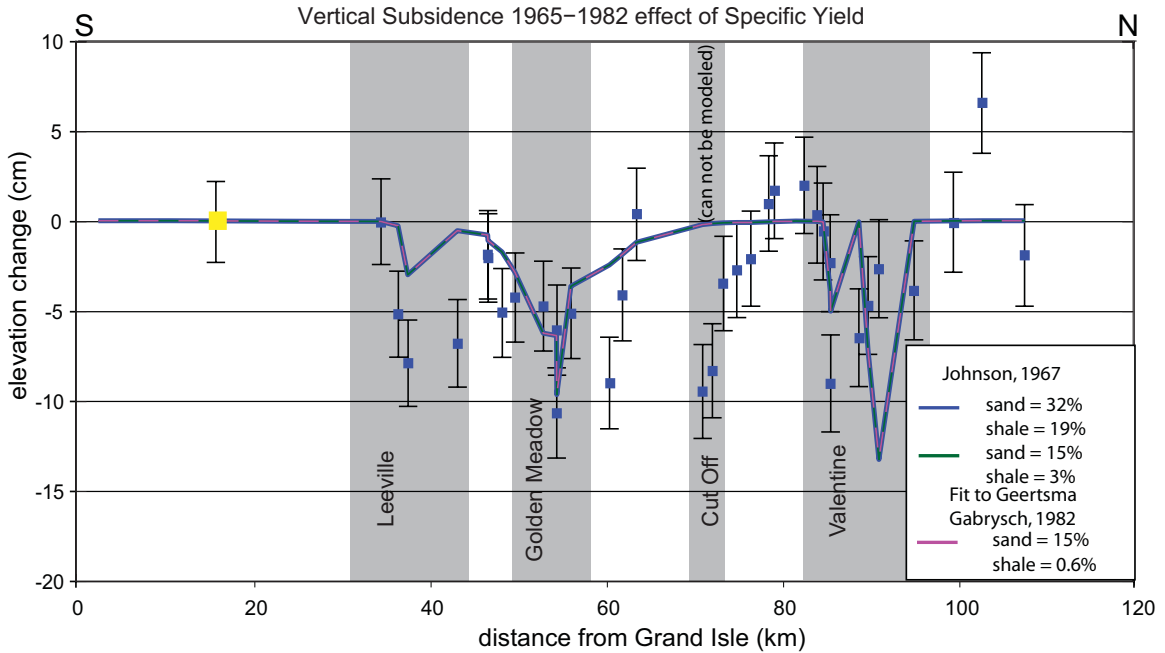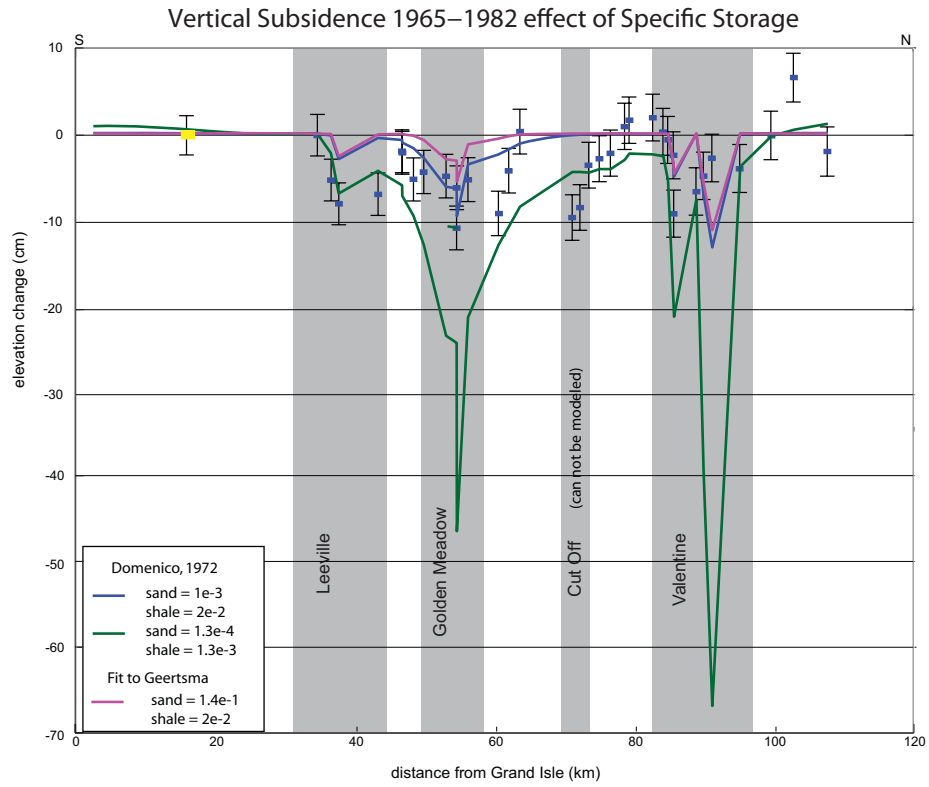
Figure 5.15: Effect of specific storage on modeled subsidence for the 1965-1982 leveling epoch.
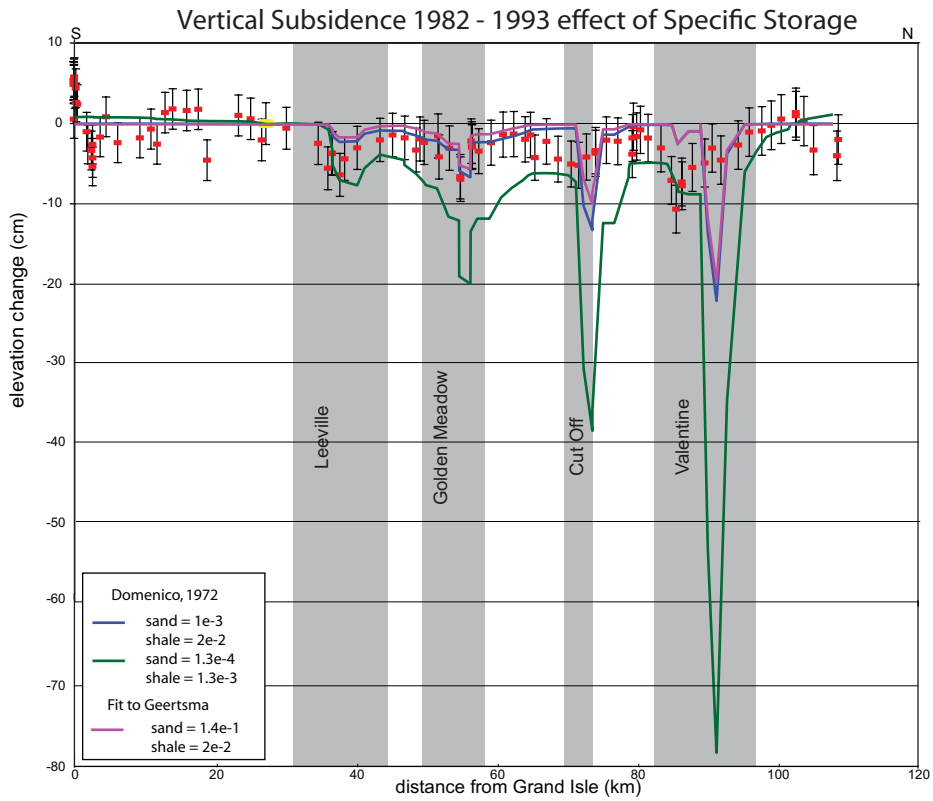
Figure 5.16: Effect of specific storage on modeled subsidence for the 1982-1993 leveling epoch.
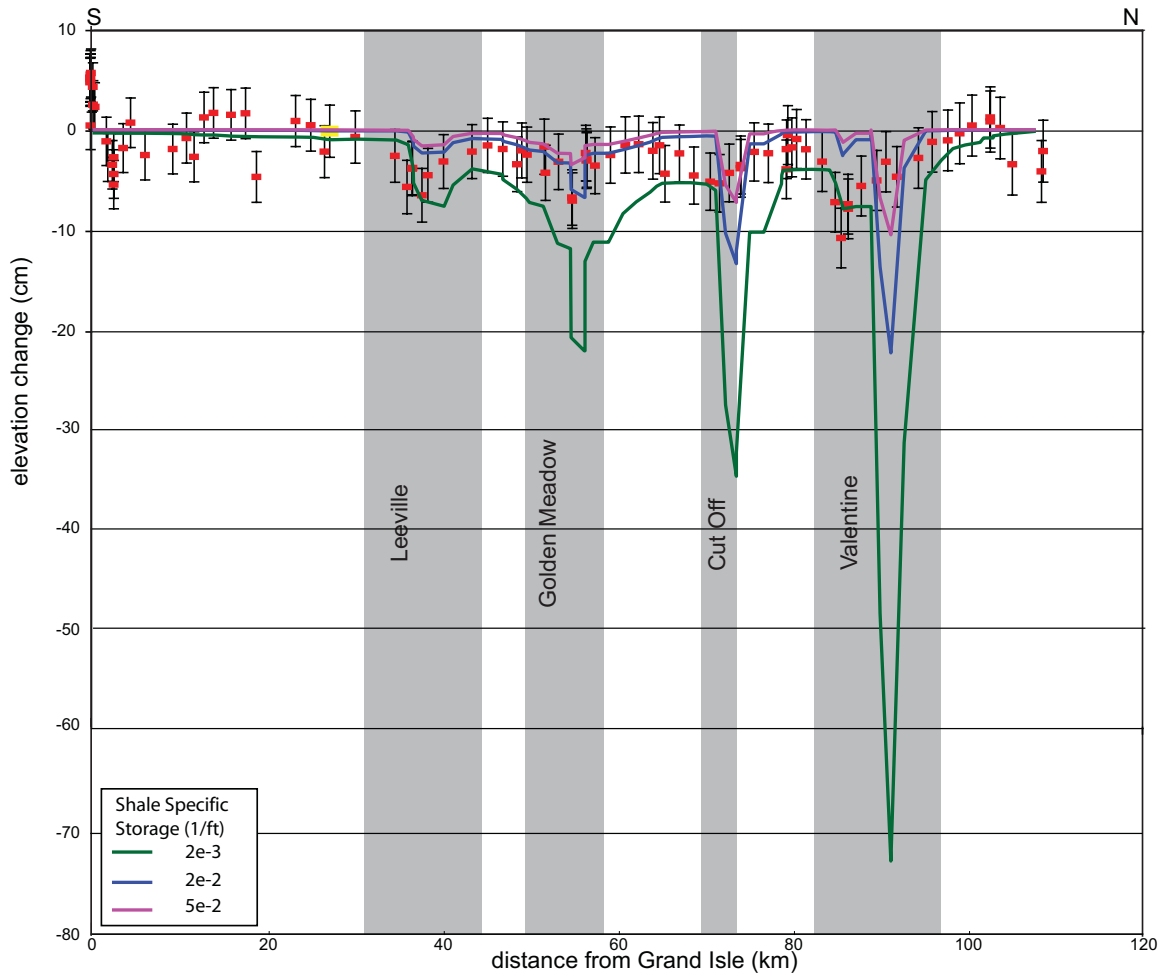
Figure 5.17: Varying shale specific storage values for best fitting model to fit the leveling data over each field. The best fit model uses the green line over Leeville, the blue line over Golden Meadow, and the magenta line over Cut Off and Valentine.

We proceed by using the values for sand specific storage determined from the best fitting Geertsma model and then test varying values for the shale specific storage. These results are shown in Figure 5.17. Again, different values of shale specific storage are needed to best fit the observed subsidence over each of the fields. Over the Leeville field a shale specific storage of $2e^{-3}$ (green line in Figure 5.17) fits well, but this over-predicts the observed subsidence over the remainder of the modeled fields. Over Golden Meadow a shale specific storage value of $2e^{-2}$ (blue line) fits well, and over the Cut Off and Valentine fields a shale specific storage value of $5e^{-2}$ fits well (magenta line).

After running the previously described parameter sensitivity tests we proceed with modeling the subsidence due to compaction of both the sands and shales over the two

time epochs of the leveling data, 1965-1982 and 1982-1993, and then two time periods following production to examine the role of shale compaction on continued subsidence once production has ended, 1993-2000, and 2000-2050. The "best-fit" MODFLOW parameters from the previous sensitivity analysis are used for these models. The "best-fit" parameters are: high hydraulic conductivities for unconsolidated sand and shale, a K_x/K_z ratio of 10/1 for sands and 100/1 for unconsolidated shales, the upper limit of the published specific yield, and the specific storage parameters determined from the Geertsma modeling for the sands and shale specific storage values of $2e^{-3}$ over Leeville, $2e^{-2}$ over Golden Meadow, and $5e^{-2}$ over Cut Off and Valentine. The results from this modeling are presented in the next section.

5.6 Modeled subsidence and subsidence predictions

Using the "best fit" MODFLOW model described in the previous section we model the production-induced subsidence due to compaction of both the sands and unconsolidated shales and compare it to both the observed subsidence and the predicted subsidence using the Geertsma model. If the "best-fit" MODFLOW model can capture the observed subsidence over both the 1965-1982 and 1982-1993 leveling epochs, including the increase in subsidence rate with decreasing production during the 1982-1993 epoch, we then extend the modeling to two additional time epochs. The additional modeled epochs, 1993-2000 and 2000-2050, are after the leveling and modeled production data ends and provide insight into the continued role of production induced subsidence in the Louisiana Coastal Zone.

We first model the subsidence caused by production induced compaction during the 1965-1982 time epoch. Figure 5.18 shows these results along the profile of the leveling line along with the results from the Geertsma model. The MODFLOW model (green line) fits both the leveling data and the Geertsma model (blue line) fairly well. MODFLOW matches the Geertsma model very well over Leeville and Valentine, underestimates at Golden Meadow, but is still within the error of the leveling line. During the 1965-1982 epoch the modeling results are affected by the removal of one reservoir in the Cut Off field that was modeled in the Geertsma solution. Due to the low

hydraulic conductivity of the unconsolidated shales relative to their horizontal hydraulic conductivity there is very little compaction of the shales being modeled in this time epoch, which explains why the MODFLOW and Geertsma models provide such similar results.

Figure 5.18: Profile of MODFLOW results along the 1965-1982 leveling line relative to the station in yellow. The leveling data is shown as blue squares with associate error bars. The MODFLOW model is the solid green line and can be compared to the analytical Geertsma model shown as a solid blue line.

Figure 5.19 shows the profile along the leveling line along with the Geertsma and MODFLOW modeling results for the 1982-1993 leveling epoch. The Geertsma model (blue line) only models the subsidence due to production-induced compaction of reservoir sands as stated earlier; this is likely the reason that it underestimates the observed subsidence. The MODFLOW results (green line), however, model production-induced subsidence due to compaction of both the reservoir sands and the reservoir bounding shales. While the Geertsma model under predicts the observed subsidence during this time epoch, the MODFLOW results fit the observed subsidence quite well. As noted in previously the 1982-1993 time epoch had an increase in the observed subsidence rate coupled with a decrease in oil and gas production that could not be explained by elastic-plastic compaction of reservoir sands or modeled using Geertsma

(see Figures 5.2, 5.3 and Chapter 4). However, by including time-dependent compaction of the reservoir bounding shales in the MODFLOW modeling we are able to capture this increase in subsidence rate while honoring the production data. This indicates that production-induced compaction of shales plays a significant role in the subsidence signal in Lafourche Parish along LA1, and likely in the entire Louisiana Coastal Zone. It also indicates that while oil and gas production may have decreased or stopped in the region subsidence due to earlier production may remain an important signal in the future.
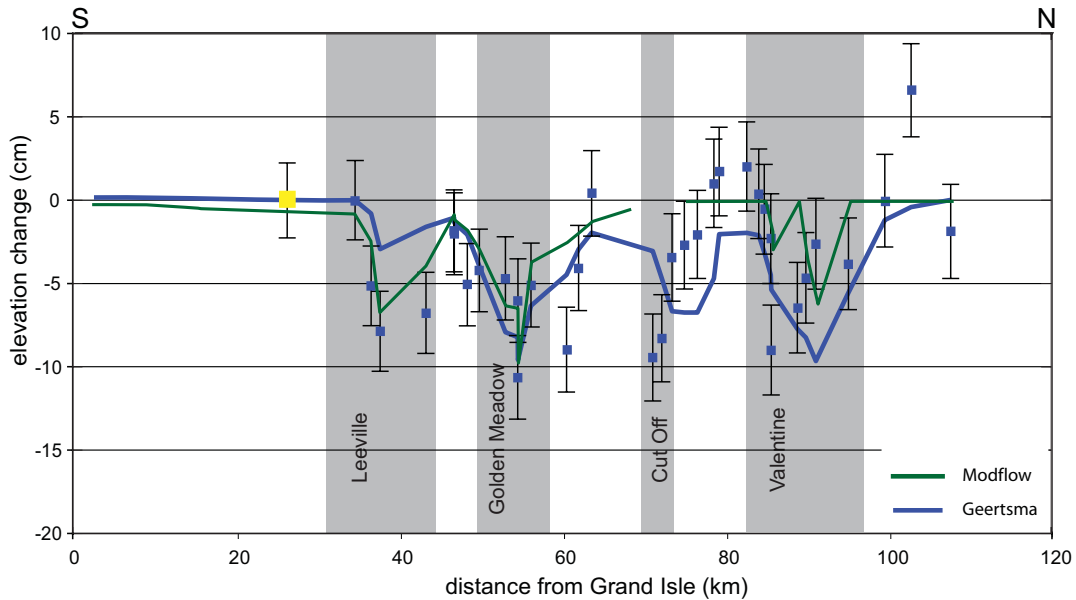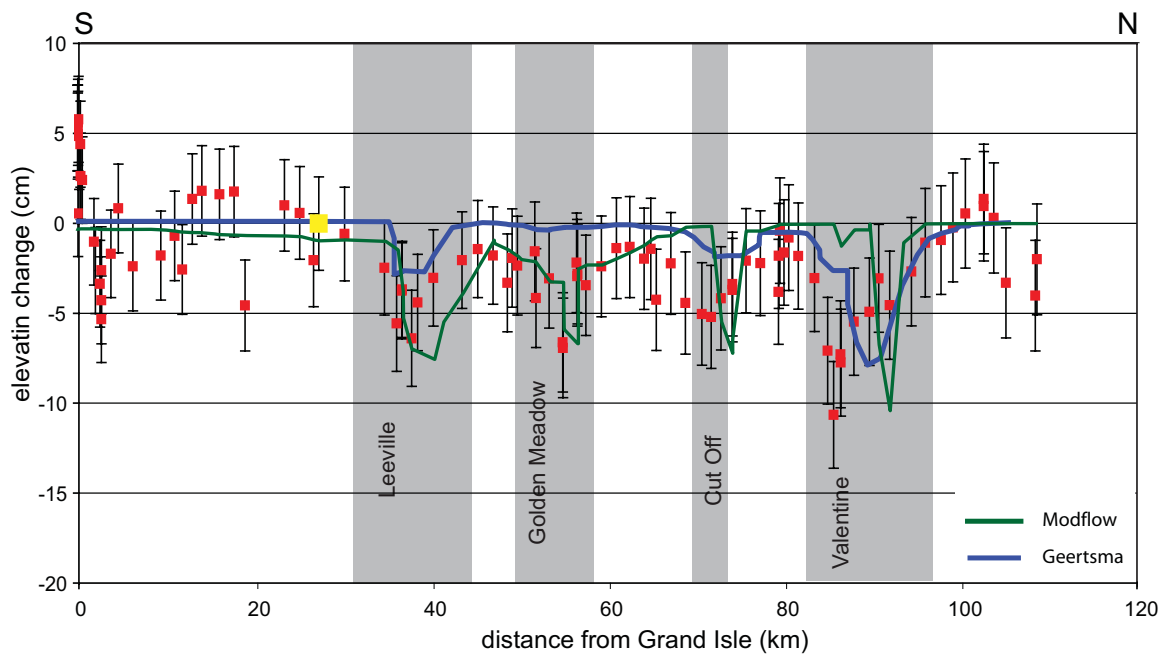

Figure 5.19: Profile of MODFLOW results along the 1982-1993 leveling line relative to the station in yellow. The leveling data is shown as red squares with associate error bars. The MODFLOW model is the solid green line and can be compared to the analytical Geertsma model shown as a solid blue line.

Since the results of the MODFLOW modeling fit the observed subsidence data during the 1965-1982 and 1982-1993 time epochs we feel confident in using the results of MODFLOW for two additional time epoch, 1993-2000 and 2000-2050, to predict subsidence due to continued compaction of the sands and unconsolidated shales following the end of modeled production. This provides insight into the possible role that production induced sand and shale compaction may play in the long term subsidence in the Louisiana Coastal Zone and as a way to guide future restoration and protection efforts. During the 7 years following the end of modeled production there continues to be

subsidence centered over the producing fields, with magnitudes equal to or exceeding those observed during active production. This is not surprising as more of the unconsolidated shales are compacting and dewatering in response to the drop in head (pressure) in the sands. To keep these predicted subsidence signals in context with what was seen and modeled earlier Figure 5.20 shows the modeled subsidence along the profile of the leveling line with the 1993 reference surface shown as the red line. Along this profile it becomes apparent that directly over the producing reservoirs subsidence is continuing, and even accelerating, due to continued compaction of both the sands and additional compaction in the unconsolidated shales.
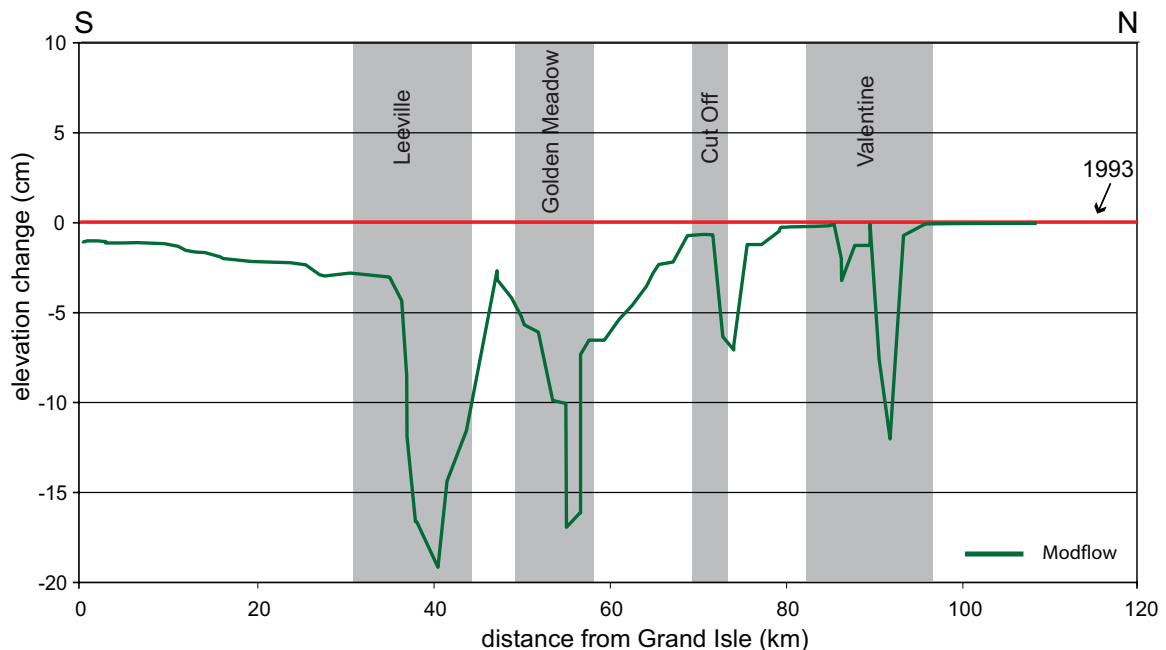
Figure 5.20: Profile of MODFLOW results for the 1993-2000 epoch along the leveling line relative to the station in yellow. The model results are shown as a green solid line and the 1993 reference surface shown as the red line.

If we extend the MODFLOW subsidence modeling to a fourth epoch from 2000-2050 we see similar results as in the 1993-2000 time epoch. The 2000-2050 time epoch was chosen as this is the time span used in many of the regional projections of land loss in the Louisiana Coastal Zone that are being used for regional planning and restoration efforts. The modeled subsidence along the leveling line profile is shown in Figure 5.21 with the red line indicating a year 2000 reference surface. These results indicate that

subsidence, especially localized over the oil and gas fields, will continue to remain important over the next 50 years, even after production has ended
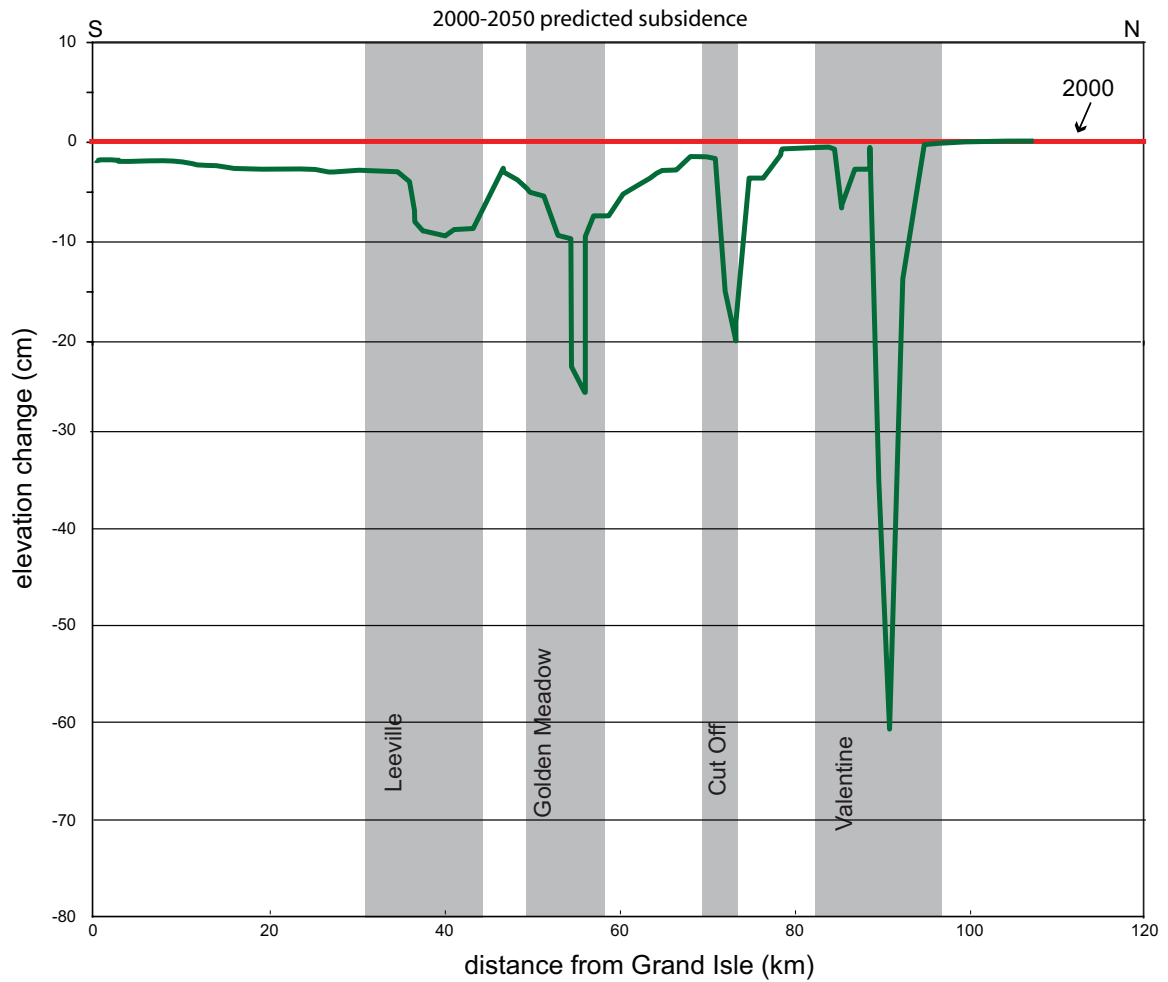
Figure 5.21: Profile of MODFLOW results for the 2000-2050 epoch along the leveling line relative to the station in yellow. The model results are shown as a green solid line and the 2000 reference level shown as the red line.

While Figures 5.20 and 5.21 show that production-induced subsidence will continue to be important even after oil and gas production has ended in the area, the differing lengths of the modeled epochs makes it difficult to compare how the subsidence rates change. Thus, we convert the modeled subsidence for the 1965-1982, 1982-1993, and 2000-2050 time epochs into subsidence rate in order to directly compare them. This is shown in Figure 5.22. As in all previous plots the subsidence rate for the 1965-1982

epoch is shown in blue, the 1982-1993 epoch in red, and now we have added the predicted subsidence rate for the 2000-2050 epoch in green. Figure 5.22 clearly shows the increase in subsidence rate from the 1965-1982 and 1982-1993 leveling epochs. The subsidence rate between 2000 and 2050 is predicted to decrease over the Leeville, Golden Meadow, and Cut Off fields and increase over the Valentine field. Despite the predicted decreases in subsidence rate over the Leeville, Golden Meadow, and Cut Off fields, the subsidence rate continues to be between 2 and 6 mm/yr, which may be significant in this low lying coastal area. A likely explanation for the continued increase in subsidence rate over the Valentine field can be found by referring back to the production data shown in Figure 5.3. While production rates fell during the 1982-1993 time epoch in the Leeville, Golden Meadow, and Cut Off field, production remained high in the Valentine field. This means that the increase in subsidence rate during the 1982-1993 epoch over the Valentine field was due to not only production-induced compaction of the shales, but also additional elastic-plastic reservoir sand compaction. Thus, during the 2000-2050 epoch the reservoir bounding shales in the Valentine field are responding to larger, and more recent reservoir pressure declines and compaction than the other modeled fields.
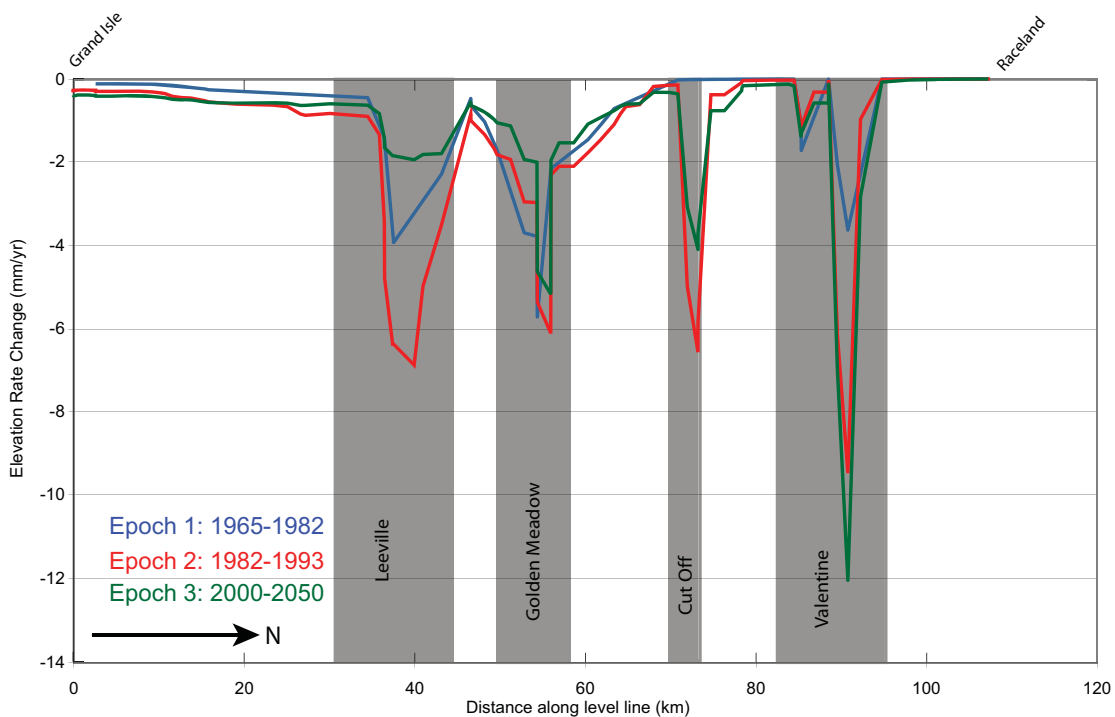
Figure 5.22: Modeled subsidence rates along the LA1 leveling line for the 1965-1982 (blue), 1982-1993 (red), and 2000-2050 (green) epochs.

Predicted future subsidence rates due to production-induced subsidence is a beneficial new piece of information for regional planners in the Louisiana Coastal Zone. However, rates alone are not sufficient to determine where subsidence may have the largest impact. For example, the 9 m of subsidence observed in the San Joaquin Valley of California had a dramatic effect on the landscape and impacted built structures, but the land remained usable due to its elevation [*Poland, et al.*, 1975]. However, in the Louisiana Coastal Zone most of the land is at or near sea level such that even small changes in elevation can lead to land and wetland loss due to relative sea level rise. Using the 1993 elevations observed along the LA 1 leveling line and the predicted production-induced subsidence rate for 2000-2050 we predict the elevation along the leveling line in the year 2050. These elevations are shown in Figure 5.23 with the red line indicating the 1993 observed elevation and the green line indicating the predicted 2050 elevation. What becomes apparent from this plot is that while there are significant amounts of subsidence over the four modeled oil and gas fields, the area in the most danger for land loss is over the Golden Meadow field. This is due to the extremely low elevation of the field in 1993 such that the predicted subsidence between 2000 and 2050 is actually sufficient to send portions of this area below sea level. While there is predicted to be more subsidence over the Valentine field during this same time period its relatively high elevation for the region keeps much of the area > 1 m above sea level.

Figure 5.23: Observed and predicted elevations along the Louisiana Highway 1 leveling line. The red line indicates the observed elevation in 1993 and the green line indicates the predicted elevation in 2050 due to continued production-induced sand and shale compaction.

5.7 Discussion

This work extends production-induced compaction subsidence modeling in the Louisiana Coastal Zone to include the time-dependent effe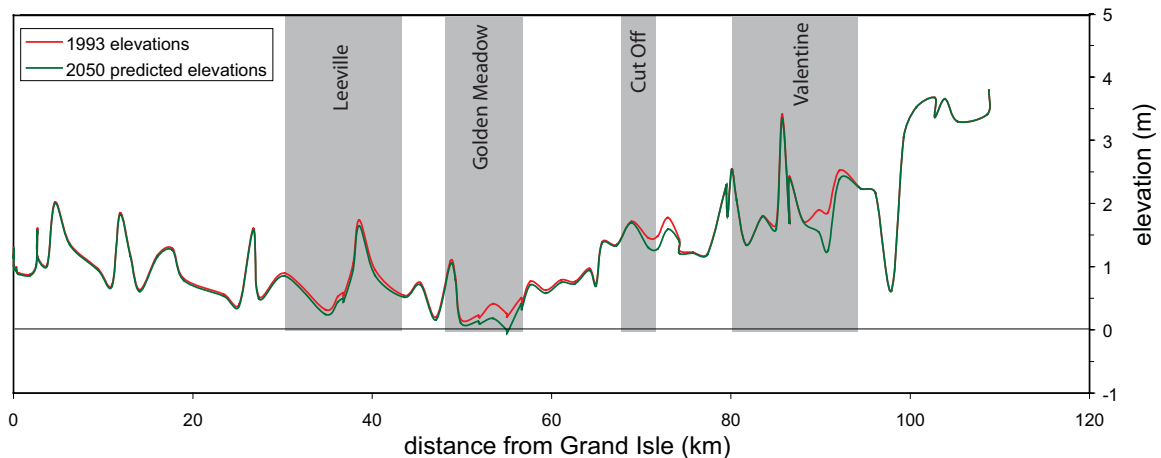ct of shales for the first time. Previous work described in Chapter 4 showed that production-induced reservoir compaction can explain the subsidence observed over oil and gas fields in Lafourche Parish. However, elastic-plastic sand compaction was not sufficient to explain the accelerating subsidence rate observed during the 1982-1993 epoch despite decreases in oil and gas production. This accelerating subsidence rate despite decreasing production suggests a time-dependent mode of subsidence such as shale compaction. We model production-induced subsidence due to sand and shale compaction using MODFLOW. We find the MODFLOW reproduces the observed subsidence during both the 1965-1982 and 1982-1993 time epochs, including the accelerating subsidence observed over the oil and gas fields during the 1982-1993 epoch which elastic-plastic sand compaction can not. We then extend the modeling to predict the subsidence after leveling and production data ended for the 1993-2000 and 2000-2050 epochs to estimate the continued role of production-induced subsidence in the Louisiana Coastal Zone.

Previous predictions of land loss relied on qualitative observations of land loss and subsidence with little to no quantitative modeling and simply extrapolated current rates to determine future land losses. While historical land loss rates indicate regions where subsidence and sea level rise may drive future land losses, the spatial and temporal variability of the driving mechanisms suggests that simple extrapolations of current land loss rates may not be sufficient for planning of future protection and restoration efforts. The Coast 2050 plan is meant to be the current template to provide guidance to parish, state, and federal agencies for the development of coastal restoration policies. However, the projected land loss rates between 2000 and 2050 were determined in this report by simply extrapolating the land loss observed from aerial photographs and satellite imagery between 1974 and 1990. As is evidenced by the leveling data, the rates of subsidence (a major component of land loss in this region) are not constant through time, and thus future rates can not be determined without understanding the driving mechanisms. The MODFLOW modeling presented in this chapter indicates that the local subsidence bowls

observed over oil and gas fields in Lafourche Parish can be explained by production-induced compaction of sand and shale. The inclusion of time-dependent shale compaction is able to explain variations in subsidence rate that do not correlate with production rates and predicts subsidence will continue for at least 50 years following the end of oil and gas production. These variations in subsidence rate, and the resulting land loss would not be captured by the extrapolation of previous land loss rates as is done in the Coast 2050 report. Future coastal restoration planning would benefit from considering the improved predictions of subsidence rate presented in this chapter.

Morton et al. [2006] argues that many numerical models underestimate observed subsidence due to our lack of understanding of the subsurface mechanisms. Thus, instead of using numerical models to determine future subsidence *Morton et al.* [2006] suggests that predictions should be based simply on the subsidence observations at benchmarks while ignoring the underlying mechanisms. In an area where small amounts of subsidence will have a large impact on land loss and considerable amounts of money are being spent for increased coastal protection and restoration projects making predictions about future subsidence rates with disregard for the underlying mechanism is a dangerous proposition. We have shown in this work that the MODFLOW modeling of production-induced sand and shale compaction is able to accurately reproduce the observed subsidence. This indicates that we are likely modeling the underlying subsidence mechanism correctly, and will have more reliable estimates of future subsidence than if we ignored the driving mechanism altogether and simply used the subsidence observations.

Morton et al. [2006] continues by arguing that the production-induced subsidence in the Louisiana Coastal Zone is comparable to the subsidence observed in the Houston-Galveston region due to groundwater pumping. Drawing on this analogy he argues that as oil and gas production decreases in southern Louisiana the subsidence rate will decrease. However, while production rates decreased in the 1982-1993 epoch the leveling data shows an increase in subsidence rate during this same time period (Figures 5.2 and 5.3). While subsidence in the Houston-Galveston region did decrease with decreases in fluid production[*Gabrysch and Coplin*, 1990] there is a fundamental

difference between the system in Texas and the Louisiana Coastal Zone. The producing aquifers in the Houston-Galveston region are shallow, laterally extensive units recharged by surface water whereas the producing oil and gas reservoirs in Louisiana are deep, compartmentalized units. These deep reservoirs only recover fluid pressure from fluids flowing into the reservoir from the surrounding units which leads to additional compaction and thus subsidence even after production has stopped. This is similar to what was seen in the San Joaquin Valley in California [*Poland, et al.*, 1975]. It is likely that the recharging of the aquifers in the Houston-Galveston region is sufficiently fast as to limit the amount of shale compaction due to pressure decreases in the aquifer sands (though extensometer data does show some permanent shale compaction [*Kasmarek, et al.*, 1997]). This is not the case in Louisiana where all of the fluid to recharge the depleted reservoirs comes from the surrounding shales and adds to the overall subsidence signal.

While the MODFLOW modeling presented in this chapter is able to accurately capture the subsidence during both the 1965-1982 and 1982-1993 time epochs by modeling production-induced compaction of the sands and shales, many simplifying assumptions that were made. First, as stated previously, MODFLOW only calculates displacements in the vertical direction. In reality surface displacements due to reservoir compaction at depth will have both a vertical and horizontal component, but in general the horizontal displacement is much smaller than the vertical. Additionally, in the Louisiana Coastal Zone the vertical component will be the most important due to the low-lying nature of the region and the largest threat coming from land loss due to relative sea level rise. Moving to a full 3D finite element modeling scheme would allow for the estimation of both horizontal and vertical surface displacements due to production-induced compaction of both the reservoir sands and reservoir bounding shales. However, the lack of data in the Louisiana Coastal Zone prohibits this more rigorous modeling technique as there would be too many free variables and the results would be highly non-unique.

The second major assumption addresses the fact that MODFLOW and the Geertsma equations (as used in Chapter 4) model the half-space differently. Geertsma is

a nucleus-of-strain and assumes that the half-space is elastic. MODFLOW, however, is a poroelastic model with all deformation occurring vertically. These differences mean that the displacements at depth will not be the same for the two modeling techniques, but they produce very similar results at the surface. Thus, while the predictions of surface subsidence are comparable, care should be taken when interpreting the displacements at depth. Finally, as there was no constitutive parameter information available for the sand and shale units in the modeled region we used acceptable ranges of parameter values in the MODFLOW modeling constrained by observed surface subsidence measurements. This coupled with the incompleteness of the pressure data for the region indicates that the values of the constitutive parameters used are likely not a true representation of the actual sand and shale parameters at depth. Instead, these values used in the model stack create an effective medium model which generates a similar surface expression as the true material properties. The only way to move beyond these simplifying assumptions in the modeling is with additional subsurface, production, and pressure data along with lab measurements on the producing reservoir sands and bounding shales. Despite not having this information the MODFLOW modeling is able to reproduce the surface data from both time periods and is able to capture the observed changes in subsidence rate with the available pressure data. This gives us confidence in our results, conclusions, and predictions of future subsidence rates.

In the wake of Hurricanes Katrina and Rita in 2005 coastal protection and restoration has been brought to national and international attention with significant amounts of money being committed to projects in the Gulf Coast region [*Day Jr., et al.*, 2007]. In January, 2006 the American Geophysical Union convened a group of experts to survey the current knowledge of the Gulf Coast environment most relevant to hurricane protection, to identify gaps in knowledge, and to present ways to integrate science into the reconstruction, protection, and restoration of the US Gulf Coast along with near-term and long-term needs to guide research [2006]. One of the major topics discussed was subsidence and the role of oil and gas production. The major near-term need identified was accurate vertical elevation control such that protection barriers could be constructed tall enough to withstand future storms while allowing for future subsidence. The report identified the following long term needs: 1) "a landscape model

that can accurately predict future integrated effects of subsidence and sediment accretion" and 2) "improved models of fault movement, petroleum extraction, and water pumping are required to predict future extent of subsidence processes" [2006]. The work presented in this chapter is the first step in meeting these near- and long-term needs for the successful rebuilding of the US Gulf Coast and provides a new tool for local and regional planners for use in their protection and restoration plans.

5.8 Conclusions

Previous work has indicated that production-induced subsidence in the Louisiana Coastal Zone is an important, but local, component of the regional subsidence signal. Multiple epochs of leveling data provide insight into time-dependent mechanisms influencing the subsidence signal. In our study area in Lafourche Parish the subsidence rate during the 1982-1993 leveling epoch is markedly greater than the subsidence rate during the 1965-1982 leveling epoch. This acceleration in the subsidence rate is despite a decrease in the rate of fluid production from the Leeville, Golden Meadow, Cut Off, and Valentine oil and gas fields. One possible mechanism to explain the accelerating subsidence despite decreasing production is the time-dependent compaction of the reservoir bounding shales. We use MODFLOW-2000, a groundwater flow modeling package developed by the U.S. Geological Survey, to model the effect of time-dependent compaction of the shales due to earlier production on the subsidence signal. Our results indicate that subsidence due to compaction of the reservoir bounding shales is an important component of the subsidence signal that should be included in any regional subsidence model for the Louisiana Coastal Zone. In addition, accurate modeling of the subsidence due to shale compaction may provide an indication of the amount of continued subsidence in the region, and should be considered in regional restoration and protection plans. This modeling indicates that subsidence over the producing oil and gas fields will continue well after production ends and thus any restoration efforts should take this into account and not plan restoration in these actively subsiding areas directly over oil and gas fields. In addition, we are able to use observed surface elevations in 1993 along with our predicted subsidence rate for 2000-2050 to estimate the elevation along

Louisiana Highway 1 in 2050. This indicates that portions of the area overlying the Golden Meadow field will be below sea level by 2050 and is likely not a good candidate for restoration efforts and new protection plans need to take this into account. This work provides new information and a new tool for local and regional planners working on reconstruction, protection, and restoration plans for the US Gulf Coast in the aftermath of Hurricanes Katrina and Rita.

References

(1998), Coast 2050: Toward a Sustainable Coastal Louisiana, 161 pp, Louisiana Department of Natural Resources, Baton Rouge, Louisiana.

(2006), Hurricanes and the U.S. Gulf Coast: Science and Sustainable Rebuilding, American Geophysical Union, http://www.agu.org/report/hurricanes/.

Angelier, J. (1989), From Orientation to Magnitudes in Paleostress Determinations Using Fault Slip Data, *Journal of Structural Geology*, *11*, 37-50.

Bakun, W. H. (1999), Seismicity Activity of San Francisco Bay Region, *Bull. Seismol. Soc. Am.*, *89*, 764-784.

Belardinelli, M. E., M. Cocco, O. Coutant, and F. Cotton (1999), Redistribution of Dynamic Stress During Coseismic Ruptures: Evidence for Fault Interaction and Earthquake Triggering, *J. Geophys. Res.*, *104*, 14925-14945 doi:11999JB900094.

Beroza, G. C., and M. D. Zoback (1993), Mechanism Diversity of the Loma Preita Aftershocks and the Mechanisms of Mainshock-Aftershock Interaction, *Science*, *259*, 210-213.

Boesch, D. F., M. N. Josselyn, A. J. Mehta, J. T. Morris, W. K. Nuttle, C. A. Simenstad, and D. J. P. Swift (1994), Scientific Assessment of Coastal Wetland Loss, Restoration and Management in Louisiana, *Journal of Coastal Research*, *Special issue 20*, 103.

Chan, A. W. (2004), Production Induced Reservoir Compaction, Permeability Loss and Land Surface Subsidence, Unpublished Ph.D. Thesis thesis, 170 pp, Stanford University, Stanford.

Chan, A. W., P. N. Hagin, and M. D. Zoback (2004), Viscoplastic Deformation, Stress and Strain Paths in Unconsolidated Reservoir Sands (Part 2): Field Applications Using Dynamic Dars Analysis, *SPE/ARMS*, *04-568*.

Chan, A. W., P. N. Hagin, and M. D. Zoback (in preparation), Time Dependent Elastic-Viscoplasticity (Evp) and the Dynamic Dars.

Chan, A. W., and M. D. Zoback (2002), Deformation Analysis in Reservoir Space (Dars): A Simploe Formalism for Prediction of Reservoir Deformation with Depletion, paper presented at SPE/ISRM Rock mechanics Conference, SPE/ISRM 78174, Irving, TX, Oct. 2002.

Chan, A. W., and M. D. Zoback (2007), The Role of Hydrocarbon Production on Land Subsidence and Fault Reactivation in the Louisiana Coastal Zone, *Journal of Coastal Research*, *23*, 771-786.

Coleman, J. M., and H. H. Roberts (1989), Deltaic Coastal Wetlands, *Geologie en Mijnbouw*, *68*, 1-24.

Cotton, F., and O. Coutant (1997), Dynamic Stress Variations Due to Shear Faults in a Plane-Layered Medium, *Geophys. J. Int.*, *128*, 676-688.

Das, S., and C. H. Scholz (1981), Off-Fault Aftershock Clusters Caused by Shear Stress Increase?, *Bull. Seismol. Soc. Am.*, *71*, 1669-1675.

Day Jr., J. W., D. F. Boesch, E. J. Clairain, G. P. Kemp, S. B. Laska, W. J. Mitsch, K. Orth, H. Mashriqui, D. J. Reed, L. Shabman, C. A. Simenstad, B. J. Streever, R. R. Twilley, C. C. Watson, J. T. Wells, and D. F. Whigham (2007), Restoration of the Mississippi Delta: Lessons from Hurricanes Katrina and Rita, *Science*, *315*, 1679-1684.

Dokka, R. K. (2006), Modern-Day Tectonic Subsidence in Coastal Louisiana, *Geology*, *28*, 281-284.

Domenico, P. A. (1972), *Concepts and Models in Groundwater Hydrology*, McGraw-Hill, New York.

Dutton, A. R., B. Harden, J.-P. Nicot, and D. O'Rourke (2003), Groundwater Availability Model for the Central Part of the Carrizo-Wilcox Aquifer in Texas, 295 pp, Bureau of Economic Geology.

Dziewonski, A. M., T.-A. Chou, and J. H. Woodhouse (1981), Determination of Earthquake Source Parameters from Waveform Data for Studies of Global and Regional Seismicity, *J. Geophys. Res.*, *86*, 2825-2852.

Felzer, K. R., R. E. Abercrombe, and G. Ekström (2004), A Common Origin for Aftershocks, Foreshocks, and Multiplets, *Bull. Seismol. Soc. Am.*, *93*, 88-98.

Felzer, K. R., T. W. Becker, R. E. Abercrombe, G. Ekström, and J. R. Rice (2002), Triggering of the 1999 M_w 7.1 Hector Mine Earthquake by Aftershocks of the 1992 M_w 7.3 Landers Earthquake, *J. Geophys. Res.*, *107*, 2109, doi:2110.1029/2001JB000911.

Felzer, K. R., and E. E. Brodsky (2005), Testing the Stress Shadow Hypothesis, *J. Geophys. Res.*, *110*, doi: 10.1029/2004JB003277.

Felzer, K. R., and E. E. Brodsky (2006), Decay of Aftershock Density with Distance Indicates Triggering by Dynamic Stresses, *Nature*, *441*, 735-738.

Fetter, C. W. (2001), *Applied Hydrogeology*, 598 pp., Prentice Hall, Upper Saddle River, NJ.

Freed, A., M (2005), Earthquake Triggering by Static, Dynamic, and Postseismic Stress Transfer, *Annu. Rev. Earth Planet Sci.*, *33*, 335-367, doi: 310.1146/snnurev.earth.1133.092203.122505.

Freed, A., M, and J. Lin (2001), Delayed Triggering of the 1999 Hector Mine Earthquake by Viscoelastic Stress Transfer, *Nature*, *411*, 180-183.

Freeze, R. A., and J. A. Cherry (1979), *Groundwater*, 604 pp., Prentice Hall, Englewood Cliffs, NJ.

Frohlich, C. (1992), Triangle Diagrams: Ternary Graphs to Display Similarity and Diversity of Earthquake Focal Mechanisms, *Physics of the Earth and Planetary Interiors*, *75*, 193-198.

Frohlich, C. (2001), Display and Quantitative Assessment of Distributions of Earthquake Focal Mechanisms, *Geophys. J. Int.*, *144*, 300-308.

Gabrysch, R. K. (1982), Ground-Water Withdrawals and Land-Surface Subsidence in the Houston-Galveston Region, Texas, 1906-1980, *U.S. Geologcial Survey Open-File Report 82-571*, 68.

Gabrysch, R. K., and L. S. Coplin (1990), Land-Surface Subsidence in Houston -Galveston Region, Texas, 19 pp, Austin, TX.

Gagliano, S. M., E. B. Kemp, III, K. M. Wicker, K. S. Wiltenmuth, and R. W. Sabate (2003), Neo-Tectonic Framework of Southeast Louisiana and Applications to Coastal Restoration, in *Transactions - Gulf Coast Association of Geological Societies, Vol.53*, edited by G. W. Stone, et al., pp. 262-276.

Geertsma, J. (1973), Land Subsidence above Compacting Oil and Gas Reservoirs, *JPT. Journal of Petroleum Technology*, *25*, 734-744.

Gomberg, J., P. Bodin, and P. A. Reasenberg (2003), Observing Earthquakes Triggered in the near Field by Dynamic Deformations, *Bull. Seismol. Soc. Am.*, *93*, 118-138.

Gomberg, J., P. A. Reasenberg, P. Bodin, and R. A. Harris (2001), Earthquake Triggering by Seismic Waves Following Landers and Hector Mine Earthquakes, *Nature*, *411*, 462-466.

Gross, S., and R. Burgmann (1998), Rate and State of Background Stress Estimated from the Aftershocks of the 1989 Loma Prieta, California, Earthquake, *J. Geophys. Res.*, *103*, 4915-4927.

Habermann, R. E. (1987), Man-Made Changes in Seismicity Rates, *Bull. Seismol. Soc. Am.*, *77*, 141-159.

Hansen, K. M., and V. S. Mount (1990), Smoothing and Extrapolation of Crustal Stress Orientation Measurements, *J. Geophys. Res.*, *95*, 1155-1165.

Hardebeck, J. L., and E. Hauksson (2001), Crustal Stress Field in Southern California and Its Implications for Fault Mechanics, *J. Geophys. Res.*, *106*, 21859-21882.

Hardebeck, J. L., J. J. Nazareth, and E. Hauksson (1998), The Static Stress Change Triggering Model: Constraints from Two Southern Californa Aftershock Sequences, *J. Geophys. Res.*, *103*, 24427-24437.

Harris, R. A. (1998), Introduction to Special Section: Stress Triggers, Stress Shadows, and Implications for Seismic Hazard, *J. Geophys. Res.*, *103*, 24347-24358.

Harris, R. A., and R. W. Simpson (1996), In the Shadow of 1857 - the Effect of the Great Ft. Tejon Earthquake on Subsequent Earthquakes in Southern California, *Geophys. Res. Lett.*, *23*, 229-232.

Harris, R. A., and R. W. Simpson (1998), Suppression of Large Earthquakes by Stress Shadows: A Comparison of Coulomb and Rate-and-State Failure, *J. Geophys. Res.*, *103*, 24439-24451.

Hill, D. P., P. A. Reasenberg, A. Michael, W. J. Arabaz, G. C. Beroza, D. Brumbaugh, J. N. Brune, R. Castro, S. Davis, D. dePolo, W. L. Ellsworth, J. Gomberg, S. Harmsen, L. House, S. M. Jackson, M.

J. S. Johnston, L. M. Jones, R. Keller, S. Malone, L. Munguia, S. Nava, J. C. Pechmann, A. Sanford, R. W. Simpson, R. B. Smith, M. Stark, M. Stickney, A. Vidal, S. Walter, V. Wong, and J. Zollweg (1993), Seismicity Remotely Triggered by the Magnitude 7.3 Landers, California, Earthquake, *Science*, *260*, 1617-1623.

Höffmann, J., S. A. Leake, D. L. Galloway, and A. M. Wilson (2003), Modflow-2000 Ground-Water Model -- Users Guide to the Subsidence and Atuifer-System Compaction (Sub) Package, *U.S. Geolgcial Survey Open-File Report 03-233*, 44p.

Kasmarek, M., L. S. Coplin, and H. X. Santos (1997), Water-Level Altitudes 1997, Water-Level Changes 1977-1997, and 1996-1997, and Compaction 1973-1996 in the Chicot and Evangeline Aquifers, Houston-Galveston Region, Texas, *U.S. Geological Survey Open-file Report 97-181*.

Kilb, D., J. Gomberg, and P. Bodin (2000), Triggering of Earthquake Aftershocks by Dynamic Stresses, *Nature*, *408*, 570-574.

Kilb, D., J. Gomberg, and P. Bodin (2002), Aftershock Triggering by Complete Coulomb Stress Changes, *J. Geophys. Res.*, *107*, 2060, doi: 2010.1029/2001JB000202.

King, G. C. P., R. S. Stein, and J. Lin (1994), Static Stress Changes and the Triggering of Earthquakes, *Bull. Seismol. Soc. Am.*, *84*, 935-953.

Kooi, H., and J. J. de Vries (1998), Land Subsidence and Hydrodynamic Compaction of Sedimentary Basins, *Hydrology and Earth System Sciences*, *2*, 159-171.

Lin, J., and R. S. Stein (2004), Stress Triggering in Thrust and Subduction Earthquakes and Stress Interaction between the Southern San Andreas and Nearby Thrust and Strike-Slip Faults, *J. Geophys. Res.*, *109*, B2303, doi: 2310.1029/2003JB002607.

Ma, J.-F., C.-H. Chan, and R. Stein (2005), Response of Seismicity to Coulomb Stress Triggers and Shadows of the 1999 Mw = 7.6 Chi-Chi, Taiwan, Earthquake, *J. Geophys. Res.*, *110*, doi: 10.1029/2004/JB003389.

Mallman, E. P., and T. Parsons (2007 (submitted)), A Global Search for Stress Shadows, *J. Geophys. Res.*.

Mallman, E. P., and M. D. Zoback (2007a), Assessing Elastic Coulomb Stress Transfer Models Using Seismicity Rates in Southern California and Southwestern Japan, *J. Geophys. Res.*, *112*, doi: 10.1029/2005JB004076.

Mallman, E. P., and M. D. Zoback (2007b), Subsidence in the Louisiana Coastal Zone Due to Hydrocarbon Production, *Journal of Coastal Research*, *SI 50 (Proceedings of the 9th International Coastal Symposium)*, 443-449.

Marsan, D. (2003), Triggering of Seismicity at Short Timescales Following Californian Earthquakes, *J. Geophys. Res.*, *108*, 2266, doi: 2210.1029/2002JB001946.

Marsan, D. (2006), Can Coseismic Stress Variability Suppress Seismicity Shadows? Insights from a Rate-and-State Friction Model, *J. Geophys. Res.*, *111*, doi: 10.1029/2005JB004060.

Marsan, D., and S. S. Nalbant (2005), Methods for Measuring Seismicity Rate Changes: A Review and a Study of How the Mw 7.3 Landers Earthquake Affected the Aftershock Sequence of the Mw 6.1 Joshua Tree Earthquake, *Pure and Applied Geophysics*, *162*, 1151-1185, doi:1110.1007/s00024-00004-02665-00024.

Masterlark, T., and H. F. Wang (2002), Transient Stress-Coupling between the 1992 Landers and 1999 Hector Mine, Califorina, Earthquakes, *Bull. Seismol. Soc. Am.*, *92*, 1470-1486.

Matthews, M. V., and P. A. Reasenberg (1988), Statistical Methods for Investigating Quiescence and Other Temporal Seismicity Patterns, *Pageoph*, *126*, 357-372.

McCloskey, J., S. S. Nalbant, S. Steacy, C. Nostro, O. Scotti, and D. Baumont (2003), Structural Constraints on the Spatial Distribution of Aftershocks, *Geophys. Res. Lett.*, *30*, 1610, doi: 1610.1029/2003GL017225.

Meckel, T. A., U. S. ten Brink, and S. J. Williams (2006), Current Subsidence Rates Due to Compaction of Holocene Sediments in Southern Louisiana, *Geophys. Res. Lett*, *33*.

Meltzner, A. J., and D. J. Wald (2003), Aftershocks and Triggered Events of the Great 1906 California Earthquake, *Bull. Seismol. Soc. Am.*, *93*, 2160-2186.

Morris, D. A., and A. I. Johnson (1967), Sunnary of Hydrologic and Physical Properties of Rock and Soil Materials as Analyzed by the Hydrologic Laboratory of the Us Geological Survey 1948-1960, *USGS, Water Supply Paper 1839-D*.

Morton, R. A., J. C. Bernier, and J. A. Barras (2006), Evidence of Regional Subsidence and Associated Interior Wetland Loss Induced by Hydrocarbon Production, Gulf Coast Region, USA, *Environmental Geology*, *50*, 261-274.

Morton, R. A., J. C. Bernier, J. A. Barras, and N. F. Ferina (2005a), Historical Subsidence and Wetland Loss in the Mississippi Delta Plain, *Gulf Coast Association of Geological Societies Transactions*, *55*, 5555-5571.

Morton, R. A., J. C. Bernier, J. A. Barras, and N. F. Ferina (2005b), Rapid Subsidence and Historical Wetland Loss in the Mississippi Delta Plain: Likely Causes and Future Implications, *USGS Open File*, *2005-1216*, 116.

Morton, R. A., N. A. Buster, and M. D. Krohn (2002), Subsurface Controls on Historical Subsidence Rates and Associated Wetland Loss in Southcentral Louisiana, in *Transactions - Gulf Coast Association of Geological Societies, Vol.52*, edited by S. P. Dutton, et al., pp. 767-778.

Morton, R. A., N. A. Purcell, and R. L. Peterson (2001), Field Evidence of Subsidence and Faulting Induced by Hydrocarbon Production in Coastal Southeast Texas, in *Transactions - Gulf Coast Association of Geological Societies, Vol.51*, edited by M. T. Roberts, et al., pp. 239-248.

Morton, R. A., G. Tiling, and N. F. Ferina (2003a), Causes of Hot-Spot Wetland Loss in the Mississippi Delta Plain, *Environmental Geosciences*, *10*, 71-80.

Morton, R. A., G. Tiling, and N. F. Ferina (2003b), Primary Causes of Wetland Loss at Madison Bay, Terrebonne Parish, Louisiana, *USGS Open File*, *03-60*, 43.

Neighbors, R. J. (1981), Subsidence in Harris and Galveston Counties, Texas, *Journal of the Irrigation and Drainage Division*, *107*, 161-174.

Ogata, Y., L. M. Jones, and S. Toda (2003), When and Where the Aftershock Activity Was Depressed: Contrasting Decay Patterns of the Proximate Large Earthquakes in Southern California, *J. Geophys. Res.*, *108*, 2318-2329, doi: 2310.1029/2002JB002009.

Okada, Y. (1992), Internal Deformation Due to Shear and Tensile Faults in a Half-Space, *Bull. Seismol. Soc. Am.*, *82*, 1018-1040.

Paine, J. G. (1993), Subsidence of the Texas Coast; Inferences from Historical and Late Pleistocene Sea Levels, in *Tectonophysics*, edited by D. M. Anderson and G. P. Eaton, pp. 445-458.

Parsons, T. (2002), Global Omori Law Decay of Triggered Earthquakes: Large Aftershocks Outside the Classical Aftershock Zone, *J. Geophys. Res. 107*, 2199, doi: 2110.1029/2001JB000646.

Parsons, T. (2005), Significance of Stress Transfer in Tiem-Dependent Earthquake Probability Calculations, *J. Geophys. Res.*, *110*, doi: 10.1029/2004JB003190.

Parsons, T., A. A. Barka, S. Toda, R. S. Stein, and J. H. Dieterich (2000), Influence of the 17 August 1999 Izmit Earthquake on Seismic Hazards in Istanbul, in *The 1999 Izmit and Duzce Earthquakes: Preliminary Results*, edited by A. A. Barka, et al., pp. 295-310.

Parsons, T., R. S. Stein, R. W. Simpson, and P. A. Reasenberg (1999), Stress Sensitivity of Fault Seismicity: A Comparison between Limited-Offset Oblique and Major Strike-Slip Faults, *J. Geophys. Res.*, *104*, 20183-20202.

Peltzer, G., P. Rosen, F. Rogez, and K. Hudnut (1998), Poroelastic Rebound Along the Landers 1002 Earthquake Rupture Surface, *J. Geophys. Res.*, *103*, 30131-30145.

Penland, S., and K. E. Ramsey (1990), Relative Sea-Level Rise in Louisiana and the Gulf of Mexico; 1908-1988, *Journal of Coastal Research*, *6*, 323-342.

Penland, S., K. E. Ramsey, R. A. McBride, J. T. Mestayer, and K. A. Westphal (1988), Relative Sea Level Rise and Subsidence in Louisiana and the Gulf of Mexico, Coastal Geology Technical Report, 121 pp, Louisiana Geological Survey, Baton Rouge, Louisiana.

Penland, S., L. Wayne, L. D. Britsch, S. J. Williams, A. D. Beall, and V. C. Butterworth (2000), Process Classification of Coastal Land Loss between 1932 and 1990 in the Mississippi River Delta Plain, Southeastern Louisiana, *USGS Open File 00-418*.

Poland, J. F., B. E. Lofgren, R. L. Ireland, and R. G. Pugh (1975), Land Subsidence in the San Joaquin Valley, California, as of 1972, *U.S. Geolgcial Survey Professional Paper 437-H*, 78.

Pollitz, F., and M. J. S. Johnston (2006), Direct Test of Static Stress Versus Dynamic Stress Triggering of Aftershocks, *Geophys. Res. Lett.*, *33*, doi:10.1029/2006GL026764.

Pollitz, F., and I. S. Sacks (2002), Stress Triggering of the 1999 Hector Mine Earthquake by Transient Deformation Following the 1992 Landers Earthquake, *Bull. Seismol. Soc. Am.*, *92*, 1487-1496.

Probabilities, W. G. o. C. E. (2003), Earthquake Probabilities in the San Francisco Bay Region: 2002-2031, *U.S. Geologcial Survey Open-File Report 03-214*.

Reasenberg, P. A., and M. V. Matthews (1988), Precursory Seismic Quiescence: A Preliminary Assessment of the Hypothesis, *Pageoph*, *126*, 373-406.

Reasenberg, P. A., and R. W. Simpson (1992), Response of Regional Seismicity to the Static Stress Change Produced by the Loma Prieta Earthquake, *Science*, *255*, 1687-1690.

Reasenberg, P. A., and R. W. Simpson (1997), Response of Regional Seismicity to the Static Stress Change Produced by the Loma Prieta Earthquake, in *The Loma Prieta, California, Earthquake of October 17, 1989 - Aftershocks and Postseismic Effects*, edited by P. A. Reasenberg, pp. 49-71.

Richardson, E., and C. Marone (1999), Effects of Normal Stress Vibrations on Frictional Healing, *J. Geophys. Res.*, *104*, 28857-28878.

Roberts, H. H., A. Bailey, and G. J. Kuecher (1994), Subsidence in the Mississippi River Delta; Important Influences of Valley Filling by Cyclic Deposition, Primary Consolidation Phenomena, and Early Diagenesis, in *Transactions - Gulf Coast Association of Geological Societies, Vol.44*, edited by R. P. Major, pp. 619-629.

Scardina, A. D., J. A. Nunn, R. H. Pilger, Jr., and Anonymous (1981), Subsidence and Flexure of the Lithosphere in the North Louisiana Salt Basin, in *Eos, Transactions, American Geophysical Union*, edited, p. 391.

Sharp, J. M., Jr., and D. W. Hill (1995), Land Subsidence Along the Northeastern Texas Gulf Coast; Effects of Deep Hydrocarbon Production, *Environmental Geology*, *25*, 181-191.

Shinkle, K. D., and R. K. Dokka (2004), Rates of Vertical Displacement at Benchmarks in the Lower Mississippi Valley and the Northern Gulf Coast, *NOAA technical report*, *50*, 135.

Simpson, R. W., and P. A. Reasenberg (1994), Earthquake-Induced Static-Stress Changes on Central California Faults, in *The Loma Prieta, California, Earthquake of October 17, 1989 - Tectonic Processes and Models*, edited by R. W. Simpson, pp. 55-89.

Steacy, S., D. Marsan, S. S. Nalbant, and J. McCloskey (2004), Sensitivity of Static Stress Calculations to the Earthquake Slip Distribution, *J. Geophys. Res.*, *109*, B04303, doi:04310.01029/02002JB002365.

Steacy, S., S. S. Nalbant, J. McCloskey, C. Nostro, O. Scotti, and D. Baumont (2005), Onto What Planes Should Coulomb Stress Pertubations Be Resolved?, *J. Geophys. Res.*, *110*, doi: 10.1029/2004JB003356.

Stein, R., and M. Lisowski (1983), The 1979 Homestead Valley Earthquake Sequence, California; Control of Aftershocks and Postseismic Deformation *J. Geophys. Res.*, *88*, 6477-6490.

Stein, R. S. (1999), The Role of Stress Transfer in Earthquake Occurrence, *Nature*, *402*, 605-609.

Stein, R. S., A. A. Barka, and J. H. Dieterich (1997), Progressice Failure on the North Anatolian Fault since 1939 by Stress Triggering, *Geophys. J. Int.*, *128*, 594-604.

Suhayda, J. N. (1987), Subsidence and Sea Level, in *Causes of Wetland Loss in the Coastal Central Gulf of Mexico, Volume Ii:Technical Narrative*, edited by R. E. Turner and D. R. Cahoon, pp. 187-202, Minerals Management Survice, New Orleans, Louisiana.

Suhayda, J. N., A. M. Bailey, H. H. Roberts, S. Penland, and G. J. Kuecher (1993), Subsidence Properties of Holocene Sediments: South Louisiana, paper presented at Coastal Zone '93, American Society of Civil Engineering, New York, New York.

Swanson, R. L., and C. I. Thurlow (1973), Recent Subsidence Rates Along the Texas and Louisiana Coasts as Determined from Tide Measurements, *J. Geophys. Res., 78*, 2665-2671.

Toda, S., and R. Stein (2003), Toggling of Seismicity by the 1997 Kagoshima Earthquake Couplet: A Demonstration of Time-Dependent Stress Transfer, *J. Geophys. Res.*, *108*, 2567, doi: 2510.1029/2003JB002527.

Toda, S., R. Stein, K. B. Richards-Dinger, and S. B. Bozkurt (2005), Forecasting the Evolution of Seismicity in Southern California: Animations Built on Earthquake Stress Transfer, *J. Geophys. Res.*, *110*, S16, doi: 10.1029/2004JB003415.

Toda, S., R. S. Stein, P. A. Reasenberg, J. H. Dieterich, and A. Yoshida (1998), Stress Transferred by the 1995 Mw = 6.9 Kobe, Japan, Shock: Effect on Aftershocks and Future Earthquake Probabilities, *J. Geophys. Res.*, *103*, 24543-24565.

Townend, J., and M. D. Zoback (2001a), Focal Mechanism Stress Inversions in Southern California and the Strength of the San Andreas Fault, paper presented at Tectonic problems of the San Andreas fault system, Stanford University Publication, Stanford, CA.

Townend, J., and M. D. Zoback (2001b), Implications of Earthquake Focal Mechanisms for the Frictional Strength of the San Andreas Fault System, in *The Nature and Tectonic Significance of Fault Zone Weakening*, edited by R. E. Holdsworth, et al., pp. 13-21, Geological Society of London, London.

Townend, J., and M. D. Zoback (2006), Stress, Strain, and Mountain Building in Central Japan, *J. Geophys. Res.*, *111*, B30411, doi:30410.31029/32005JB003759.

Tsukahara, H., and Y. Kobayashi (1991), Crustal Stress in the Central and Western Parts of Honshu, Japan, *Zisin*, *44*, 221-231.

Wald, D. J. (1996), Slip History of the 1995 Kobe, Japan, Earthquake Determined from Strong Motion, Teleseismic, and Geodetic Data, *J. Phys. Earth*, *44*, 489-503.

Wald, D. J., and T. H. Heaton (1994), Spatial and Temporal Distribution of Slip for the 1992 Landers, California, Earthquake, *Bull. Seismol. Soc. Am.*, *84*, 668-691.

Weldon, R. J., and J. E. Springer (1988), Active Faulting near the Cajon Pass Well, Southern California: Implications for the Stress Orientation near the San Andreas Fault, *Geophys. Res. Lett.*, *15*, 993-996.

White, W. A., and R. A. Morton (1997), Wetland Losses Related to Fault Movement and Hydrocarbon Production, Southeastern Texas Coast, *Journal of Coastal Research*, *13*, 1305-1320.

Wiemer, S. (2001), A Software Package to Analyze Seismicity: Zmap, *Bull. Seismol. Soc. Am.*, *90*, 859-869.

Wiemer, S., and M. Wyss (2000), Minimum Magnitude of Completeness in Earthquake Catalogs: Examples from Alaska, the Western United States, and Japan, *Bull. Seismol. Soc. Am.*, *90*, 859-869.

Winston, R. B. (2000), Graphical User Interface for Modflow, Version 4, *U.S. Geologcial Survey Open-File Report 00-315*.

Woessner, J., E. Hauksson, S. Wiemer, and S. Neukomm (2004), The 1997 Kagoshima (Japan) Earthquake Doublet: A Quantitative Analysis of Aftershock Rate Changes, *Geophys. Res. Lett.*, *31*, doi: 10.1029/2003GL018858.

Wyss, M., and S. Wiemer (2000), Change in the Probability for Earthquakes in Southern California Due to the Landers Magnitude 7.3 Earthquake, *Science*, *290*, 1334-1338.

Yamashina, K. (1978), Induced Earthquakes in the Izu Peninsula by the Izu-Hanto-Oki Earthquake of 1974, Japan, *Tectonophysics*, *51*, 139-154.

Zoback, M. D., and J. H. Healy (1992), In Situ Stress Measurements to 3.5 Km Depth in the Cajon Pass Scientific Research Borehole: Implications for the Mechanics of Crustal Faulting, *J. Geophys. Res*, *97*, 55039-55058.